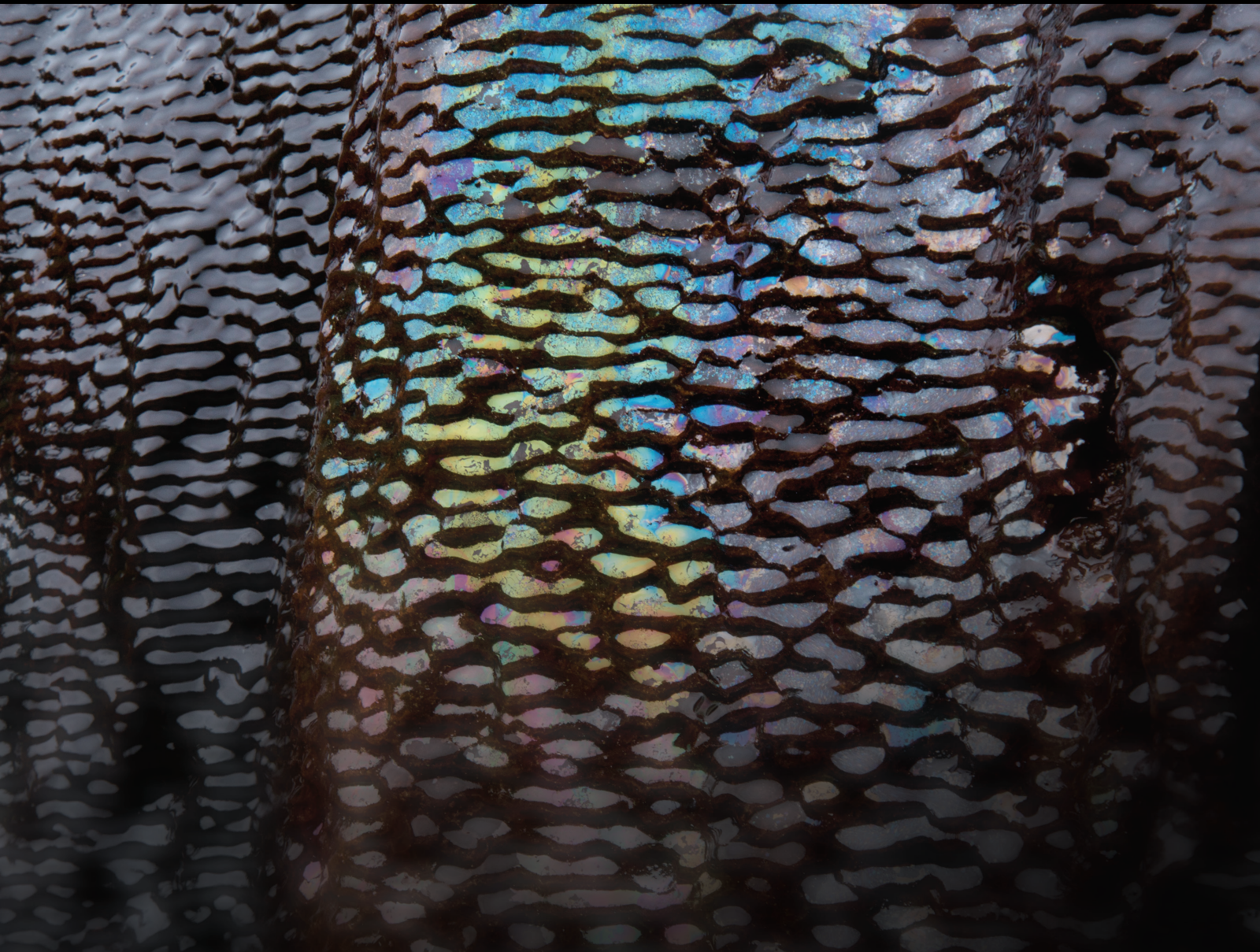


Emerging Techniques for Monitoring Geofluids and Geothermal Activities

Lead Guest Editor: Glenda Taddia

Guest Editors: Paolo Dabove, Alessandro Santilano, Margaret Shanafield,
and Christian Anibas





Emerging Techniques for Monitoring Geofluids and Geothermal Activities

Geofluids

Emerging Techniques for Monitoring Geofluids and Geothermal Activities

Lead Guest Editor: Glenda Taddia

Guest Editors: Paolo Dabove, Alessandro Santilano,
Margaret Shanafield, and Christian Anibas







Copyright © 2020 Hindawi Limited. All rights reserved.

This is a special issue published in "Geofluids." All articles are open access articles distributed under the Creative Commons Attribution License, which permits unrestricted use, distribution, and reproduction in any medium, provided the original work is properly cited.





























Chief Editor

































Umberta Tinivella, Italy

Associate Editors

Paolo Fulignati , Italy
Huazhou Li , Canada
Stefano Lo Russo , Italy
Julie K. Pearce , Australia

Academic Editors



Basim Abu-Jdayil , United Arab Emirates
Hasan Alsaedi , USA
Carmine Apollaro , Italy
Baojun Bai, USA
Marino Domenico Barberio , Italy
Andrea Brogi , Italy
Shengnan Nancy Chen , Canada
Tao Chen , Germany
Jianwei Cheng , China
Paola Cianfarra , Italy
Daniele Cinti , Italy
Timothy S. Collett , USA
Nicoló Colombani , Italy
Mercè Corbella , Spain
David Cruset, Spain
Jun Dong , China
Henrik Drake , Sweden
Farhad Ehya , Iran
Lionel Esteban , Australia
Zhiqiang Fan , China
Francesco Frondini, Italy
Ilaria Fuoco, Italy
Paola Gattinoni , Italy
Amin Gholami , Iran
Michela Giustiniani, Italy
Naser Golsanami, China
Fausto Grassa , Italy
Jianyong Han , China
Chris Harris , South Africa
Liang He , China
Sampath Hewage , Sri Lanka
Jian Hou, China
Guozhong Hu , China
Lanxiao Hu , China
Francesco Italiano , Italy
Azizollah Khormali , Iran
Hailing Kong, China

Karsten Kroeger, New Zealand
Cornelius Langenbruch, USA
Peter Leary , USA
Guangquan Li , China
Qingchao Li , China
Qibin Lin , China
Marcello Liotta , Italy
Shuyang Liu , China
Yong Liu, China
Yueliang Liu , China
Constantinos Loupasakis , Greece
Shouqing Lu, China
Tian-Shou Ma, China
Judit Mádl-Szonyi, Hungary
Paolo Madonia , Italy
Fabien Magri , Germany
Micòl Mastroicco , Italy
Agnes Mazot , New Zealand
Yuan Mei , Australia
Evgeniy M. Myshakin , USA
Muhammad Tayyab Naseer, Pakistan
Michele Paternoster , Italy
Mandadige S. A. Perera, Australia
Marco Petitta , Italy
Chao-Zhong Qin, China
Qingdong Qu, Australia
Reza Rezaee , Australia
Eliahu Rosenthal , Israel
Gernot Rother, USA
Edgar Santoyo , Mexico
Mohammad Sarmadivaleh, Australia
Venkatramanan Senapathi , India
Amin Shokrollahi, Australia
Rosa Sinisi , Italy
Zhao-Jie Song , China
Ondra Sracek , Czech Republic
Andri Stefansson , Iceland
Bailu Teng , China
Tivadar M. Tóth , Hungary
Orlando Vaselli , Italy
Benfeng Wang , China
Hetang Wang , China
Wensong Wang , China
Zhiyuan Wang , China
Ruud Weijermars , Saudi Arabia

Bisheng Wu , China
Da-yang Xuan , China
Yi Xue , China
HE YONGLIANG, China
Fan Yang , China
Zhenyuan Yin , China
Sohrab Zendeboudi, Canada
Zhixiong Zeng , Hong Kong
Yuanyuan Zha , China
Keni Zhang, China
Mingjie Zhang , China
Rongqing Zhang, China
Xianwei Zhang , China
Ye Zhang , USA
Zetian Zhang , China
Ling-Li Zhou , Ireland
Yingfang Zhou , United Kingdom
Daoyi Zhu , China
Quanle Zou, China
Martina Zucchi, Italy



Contents

The Temperature Evaluation of the Buried Hill Geothermal Reservoirs in the Jizhong Depression, Bohai Bay Basin, China

Yuyang Dong , Jianhui Zeng , Xianzheng Zhao, Yanu Wang, Tianhao Chen, Yongchao Zhang, and Sen Feng



Research Article (14 pages), Article ID 4814515, Volume 2020 (2020)

Relationship between Movement Laws of the Overlaying Strata and Time Space of the Mined-Out Volume

Xiang Yu, Kang Zhao , Qing Wang , Yajing Yan, Yongjun Zhang, and Junqiang Wang


Research Article (9 pages), Article ID 2854187, Volume 2020 (2020)

Hydraulic Fracturing Behavior in Shale with Water and Supercritical CO₂ under Triaxial Compression

Jianming He , Yixiang Zhang , Chao Yin, and Xiao Li

Research Article (10 pages), Article ID 4918087, Volume 2020 (2020)

Geological Structural Surface Evaluation Model Based on Unascertained Measure

Kang Zhao , Qing Wang, Yajing Yan, Junqiang Wang, Kui Zhao, Shuai Cao, and Yongjun Zhang

Research Article (7 pages), Article ID 3547384, Volume 2019 (2019)

Hazard Scenarios Related to Submarine Volcanic-Hydrothermal Activity and Advanced Monitoring Strategies: A Study Case from the Panarea Volcanic Group (Aeolian Islands, Italy)

Davide Romano , Alessandro Gattuso , Manfredi Longo , Cinzia Caruso, Gianluca Lazzaro, Andrea Corbo, and Francesco Italiano

Research Article (15 pages), Article ID 8728720, Volume 2019 (2019)

Research Article

The Temperature Evaluation of the Buried Hill Geothermal Reservoirs in the Jizhong Depression, Bohai Bay Basin, China

Yuyang Dong^{1,2}, Jianhui Zeng^{1,2}, Xianzheng Zhao,³ Yanu Wang,^{1,2} Tianhao Chen,^{1,2} Yongchao Zhang,⁴ and Sen Feng^{1,2}

¹State Key Laboratory of Petroleum Resources and Prospecting, China University of Petroleum, Beijing 102249, China

²College of Geosciences, China University of Petroleum, Beijing 102249, China

³Dagang Oilfield Company, PetroChina, Tianjin 300280, China

⁴Qingdao Institute of Marine Geology, China Geological Survey, Qingdao 266071, China

Correspondence should be addressed to Jianhui Zeng; zengjh@cup.edu.cn

Received 15 August 2019; Revised 14 March 2020; Accepted 31 October 2020; Published 23 November 2020

Academic Editor: Glenda Taddia

Copyright © 2020 Yuyang Dong et al. This is an open access article distributed under the Creative Commons Attribution License, which permits unrestricted use, distribution, and reproduction in any medium, provided the original work is properly cited.

The Jizhong Depression is located in the western Bohai Bay Basin, eastern China. The deep strata are mainly composed of carbonate buried hill, and the shallow strata are a mainly siliciclastic deposition. In the present work, the Na-K-Mg triangle diagram and geothermometers were used to investigate the geochemical characteristics of shallow groundwater and reservoir temperature features of three geothermal reservoirs in the depression, including the Ordovician, the Cambrian, and the Precambrian Wumishan Formation. The results showed that the geothermal water in the depression could be divided into three groups: group I, Cl-HCO₃-Na type; group II, Cl-Na type; and group III, Cl-Na-Ca type. By using the Na-K-Mg triangle diagram, group II and group III geothermal water samples were identified as the partially equilibrated water, whose temperature of the geothermal reservoir can be calculated based on the cation geothermometers. The ranges of the calculated temperature of the shallow strata and the deep strata are 91~146°C and 147~176°C, respectively. It has the good results obtained with some cation geothermometers in a geothermal system hosted in carbonate rocks like the studied area. The analysis workflow and calculation data obtained in this work contribute to the evaluation of the temperature field and the exploration and development of the geothermal resources in the Bohai Bay Basin.

1. Introduction

Many countries around the world are engaging in research on new energy, especially on renewable energy, in order to gradually reduce their nation's dependence on traditional fossil fuels. There are roughly 82 countries (regions) making use of geothermal energy directly and 26 countries (regions) using geothermal energy for power generation. China's geothermal resources account for about 16.7% of global resources, especially the medium- and low-temperature geothermal resources, which means that the geothermal energy sector has great development potential. It is shown that there has been a rapid development in geothermal utilization in the past few years

and the installed capacity of geothermal power generation will increase by 1 GWe per year in the next 6 and 7 years [1].

Geothermal and petroleum resources coexist in sedimentary basins. With most of the oilfields in eastern China entering the middle and late stages of development, the difficulty of oil and gas exploitation gradually increases, and the proportion (water content) and the total amount of water in the produced fluid are also increasing. The water content of the old oilfields in the east is more than 90% on average [2]. In a sense, the reservoirs in these oilfields are no longer oil but water. More and more wells have been abandoned in these oilfields when the petroleum reservoir was depleted without economic feasibility. The oilfield has a large amount

of detailed geological data, which provides important basic data for the development and utilization of geothermal resources.

Drilling costs can account for 50% of geothermal projects. If the abandoned oil and gas wells are transformed into geothermal wells after the thermal storage temperature assessment, drilling costs can be greatly reduced and the geothermal project can be launched [3]. In the late stage of oilfield development, abandoned oil and gas wells can be transformed into geothermal wells and utilized as geothermal wells [4, 5]. Kujawa et al. [6, 7] introduced the double-pipe well hole heat exchanger, which is the simplest kind of geothermal borehole heat exchanger, used for heat extraction from abandoned oil and gas wells. In recent years, some scholars have continued their research on obtaining thermal energy from abandoned oil and gas wells [8–10]. Getting geothermal energy from abandoned oil and gas wells has the following four advantages. There is no drilling investment (costs can be saved) and no groundwater extraction (corrosion problems can be avoided), thermal properties of wells are available, and retrofitting well-bore with equipping the inner pipe is a proven technology [11]. In the Bohai Bay Basin, some abandoned oil wells have been retrofitted, such as wells Y1 and L24 in Huabei Oilfield [12] and wells T38-1 and T38-2 in Dagang Oilfield [13]. Huabei Oilfield uses recharge wells to inject water into geothermal reservoirs and then uses geothermal wells to extract hot water to develop geothermal energy. There is a certain distance (minimum 200 m) between recharge wells and geothermal wells to achieve heat exchange [12].

Geothermometry is a method that uses the concentration or concentration ratio of the chemical components to calculate the temperature of an underground geothermal reservoir. The method is based on the hypotheses that water and hydrothermal (secondary) minerals quickly attain the equilibrium condition in the geothermal reservoir and that no water-rock interaction and no interfering process (e.g., mixing and boiling) take place while the geothermal fluid is rising to the earth's surface [14, 15]. In the 1970s–1980s, experts and scholars established a series of geothermometers to estimate the temperature of geothermal reservoirs, including silica geothermometers, cation geothermometers, and isotope geothermometers, which are widely used in the development and utilization of geothermal resources [14–17]. From 1988 to 1992, a series of triangular figures were created for the study of the origin and formation mechanism of geothermal fluids [18, 19]. From 1997 to 2002, some scholars proposed some improvements to the geothermometers. Verma and Santoyo [20] proposed three improved equations for the widely used Na-K, Na-Li, and silica geothermometers and compared them with the equations by Fournier and others, which find that the total propagated errors of the new equation are smaller than the original equation. Bayram [21] and Can [22] developed a new Na-K geothermometer based on artificial neural networks (ANNs), respectively. Bayram also compared seven Na-K geothermometers for predicting geothermal fields and considered that the reservoir temperatures of some geothermal fields in Turkey determined by the new method are consistent with those determined by other methods [21]. Using the Na-K-Mg triangle diagram, Zheng et al. [23] consider that the cation

geothermometer can estimate the water samples in the Guanzhong Basin; the calculation results were similar; and after studying the silica equilibrium with selected geothermal water samples, the results show that chalcedony has a better fit than quartz, which inferred that chalcedony controls the silica concentration in the deep reservoir. By using the Na-K-Mg triangle diagram, cation geothermometers were not applicable in southern Tunisia; Kamel used the Na-Li geothermometer to estimate the temperature of the thermal water, finding that the results obtained are credible, compared with results of previous studies [24]. Nitschke et al. [25] considered that the Na^+/K^+ concentration ratio in fluids is obviously not unequivocally controlled by temperature but is also dependent upon reservoir rock composition. Blasco et al. studied the Tiermas geothermal system in the Jaca-Pamplona Basin, with two groups of different total dissolved solids and waters in the carbonate rock, and results show that there are slight differences in the temperature of depth and in the concentration of some chemical compositions. They also found the good results obtained with cationic geothermometers in a geothermal system of low temperature and hosted in carbonate-evaporitic rocks like the studied area, which may be attributed to the presence of detrital rocks (silicate minerals) in the carbonate-evaporitic reservoir [26].

The Jizhong Depression is a sedimentary basin developed in the Mesozoic and Cenozoic era. The depression is rich in oil and gas resources, the study of which has been quite sufficient [27–31]. Based on the research of Zhang et al., the depression belongs to the type of sedimentary basin nonmagma origin. There are two main heat sources in the depression, one is the conduction heat from the deep earth, and the other is generated by the radioactive materials in the strata, mainly in the forms of conductive heat transfer, with regional hydrothermal convection. The depression has no additional heat source (the heat generated by magma) [32]. The plane distribution characteristics of the heat flow in the study area are related to the relief of the basement, and the basement uplift is a relatively high-temperature zone [33]. At the same time, the hydrodynamic condition is one of the important influencing factors causing the differences in geothermal fields in different regions of the depression. The geothermal reservoirs in the depression are adjacent to the heat resources, and most of them have good cap rock, which mainly includes pore type, fracture type, and fracture-cavern type [34]. He and Ma proposed a conceptual model for the formation mechanism of Ordovician carbonate thermal reservoirs in the North China Plate by analyzing the hydrochemical characteristics, hydrochemical types, and characteristic coefficients [35]. Zhao et al. studied the hydrochemical characteristics of the Baxian sag in the depression, considering that the characteristics could be divided into three types according to their different chemical composition, the origin and formation mechanism of which were also studied [28]. However, the estimation of the geothermal resources in the depression, especially the temperature of the geothermal reservoir, has not received sufficient attention.

This paper analyzes the geochemical characteristics of the geothermal water in the buried hill of the study area and divides these samples into groups. Then, determine whether each group is suitable to calculate the temperature of the

geothermal reservoir with a cation geothermometer and estimate the temperature. After obtaining the calculation results, compare the results with the bottom hole temperature (BHT) to verify the reliability of the results. Through the research of this paper, a scientific basis for the development and utilization of the geothermal resources in the study area will be provided.

2. Basic Geology Settings

2.1. Geological Settings. Located in the western part of the Bohai Bay Basin, the Jizhong Depression is a Mesozoic and Cenozoic sedimentary depression developed in the basement of the ancient platform in North China [4, 33]. With an area of about 3.2×10^4 km², the Jizhong Depression shows a northeast-southwest trend and is bounded by the Yanshan uplift in the north, the Xingheng uplift in the south, the Taihangshan uplift in the west, and the Cangxian uplift in the east. According to the characteristics of the basement relief and fault distribution, the central depression can be divided into several secondary structural units [33]. In general, the depression shows the characteristics of “one convex and two concaves”; that is, the central uplift zone divides the Jizhong Depression into the western and east depression zones. The central swell belt mainly includes Daxing, Niuzhai town, Rongcheng, Gaoyang, Wuji, and Ningjin. The western depression zone mainly includes sags such as Beijing, Xushui, Baoding, and Shijiazhuang. The eastern depression zone mainly includes Langgu, Wuqing, Baxian, Raoyang, Shexian, Shulu, Jinxian, and other sags (Figure 1).

There are three types of faults in the study area: NNE, NE, and SW trending [4, 36]. The NNE-trending faults are the most developed group of faults in this area. They are large in scale, long in extension and steep in dip. In Cenozoic, fault activity was still intense and controlled the Oligocene deposition process. The north-easterly faults are in the same direction as the axial direction of the basement folds, most of which distribute in the axis part of the basement folds and low angle. In comparison, the SW-trending faults are much smaller. As a result, these faults control the area of geothermal fields in the depression.

According to the survey data of geothermal wells in 2015, there are 544 geothermal wells in the Jizhong Depression, accounting for 48.57% of all geothermal wells in Hebei province [37]. Geothermal wells are mainly distributed in the central uplift zone, while oil wells are mainly distributed in various depressions and slopes in the study area. Figure 1 shows the location of geothermal wells and oil wells.

In the Jizhong Depression, the Cenozoic formations compose of Pinyuan Formation (Qp) of Quaternary; Minghuazhen Formation (Nm) and Guantao Formation (Ng) of Neogene; and Dongying Formation (Ed), Shahejie Formation (Es), and Kongdian Formation (Ek) of Paleogene. These formations are all sedimentary rocks. The formations of the buried hill developed in the Paleozoic and Precambrian, and they are dominated by weathered and denuded carbonate which formed during the Ordovician (O), Cambrian (C), Qingbaikou (Qb), and Jixian (Jx) (Figure 2).

2.2. Hydrogeological Settings. There are three geothermal aquifer systems in the Jizhong Depression: Proterozoic-Lower Paleozoic weak alternating area, Upper Paleozoic-Paleogene hydrodynamic blocking area, and Neogene strong alternating area. The west (Taihang mountain) and the north (Yanshan mountain) are the main water supply area [38, 39]. The atmospheric precipitation permeated through the basin along with the carbonate aquifer system or the peripheral deep fault belt. Groundwater flowed mainly from the Taihang mountains in the west of the depression to the southeast, just a small amount flowed from the Yanshan mountains in the north of the depression to the southwest, and a minimal amount came from the Cangxian uplift area. After the groundwater in the surrounding mountains crossed the alternating area at the edge of the basin, the flow transformed into a long-distance horizontal (near horizontal) migration. It absorbed heat from surrounding rock, reacted with the rock sufficiently, and dissolved the soluble components of rock. According to the measured water pressure of the buried hill by drilling, it is converted into the distribution of the current water head, and the distribution diagram of it is drawn (Figure 3). In this region, the groundwater head of the buried hill gradually decreases from the basin periphery to the basin center, forming the movement trend of groundwater from the depression periphery to the center, that is, the characteristics of typical “centripetal flow” [38–40].

2.3. Geothermal Regime Settings. The present geothermal gradient in sedimentary basins is studied through various borehole test temperature data [33]. The present geothermal gradient in the Jizhong Depression is 2.8~3.8°C/100 m, and the average geothermal gradient is 3.2~3.4°C/100 m. In the Beijing-Xushui-Baoding-Shijiazhuang swell belt, which is in the west of the depression, the present geothermal gradient ranges from 2.8°C to 3.2°C/100 m. The ground temperature gradient of the east area, which is the adjacent Niutuo-Rongcheng-Gaoyang uplift area increased by 3.6~3.8°C/100 m. However, the present geothermal gradient in the three oil-bearing depressions of Langgu, Baxian, and Raoyang in the east of Niutuo town, Rongcheng, and Gaoyang uplift decreases to 3.0~3.2°C/100 m. After that, the geothermal gradient in the east increased again, reaching 3.4~3.6°C/100 m in the uplift area of Cangxian county [4, 34]. The present geothermal gradient distribution in the depression is consistent with the underlying basement structure.

By using the oil test temperature data, a section map of the relationship between formation temperature and formation distribution at 3500 m was drawn (Figure 4, the position of the section as shown in Figure 1). According to the collected temperature data, the temperature of buried hills at 3500 m is generally 110~150°C, and that of the depression area is relatively lower (110~124°C). In the uplift area and the swell area inside the depression area, the ground temperature is significantly increased (127~148°C). Figure 4 shows that the temperature of the northwestern uplift area is lower than the eastern uplift area, and the temperature of the convex area of the depression is generally higher than the temperature of the depression at the same depth.

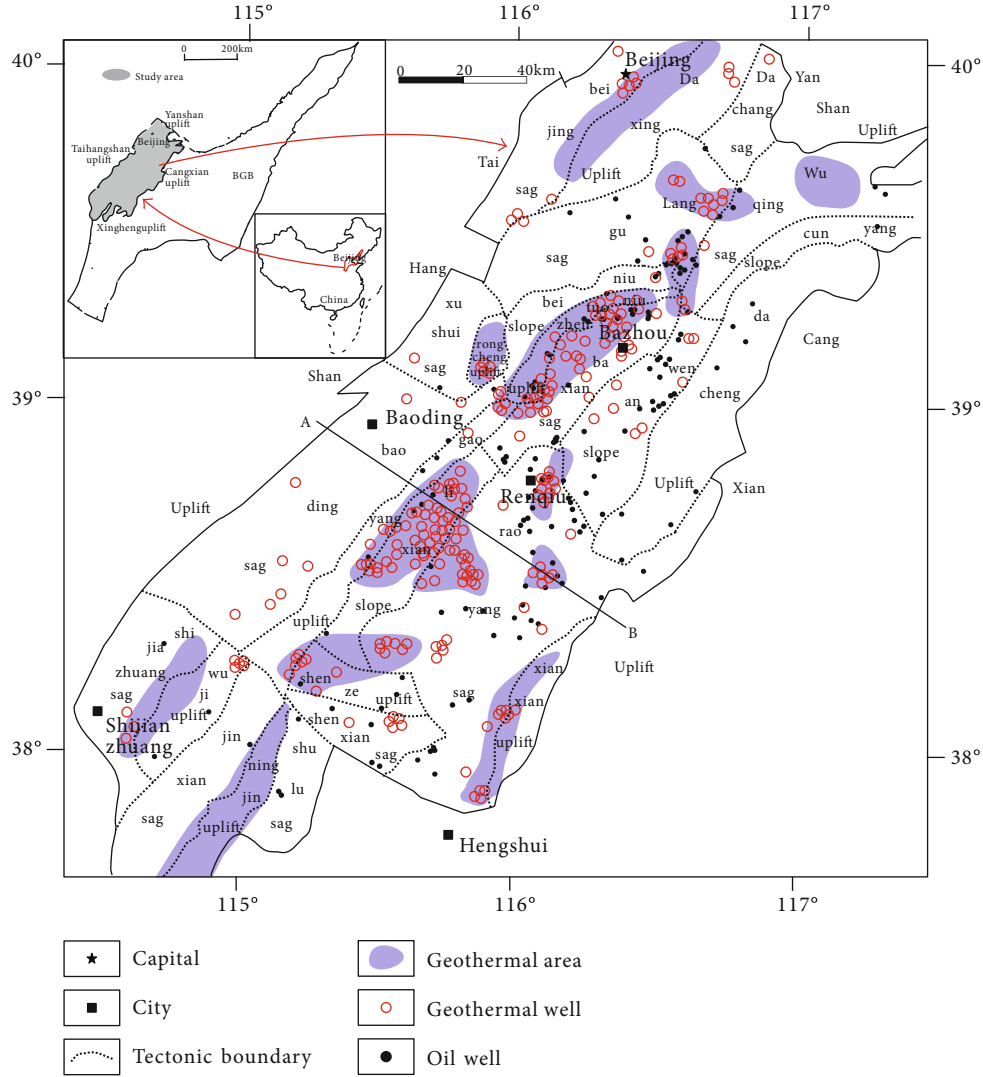


FIGURE 1: Sketch map showing the structure and geothermal area of the Jizhong Depression.

3. Materials and Methods

3.1. Sampling and Analysis. The Huabei Oilfield Research Institute provided hydrochemical data from about 400 groundwater samples. Groundwater samples were obtained from drill stem tests (DST) of oil wells [41]. These wells were drilled between 1970 and 2000. And the obtained water samples were tested by oilfield water analysis testing methods (National Standard SY5523-2000). The cation in the water sample is Na^+ , K^+ , Ca^{2+} , Mg^{2+} , or B^{3+} , and the anion is Cl^- , HCO_3^- , CO_3^{2-} , SO_4^{2-} , Br^- , or I^{3-} .

The collected test results are analyzed to determine whether the test results are accurate. Since a fundamental condition of the electrolytic solution is electrical neutrality, the total number of positive charges carried by the cations in the solution should be equal to the total number of negative charges carried by the anions.

Groundwater is an electrolytic solution with a relatively complex composition. Therefore, groundwater also follows the electrical neutrality equation. The electrical neutrality equation is

$$\sum Zm_c = \sum Zm_a. \quad (1)$$

In the formula, m_a and m_c , respectively, represent the molar concentration of anions and cations, and Z represents the respective charge number of anions and cations.

Although the composition of groundwater is very complicated, there are also differences between major ions and trace elements. Trace elements have little effect on the calculation. Therefore, in the calculation, the trace elements are removed. This article only calculates the electrical neutrality equation of the main ion content.

The components in groundwater are expressed by their constant components. The expression is

$$(\text{Na}^+) + (\text{K}^+) + 2(\text{Ca}^{2+}) + 2(\text{Mg}^{2+}) = (\text{Cl}^-) + (\text{HCO}_3^-) + 2(\text{SO}_4^{2-}). \quad (2)$$

In this test result, the B^{3+} , CO_3^{2-} , Br^- , and I^{3-} contents are very small so that these elements can be omitted in this calculation. There are trace components in the test, and there may

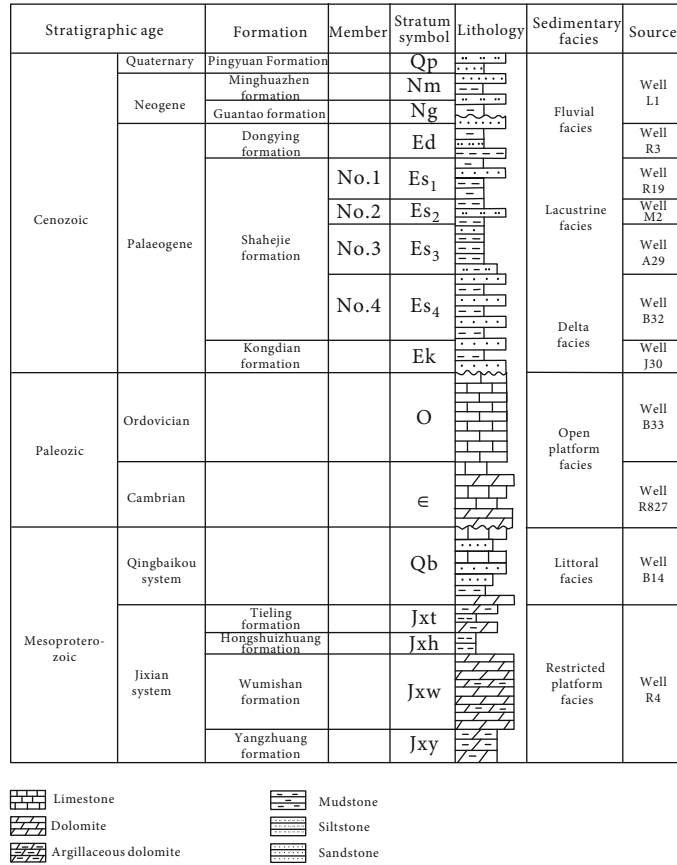


FIGURE 2: Stratigraphic histogram in the study area.

be some errors, but the test results cannot be considered wrong, and the above formula is only an approximate equation. If the test result of the electrical neutral equation is within a certain error range, the test result can be considered correct.

$$E = \frac{(\sum Zm_c - \sum Zm_a)}{(\sum Zm_c + \sum Zm_a)} \quad (3)$$

E stands for charge balance error (unit: %).

If the absolute value of the calculated result is less than 5%, the calculated result is reliable; if the absolute value of the calculated result is higher than 5%, the test result is doubtful.

The formula was used to test all collected sample data, and the absolute value of most of the calculated results was found to be less than 5%. The test results of the collected data were credible, indicating that the analysis results were reasonable. In order to ensure the credibility of the data, we exclude the data with a large absolute value.

3.2. Chemical Geothermometer. Chemical geothermometers were applied to estimate the temperatures of the geothermal reservoirs, including three cation geothermometers (the equilibrium constants for exchange and alteration reactions are temperature dependent). Table 1 lists the formulas for

the calculations used in this research. Moreover, the equilibrium state between thermal water and specific minerals was studied using the Na-K-Mg triangle diagram [18].

4. Results and Discussion

4.1. Hydrochemical Characteristics. The relationship between the total dissolved solids (TDS) and the depth of the geothermal reservoir in the study area is studied. The shallowly buried hill geothermal reservoirs (500~1500 m) have the lowest TDS, which is less than 5 g/L; the middle part of buried hill geothermal reservoirs (1500~3000 m) is 2~15 g/L; and the deeply buried hill geothermal reservoirs (3000~5000 m) are relatively high and have a broader distribution range, ranging from 2 to 45 g/L. Overall, the TDS increases as the depth of geothermal reservoirs increases (Figure 5).

By using cluster analysis of the main ions of the water samples, the water samples in the study area can be divided into three groups (Figure 6). The anions of group I are mainly Cl^- and HCO_3^- , and the cation is mainly Na^+ ; geothermal water is $Cl-HCO_3-Na$ type; and the TDS is relatively low, generally less than 5 g/L. The average sodium chloride coefficient is 1.34, the metamorphic coefficient is -9.3 on average, and the desulfurization coefficient is generally higher than 10.0. The anion of group II is mainly Cl^- , and the cation is mainly Na^+ ; geothermal water is $Cl-Na$ type; and the TDS is

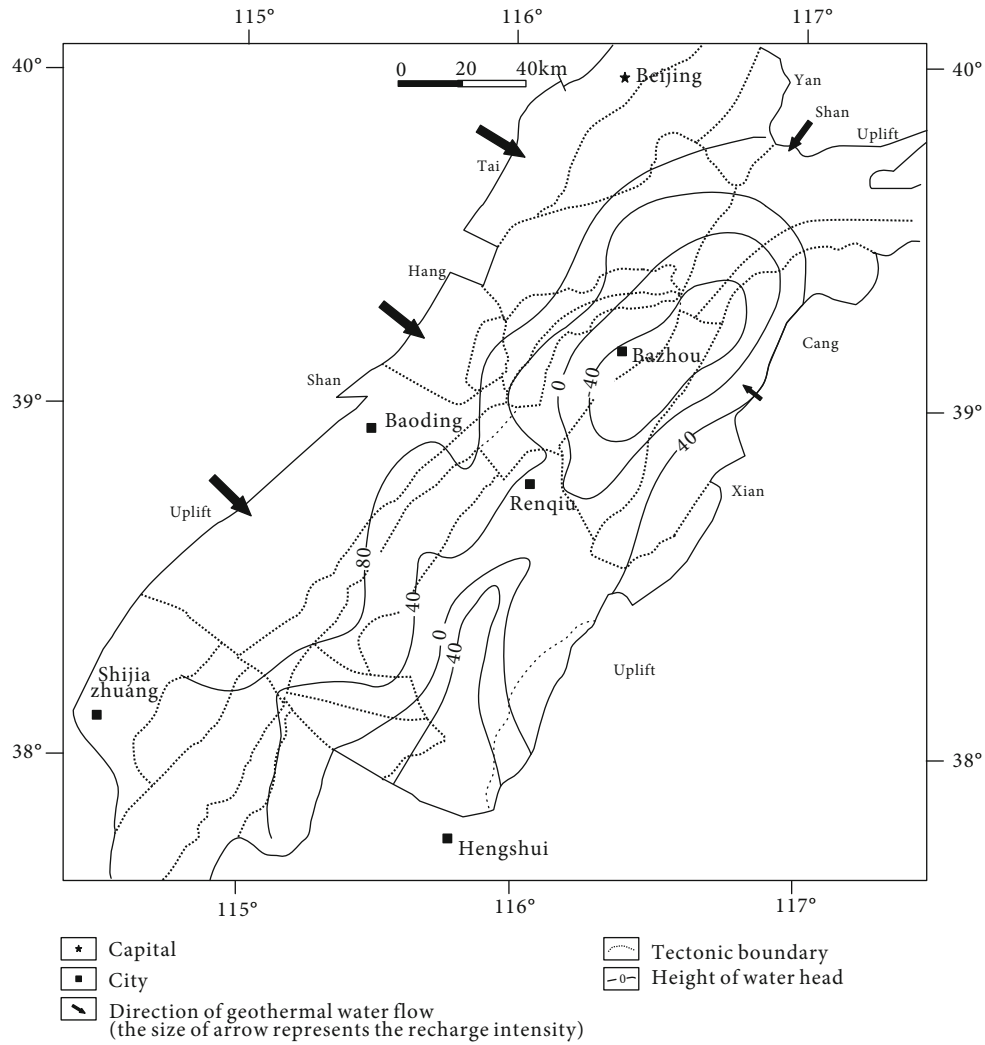


FIGURE 3: Current water head distribution of the geothermal reservoir in the buried hill of the study area.

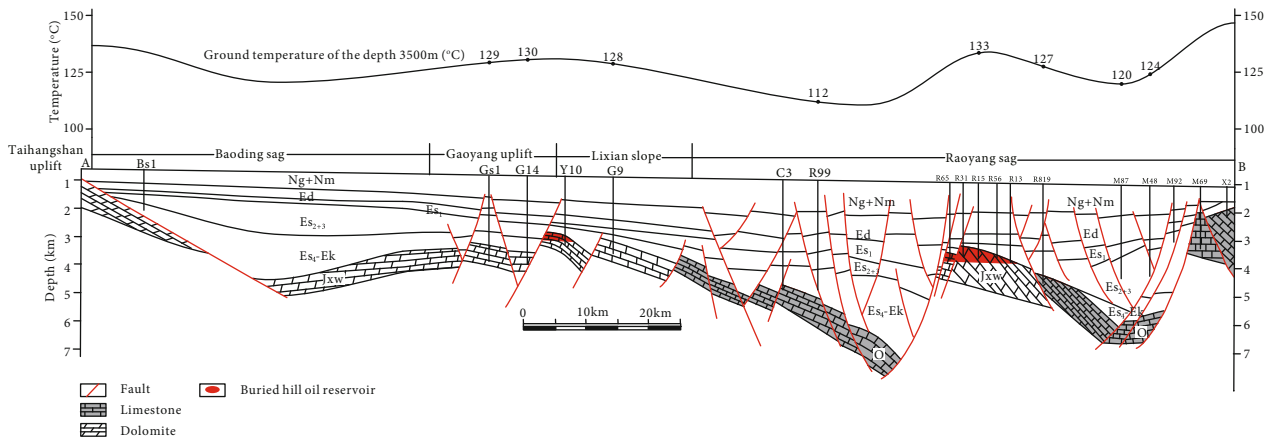


FIGURE 4: Formation (depth 3500 m) temperature and stratigraphic distribution in the study area.

higher than group I, generally 5~20 g/L. The sodium chloride coefficient is 0.96 on average, the metamorphic coefficient is -3.19 on average, and the desulfurization coefficient is 6.4 on

average. The anion of group III is mainly Cl^- , and cations are mainly Na^+ and Ca^{2+} ; geothermal water is Cl-Na-Ca type; and the TDS is the highest in all three groups, more than

TABLE 1: Chemical geothermometers used in this work.

Geothermometer	Calibration	Author
Na-K	$T_{Na-K} = \frac{1390}{1.75 + \log (Na/K)} - 273.15$	Giggenbach (1988)
	$T_{Na-K} = \frac{1217}{1.483 + \log (Na/K)} - 273.15$	Fournier (1979)
K-Mg	$T_{K-Mg} = \frac{4410}{13.95 \log (K^2/Mg)} - 273.15$	Giggenbach et al. (1983)
Na-K-Ca	$T_{Na-K-Ca} = \frac{1647}{\log (Na/K) + \beta \left[\log \left(\sqrt{Ca/Na} \right) + 2.06 \right] + 2.47} - 273.15$	Fournier and Truesdell (1973)

Concentration units for the elements involved are all in mg/L. The empirical coefficient β value is determined based on the calculation result. When the calculated temperature is less than 100°C, the empirical coefficient β is 4/3; when the calculated temperature is higher than 100°C, the empirical coefficient β is 1/3.

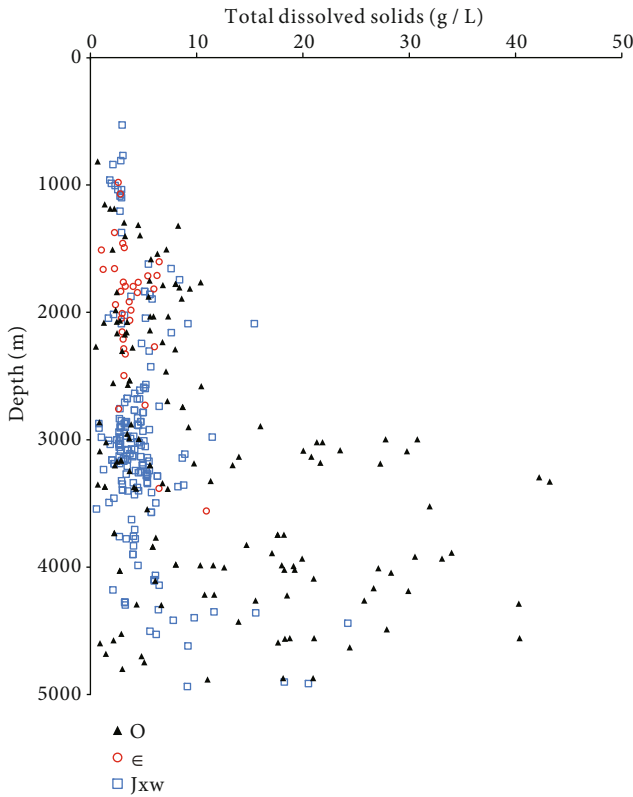


FIGURE 5: Depth and TDS for geothermal water in the study area.

20 g/L. The sodium chloride coefficient is 0.61 on average, the metamorphic coefficient is 3.8 on average, and the desulfurization coefficient is generally less than 3.0 (Table 2).

The horizontal distribution of water samples in the study area is studied (Figure 7). Group I geothermal water is mainly distributed in the west and north of the study area, group II geothermal water is mainly distributed in the middle and south of the study area, and group III geothermal water is distributed in the eastern Bazhou, within a small area in the north of Hengshui.

Comparing the current water head distribution map (Figure 3) with the buried hill geothermal water distribution

map (Figure 7), it is found that there is a good correspondence between the types of geothermal water and the “centripetal flow” feature in the hydrological characteristics.

The samples were classified into three groups by using cluster analysis, and the hydrochemical characteristics of each group were also compared and analyzed. The sealing of geothermal water has also been studied, mainly considering three types of parameters, which were the sodium chloride coefficient ($r(Na^+)/r(Cl^-)$), metamorphic coefficient ($r(Cl^- - Na^+)/r(Mg^{2+})$), and desulfurization coefficient ($r(SO_4^{2-}) \times 100/r(Cl^-)$).

The sodium chloride coefficient is a parameter that reflects the degree of groundwater concentration and deterioration. The chemical properties of chloride ions in this coefficient are stable, and there is a little reflection of adsorption, precipitation, and exchange, while sodium ions may decrease due to chemical reactions such as adsorption and precipitation. From the perspective of sedimentology, the sodium chloride coefficient of water in marine formations is relatively small, the sodium chloride coefficient of land is relatively large, and the sodium chloride coefficient of salt lakes is close to 1. From the perspective of water concentration and deterioration, the higher the concentration or deterioration, the lower the sodium chloride coefficient [42].

The desulfurization coefficient is an important parameter reflecting the degree of desulfurization and the reduction of groundwater. Chlorine ion and sulfate ion are the two anions with the highest content in groundwater. Due to the differences in the extensiveness and stability of the two ion sources, the content of sulfate is usually not as high as that of chloride ion. In the groundwater, sulfate ions mainly come from the dissolution of gypsum ($CaSO_4 \cdot 2H_2O$) or other sulfate rocks, and sulfur, which is originally insoluble in water, enters the groundwater in large quantities through the oxidation of sulfides. On the other hand, in the reducing environment, when there is organic matter, the desulfurization bacteria can reduce SO_4^{2-} to H_2S . Therefore, the higher the degree of formation closure, the lesser the external sulfate supply and the stronger the degree of sulfate reduction, resulting in a smaller desulfurization coefficient in the groundwater. However, when there are gypsum salts, coal measures, and metal

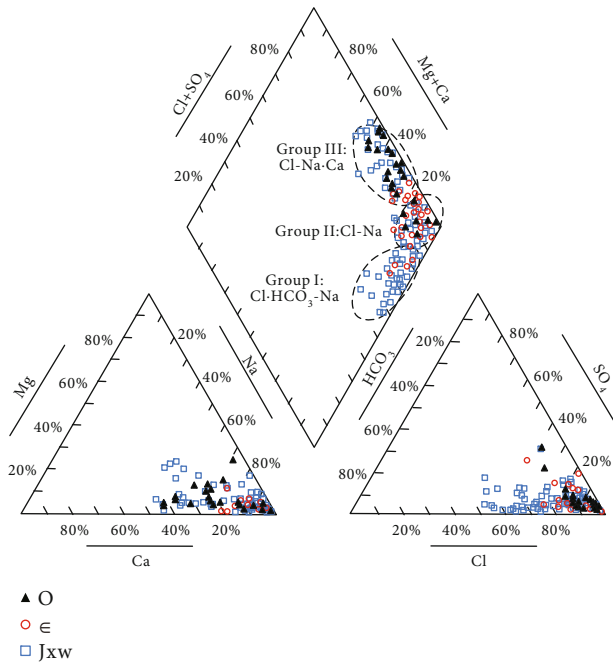


FIGURE 6: Piper diagram of geothermal water in the buried hill of the study area.

sulfide deposits in the local formation, the sulfate content abnormally increases, leading to a significant increase in the desulfurization coefficient [42].

The metamorphic coefficient reflects the degree of ion exchange during the migration of formation water. In a closed environment, the content of unstable ions in groundwater tends to decrease, while the relative content of ions with high stability continues to increase. The main reason for the change in the relative content of groundwater ions is the ion exchange effect. Under this effect, the anions that are less stable (e.g., CO_3^{2-} and HCO_3^-) are reduced first, leaving more stable chloride ions. After that, the cations exchanged, and the highly active magnesium ions were replaced by the more stable calcium ions. The metamorphic coefficient can be used to characterize the metamorphic process. The greater the burial depth, the better the sealing conditions and the longer the continuous geological time. In general, the longer the time of water-rock interaction, the more ion exchange will be and the higher the deterioration coefficient becomes [26, 42].

Figure 5 indicates that the TDS of the geothermal water increases with the increase of depth. From group I to group III, the TDS of the geothermal water also shows an increasing trend. Studying the relationship between TDS and three types of coefficients (sodium chloride coefficient, desulfurization coefficient, and metamorphic coefficient), it is found that the sodium chloride coefficient and the desulfurization coefficient are gradually decreasing, and the metamorphic coefficient is gradually increasing, which indicates that with the increase of depth, the reduction of the three groups (from group I to group III) is getting better, and water-rock interaction is getting stronger (Figure 8).

4.2. Temperatures of Geothermal Reservoirs

4.2.1. Geothermometric Applications. The water-rock equilibrium state should be judged before applying cation geothermometers. The cation geothermometers based on the equilibrium of Na-K, Na-K-Ca, and K-Mg are widely used to evaluate the geothermal reservoir temperature. Sometimes the temperature calculated by the cation geothermometers has a significant deviation from the actual temperature. The main problem is the use of unreasonable water samples. It is relatively difficult to use pH and concentrations such as Cl^- , SO_4^{2-} , and HCO_3^- to eliminate inappropriate water samples. Giggenbach first proposed the Na-K-Mg triangle diagram to evaluate the water-rock equilibrium state and distinguish three different types (immature water, partially equilibrated water, and fully equilibrated water) of water samples. The distribution in the figure can be used to determine whether the minerals in the geothermal water have reached saturation and whether geothermal water is suitable for cation geothermometers. Fully equilibrated water means that the dissolved minerals in the geothermal water and the surrounding rock have reached the equilibrium state. At this time, the results calculated according to the Na-K geothermometer and the K-Mg geothermometer are equal, and the results should be located at the intersection of partially equilibrated water and fully equilibrated water scales in the Na-K-Mg triangle diagram [18, 43–45].

The Na, K, and Mg ion contents of the buried hill geothermal water collected in the study area are projected into the Na-K-Mg triangle diagram (Figure 9). The geothermal water sample of group I is close to the Mg end-member in the lower right corner, and it belongs to immature water. The result reflects that the sodium and potassium minerals in the geothermal water is not saturated. In principle, it is unreasonable to estimate the equilibrium temperature by using these immature water samples. The geothermal water point of group I fits into a dilution line, and the intersection point with the fully equilibrated water line is the temperature at which the geothermal water reaches equilibrium, which is approximately 173°C. It indicates that geothermal water is mixed with cold water in the shallow strata so that the dissolved equilibrium water is affected by cold water and became immature water. The geothermal water samples of group II and group III are located in the partially equilibrated water zone, indicating that they mix less with cold water, which is partially equilibrated water, and the temperature can be estimated by cation geothermometers.

4.2.2. Cation Geothermometer. The cation geothermometer is used to estimate the heat exchange temperature of the deep buried hill geothermal system in the Jizhong Depression. Table 3 shows the calculation results. For the same geothermal water system, the calculation obtained with different geothermometers is quite different. Therefore, it is necessary to discuss the applicability of various temperature scales with the measured data.

The temperature of geothermal reservoirs calculated by the Na-K geothermometer is higher than that by the K-Mg geothermometer. For temperature changes, the chemical reaction of the K-Mg geothermometer reaches the equilibrium

TABLE 2: Geochemical characteristics of geothermal water in the buried hill of the study area.

Group	TDS (g/L)	Hydrochemical type		Main cation and anion (percentage of meq)	Ionic ratio (Min ~ Max/average)		
		Surin classification	Shu kraft classification		$r(\text{Na}^+)/r(\text{Cl}^-)$	$r(\text{Cl}^- - \text{Na}^+)/r(\text{Mg}^{2+})$	$r(\text{SO}_4^{2-}) \times 100/r(\text{Cl}^-)$
I	<5	NaHCO ₃	Cl-HCO ₃ -Na	Cl ⁻ (52%) HCO ₃ ⁻ (37%) Na ⁺ (83%)	$\frac{1.21 \sim 2.51}{1.34}$	$\frac{-45.9 \sim 9.6}{-9.3}$	$\frac{8.1 \sim 48.1}{14.4}$
II	5~20	NaHCO ₃ and CaCl ₂	Cl-Na	Cl ⁻ (92%) Na ⁺ (90%)	$\frac{0.81 \sim 1.11}{0.96}$	$\frac{-30.4 \sim 12.5}{-3.2}$	$\frac{1.4 \sim 13.3}{6.4}$
III	>20	CaCl ₂	Cl-Na-Ca	Cl ⁻ (89%) Na ⁺ (58%) Ca ²⁺ (30%)	$\frac{0.32 \sim 1.05}{0.61}$	$\frac{-9.3 \sim 16.2}{3.8}$	$\frac{0.3 \sim 3.4}{2.6}$

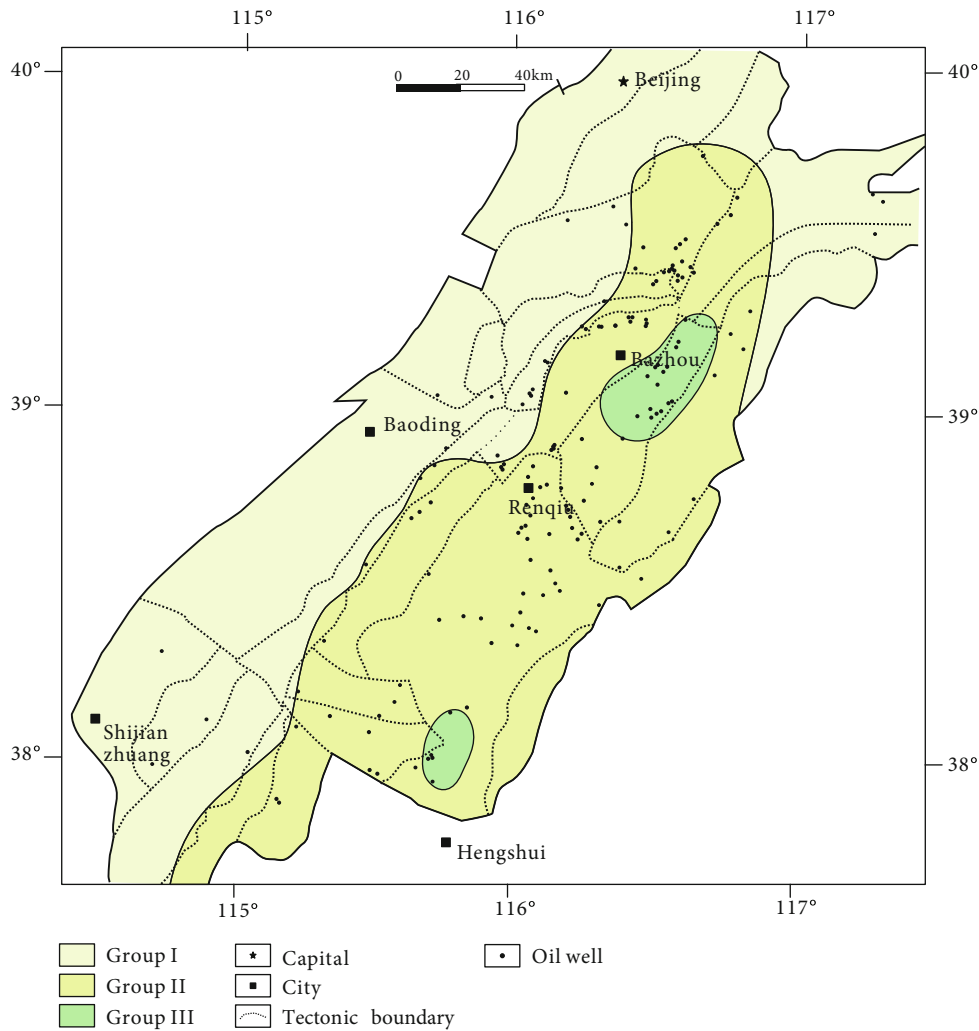


FIGURE 7: Three different types of buried hill geothermal water in the study area.

faster than that of the Na-K geothermometer, even at low temperatures. The equilibrium of the K-Mg geothermometer is continuously broken and rebalanced by the conduction cooling or the mixing with the shallow cold water during the process of rising water from the deep to the surface so that the K-Mg geothermometer calculation results are biased toward the shallow heat exchange temperature and the drilling

temperature. In general, the geothermal system in the study area has a multistage geothermal reservoir. During the processes from a deep geothermal reservoir to a shallow geothermal reservoir, the geothermal water reestablishes a new water-rock equilibrium state. In this process, the equilibrium state of Na⁺/K⁺ changes slower, which is consistent with the deep geothermal reservoir, while the equilibrium state of K⁺/Mg²⁺

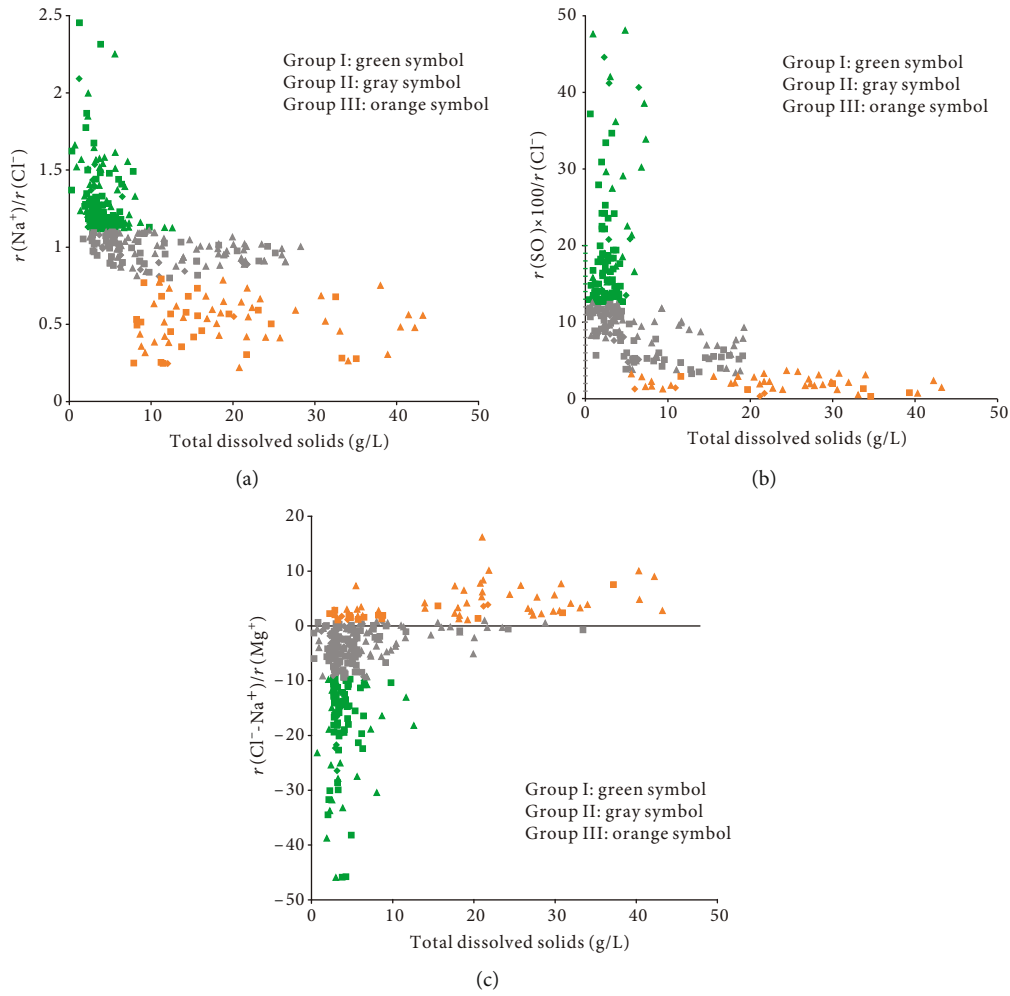


FIGURE 8: Relationship between TDS and three coefficients of the geothermal water in the study area. (a) Sodium chloride coefficient. (b) Desulfurization coefficient. (c) Metamorphic coefficient. Triangle: Ordovician samples. Diamond: Cambrian samples. Square: Jixian samples.

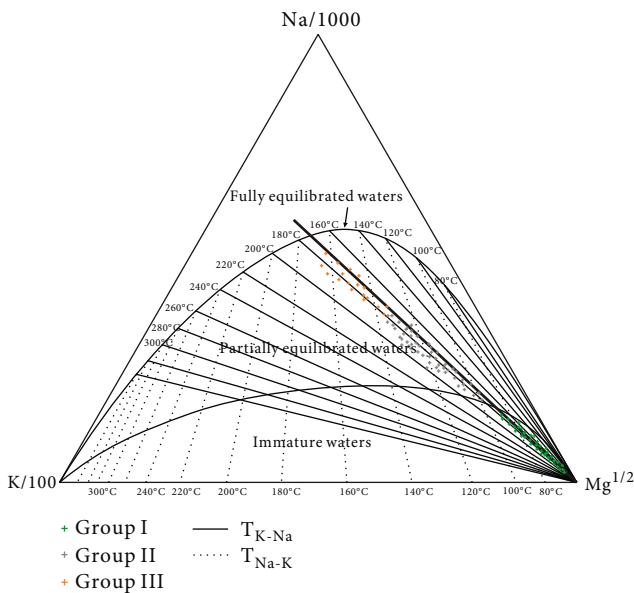


FIGURE 9: Na-K-Mg triangle diagram of the geothermal water in the buried hill of the study area.

changes faster, and the water-rock equilibrium state is reestablished in the shallow geothermal reservoir. Therefore, in the water samples, the equilibrium state of Na^+/K^+ is close to the deep geothermal reservoir, and the equilibrium state of $\text{K}^+/\text{Mg}^{2+}$ is close to the shallow geothermal reservoir. So the Na-K geothermometer is suitable for calculating the deep geothermal reservoir, and the K-Mg geothermometer is suitable for calculating the shallow geothermal reservoir. Based on the calculation results of the K-Mg geothermometer, the ranges of the shallow strata are 91~146°C. And based on the calculation results of the Na-K geothermometer, the ranges of the deep strata are 147~176°C.

As shown in Table 3, the temperature calculated by the K-Mg geothermometer ($T_{\text{K-Mg}}$; the temperature calculated by the Na-K geothermometer is $T_{\text{Na-K}}$, and the temperature calculated by the Na-K-Ca geothermometer is $T_{\text{Na-K-Ca}}$) is closer to the observed temperature, which reflects that the equilibrium state of the K-Mg is continuously broken and rebalanced during the upward movement of the deep geothermal water. So the calculation is closer to the temperature of the shallow geothermal water. As mentioned earlier,

TABLE 3: Observed temperature and the calculation results of geothermal reservoirs.

Well	Depth (m)	Group	Na-K	K-Mg	Geothermometer (°C)		Observed temperature (°C)
					Na-K-Ca ($\beta = 4/3$)	Na-K-Ca ($\beta = 1/3$)	
B5	2164	II	157.0	120.1	162.8	158.9	101
B9	1938	II	149.8	98.1	202.1	165.1	98
B10	1763	II	163.3	111.8	207.5	173.7	92
B12	1891	II	170.2	131.4	219.5	180.0	98
B13	2567	II	160.0	126.5	211.3	172.3	106
B14	1796	II	160.5	97.6	259.4	183.6	92
B17	2008	II	156.6	111.8	229.8	176.4	100
B21	3544	III	166.2	163.1	212.8	176.3	133
B24	2496	II	156.7	105.2	205.8	169.9	103
L13	2158	II	169.2	126.9	183.2	170.2	102
L16	1743	II	170.0	127.4	219.5	180.0	90
L23	3242	III	163.6	145.0	223.2	176.9	122
L24	3270	III	175.9	120.0	212.8	176.3	123
L25	3282	III	165.8	118.2	191.7	171.1	122
M10	1894	II	145.9	113.9	267.2	187.4	94
M14	1709	II	155.6	91.6	142.0	158.7	89
M15	2728	II	165.2	116.0	188.3	170.3	110
M17	2566	II	165.5	114.9	200.8	173.4	104
M23	2244	II	164.3	106.8	121.4	149.8	104
M25	3760	III	174.6	105.6	185.2	163.2	142
N19	2878	II	160.5	123.7	203.3	170.9	107
R4	3152	II	159.7	125.4	181.3	164.7	113
R6	3414	III	167.1	138.0	247.2	183.7	130
R7	3072	II	161.6	116.8	228.7	177.1	110
R8	3400	III	164.2	133.1	213.0	175.1	126
R11	2636	II	162.6	121.7	209.2	173.5	105
R16	3186	II	154.2	113.4	174.2	160.6	112
R17	3168	II	157.7	122.2	192.8	166.9	111
R23	3626	III	161.9	123.6	199.2	170.6	137
R26	3140	II	149.2	128.7	187.3	170.2	112
R29	3284	II	167.9	139.3	176.7	168.3	118
R31	3337	III	163.0	127.9	259.4	183.6	124
R32	3145	II	157.4	110.3	203.5	168.9	113
R34	3123	II	162.0	118.1	153.5	159.2	113
R35	3078	II	159.7	115.5	203.7	170.4	110
R81	3244	II	159.8	132.0	246.8	179.5	115
R83	3370	III	161.9	110.7	206.3	172.8	121
R841	3410	III	220.0	174.0	164.0	126.0	122
S3	3985	III	171.8	127.7	213.8	179.7	131
S13	3185	II	171.0	126.9	235.3	183.7	114
Y1	3054	II	154.1	112.0	173.4	160.4	111
Y5	3089	II	155.2	146.6	176.5	161.8	114
Y6	2163	II	141.2	119.1	171.1	159.5	102
Y8	2302	II	156.5	128.0	167.2	159.9	106
Y11	2063	II	153.8	107.2	160.5	157.2	100
Y13	2031	II	165.6	124.3	180.0	168.7	99
Y14	1507	II	148.0	105.4	157.4	151.6	86
Y15	3347	III	160.6	127.6	229.8	176.4	120

TABLE 3: Continued.

Well	Depth (m)	Group	Geothermometer (°C)				Observed temperature (°C)
			Na-K	K-Mg	Na-K-Ca ($\beta = 4/3$)	Na-K-Ca ($\beta = 1/3$)	
Y18	3187	II	174.8	146.1	233.8	185.6	114
Y19	1840	II	147.9	92.9	127.1	145.6	93
Y20	3522	III	175.1	150.0	147.8	164.6	134

when the dissolved minerals in the geothermal water and the surrounding rock are close to the equilibrium state, the position of the sample point in the Na-K-Mg triangle diagram is closer to the fully equilibrated water line. For example, T_{K-Mg} of well B21 (163.1°C) is close to T_{Na-K} (166.2°C). It is reflected that in the process of the geothermal water rising from the deep to the surface, there is little cold water mixed or nearly adiabatic cooling, and ion exchange is infrequent. In the areas with high Ca ion concentration, the results of T_{K-Mg} and T_{Na-K} are abnormal. For example, the Ca ion concentration reached 1172.3 mg/L in the water sample of well R841, and the results of T_{K-Mg} (174.0°C) and T_{Na-K} (220.0°C) are abnormal. In this case, the Na-K-Ca geothermometer is suitable. The calculation result was 126.0°C. Since the observed temperature of the water sample in this study is higher than 100°C and the Na-K-Ca geothermometer ($\beta = 4/3$) is generally used to calculate geothermal water with a temperature less than 100°C, the calculation results are generally abnormal.

According to drilling data, with overlying sandstone strata, well R8 is a buried hill thermal reservoir of the dolomite at a depth of 3400 m. Well L23 is a buried hill thermal reservoir of the dolomite at a depth of 3242 m, and the overlying strata are conglomerate. Other wells in the study area have similar characteristics. The calculation results are approximate to the observed temperature, which may be attributed to the presence of detrital rocks (silicate minerals) in the buried hill reservoir.

5. Conclusions

In this study, all the samples were divided into three groups using cluster analysis of the major elements. The anions of group I are mainly Cl^- and HCO_3^- , and the cation is mainly Na^+ ; the geothermal water is Cl- HCO_3^- -Na type; and the TDS is less than 5 g/L. The anion of group II is mainly Cl^- , and the cation is mainly Na^+ ; the geothermal water is Cl-Na type; and the TDS is 5~20 g/L. The anion of group III is mainly Cl^- , and cations are mainly Na^+ and Ca^{2+} ; the geothermal water is Cl-Na-Ca type; and the TDS is more than 20 g/L.

It is found that the sodium chloride coefficient and the desulfurization coefficient are gradually decreasing and the metamorphic coefficient is gradually increasing, which indicates that with the increase of depth, the reduction of the three groups (from group I to group III) is getting better, and water-rock interaction is getting stronger.

Using the Na-K-Mg triangle diagram, it is found that group I is immature water, group II and group III are partially equilibrated water, and the latter two groups can use

cation geothermometers to evaluate geothermal temperature. There are differences in the calculation results of different water geothermometers for the same water sample. The Na-K geothermometer is suitable for calculating the deep geothermal reservoir, and the K-Mg geothermometer is suitable for calculating the shallow geothermal reservoir. In the areas with high Ca ion concentration, the Na-K-Ca geothermometer is suitable. Based on the calculation results of the K-Mg geothermometer, the ranges of the shallow strata are 91~146°C. And based on the calculation results of the Na-K geothermometer, the ranges of the deep strata are 147~176°C.

It has the good results obtained with some cation geothermometers, such as the Na-K geothermometer, in a geothermal system hosted in carbonate rocks like the studied area. This unusual situation may be attributed to the presence of detrital rocks (silicate minerals) in the carbonate reservoir of the buried hill.

At present, in Huabei Oilfield, some abandoned oil wells have been retrofitted, which uses recharge wells to recharge water into geothermal reservoirs and geothermal wells to extract hot water to develop geothermal energy. Studying geochemical characteristics of geothermal water reservoirs will help to select the water injected into the formation, which will protect the reservoir during water injection and production and prevent wellbore corrosion. At the same time, due to the early drilling time of many wells in the study area and the lack of geothermal data or inaccurate data in some wells, the research in this paper can be used to estimate the temperature of deep reservoirs in the study area and provide reference for the development of geothermal resources.

Data Availability

Readers can obtain the relevant data from the Huabei Oilfield Research Institute.

Conflicts of Interest

The authors declare that they have no conflicts of interest.

Acknowledgments

This study was financially supported by the National Science and Technology Special Grant (No. 2016ZX05006-001). Thanks are also given to Huabei Oilfield Company of PetroChina, which provided all the related dates of the Jizhong Depression.

References

- [1] J. Zhu, K. Hu, X. Lu, X. Huang, K. Liu, and X. Wu, "A review of geothermal energy resources, development, and applications in China: current status and prospects," *Energy*, vol. 93, pp. 466–483, 2015.
- [2] S. J. Wang, J. H. Yan, M. Li, K. W. Li, and S. B. Hu, "New advances in the study of oilfield geothermal resources evaluation," *Chinese Journal of Geology*, vol. 49, pp. 771–780, 2014.
- [3] E. Barbier, "Geothermal energy technology and current status: an overview," *Renewable and Sustainable Energy Reviews*, vol. 6, no. 1-2, pp. 3–65, 2002.
- [4] H. B. Liang, Z. Qian, S. L. Xin, K. J. Zhao, and L. R. Zhu, "Assessment and development of geothermal resources in Jizhong depression," *China Petroleum Exploration*, vol. 15, no. 5, pp. 63–68, 2010.
- [5] J. Y. Wang, N. S. Qiu, S. B. HU, and L. J. He, "Advancement and developmental trend in the geothermics of oil fields in China," *Earth Science Frontiers*, vol. 24, pp. 1–12, 2017.
- [6] T. Kujawa, W. Nowak, and A. A. Stachel, "Analysis of the exploitation of existing deep production wells for acquiring geothermal energy," *Journal of Engineering Physics and Thermophysics*, vol. 78, no. 1, pp. 127–135, 2005.
- [7] T. Kujawa, W. Nowak, and A. A. Stachel, "Utilization of existing deep geological wells for acquisitions of geothermal energy," *Energy*, vol. 31, no. 5, pp. 650–664, 2006.
- [8] A. P. Davis and E. E. Michaelides, "Geothermal power production from abandoned oil wells," *Energy*, vol. 34, no. 7, pp. 866–872, 2009.
- [9] W. L. Cheng, T. T. Li, Y. L. Nian, and C. L. Wang, "Studies on geothermal power generation using abandoned oil wells," *Energy*, vol. 59, pp. 248–254, 2013.
- [10] J. D. Templeton, S. A. Ghoreishi-Madiseh, F. Hassani, and M. J. Al-Khawaja, "Abandoned petroleum wells as sustainable sources of geothermal energy," *Energy*, vol. 70, pp. 366–373, 2014.
- [11] Y. L. Nian and W. L. Cheng, "Insights into geothermal utilization of abandoned oil and gas wells," *Renewable and Sustainable Energy Reviews*, vol. 87, pp. 44–60, 2018.
- [12] Y. Z. Wei, F. Q. Wang, and B. Y. Ren, "Drainage and production by using geothermal in Huabei oil region," *Oil Drilling & Production Technology*, vol. 31, pp. 93–95, 2009.
- [13] Q. S. Dong, X. L. Huang, Z. H. Lang, and Z. Y. Yang, "Technical analysis on transforming abandoned oil well into geothermal well," *Exploration Engineering*, vol. 43, pp. 18–21, 2016.
- [14] R. O. Fournier, "Chemical geothermometers and mixing models for geothermal systems," *Geothermics*, vol. 5, no. 1-4, pp. 41–50, 1977.
- [15] R. O. Fournier, "Geochemical and hydrologic considerations and the use of enthalpy-chloride diagrams in the prediction of underground conditions in hot-spring systems," *Journal of Volcanology and Geothermal Research*, vol. 5, no. 1-2, pp. 1–16, 1979.
- [16] C. Fouillac and G. Michard, "Sodium/lithium ratio in water applied to geothermometry of geothermal reservoirs," *Geothermics*, vol. 10, no. 1, pp. 55–70, 1981.
- [17] S. Arnorsson, "Chemical equilibria in Icelandic geothermal systems—implications for chemical geothermometry investigations," *Geothermics*, vol. 12, no. 2-3, pp. 119–128, 1983.
- [18] W. F. Giggenbach, "Geothermal solute equilibria. Derivation of Na-K-Mg-Ca geothermometers," *Geochimica et Cosmochimica Acta*, vol. 52, no. 12, pp. 2749–2765, 1988.
- [19] W. F. Giggenbach and R. B. Glover, "Tectonic regime and major processes governing the chemistry of water and gas discharges from the Rotorua geothermal field, New Zealand," *Geothermics*, vol. 21, no. 1-2, pp. 121–140, 1992.
- [20] S. P. Verma and E. Santoyo, "New improved equations for SiO_2 geothermometers by outlier detection and rejection," *Journal of Volcanology and Geothermal Research*, vol. 79, no. 1-2, pp. 9–23, 1997.
- [21] A. Ferhat Bayram, "Application of an artificial neural network model to a Na–K geothermometer," *Journal of Volcanology and Geothermal Research*, vol. 112, no. 1-4, pp. 75–81, 2001.
- [22] I. Can, "A new improved Na/K geothermometer by artificial neural networks," *Geothermics*, vol. 31, no. 6, pp. 751–760, 2002.
- [23] Z. Xilai, H. Armannsson, L. Yongle, and Q. Hanxue, "Chemical equilibria of thermal waters for the application of geothermometers from the Guanzhong basin, China," *Journal of Volcanology and Geothermal Research*, vol. 113, no. 1-2, pp. 119–127, 2002.
- [24] S. Kamel, "Application of selected geothermometers to Continental Intercalaire thermal water in southern Tunisia," *Geothermics*, vol. 41, pp. 63–73, 2012.
- [25] F. Nitschke, S. Held, T. Neumann, and T. Kohl, "Geochemical characterization of the Villarrica geothermal system, Southern Chile, part II: site-specific re-evaluation of SiO_2 and Na-K solute geothermometers," *Geothermics*, vol. 74, pp. 217–225, 2018.
- [26] M. Blasco, L. F. Auqué, M. J. Gimeno, P. Acero, and M. P. Asta, "Geochemistry, geothermometry and influence of the concentration of mobile elements in the chemical characteristics of carbonate-evaporitic thermal systems. The case of the Tiermas geothermal system (Spain)," *Chemical Geology*, vol. 466, pp. 696–709, 2017.
- [27] J. C. Shen, X. G. Wang, L. F. Jia, and L. H. Gong, "The differences in the development of the geothermal reservoirs of the Guantao Group and conditions of well completion in the Jizhong and Huanghua depressions," *Hydrogeology & Engineering Geology*, vol. 3, no. 8, pp. 40–43+54, 2004.
- [28] X. Z. Zhao, F. M. Jin, Q. Wang, C. Y. Han, and X. Y. Dong, "Exploration and discovery of subtle deep buried hill and buried hill inner curtain hydrocarbon reservoir in Jizhong sag," *China Petroleum Exploration*, vol. 19, pp. 10–21, 2014.
- [29] C. H. Gao, M. Zha, X. Z. Zhao, and P. Peng, "Migration systems and hydrocarbon accumulation models of buried hill reservoirs in Jizhong Depression," *Lithologic Reservoirs*, vol. 27, pp. 26–30+37, 2015.
- [30] C. H. Gao, M. Zha, X. Z. Zhao, and F. M. Jin, "Hydrocarbon accumulation models and their main controlling factors in the deep buried hills of the Jizhong Depression, Bohai Bay Basin," *Natural Gas Industry*, vol. 37, pp. 52–59, 2017.
- [31] Y. M. Zhang, J. Z. Tian, D. X. Yang et al., "Accumulation conditions and exploration direction of Cambrian Fujunshan Formation inside buried hills in Jizhong depression," *China Petroleum Exploration*, vol. 24, pp. 297–312, 2019.
- [32] Y. Zhang, J. Y. Feng, Z. L. He, and P. W. Li, "Classification of geothermal systems and their formation key factors," *Earth Science Frontiers*, vol. 24, pp. 190–198, 2017.
- [33] J. Chang, N. S. Qiu, X. Z. Zhao et al., "Present-day geothermal regime of the Jizhong depression in Bohai Bay Basin, East China," *Chinese Journal of Geophysics*, vol. 59, pp. 1002–1016, 2016.

- [34] Y. M. Zhang, J. Chang, N. Liu et al., “Present-day temperature–pressure field and its implications for the geothermal resources development in the Baxian area, Jizhong Depression of the Bohai Bay Basin,” *Natural Gas Industry B*, vol. 5, no. 3, pp. 226–234, 2018.
- [35] X. He and Y. Ma, “Hydrochemical features and formation mechanism of the Ordovician carbonate reservoir in North China Plate,” *Safety and Environmental Engineering*, vol. 26, pp. 9–15, 2019.
- [36] D. F. He, Y. Q. Cui, Y. Y. Zhang et al., “Structural genetic types of paleoburied hill in Jizhong depression, Bohai Bay Basin,” *Acta Petrologica Sinica*, vol. 33, pp. 1338–1356, 2017.
- [37] J. Li and Z. G. Zhang, “Characteristics of geothermal resources in Jizhong depression (Hebei region),” *Journal of Hebei University of Technology*, vol. 47, pp. 113–120, 2018.
- [38] J. H. Du, H. W. Zou, B. S. Fei, H. Y. Lei, F. Z. Zhang, and Y. M. Zhang, *Buried hill composite hydrocarbon accumulation zone of Jizhong depression*, Science Press, 2002.
- [39] B. J. Zhang, Y. L. Sun, X. L. Kang, L. Du, F. Xu, and Y. Y. Hu, “The study of formation conditions of karst geothermal water in Beijing and its peripheral areas based on hydrochemical analysis,” *Urban Geology*, vol. 12, pp. 11–19, 2017.
- [40] F. Li and J. H. Zeng, “Characterization of origin and evolution of formation water in buried hill of Jizhong depression, China, using multivariate statistical analysis of geochemical data,” *Geofluids*, vol. 2017, Article ID 5290686, 15 pages, 2017.
- [41] S. H. Wu, Q. Z. Cai, and S. M. Shi, *Oilfield geology*, Petroleum Industry Press, 2011.
- [42] J. H. Zeng, *Geofluids in sedimentary basins*, China University of Petroleum Press, 2017.
- [43] Y. Hou, Z. Shi, and W. Mu, “Fluid geochemistry of fault zone hydrothermal system in the Yidun-Litang area, eastern Tibetan Plateau geothermal belt,” *Geofluids*, vol. 2018, Article ID 6872563, 13 pages, 2018.
- [44] X. Wang, G. Wang, H. Gan, Z. Liu, and D. Nan, “Hydrochemical characteristics and evolution of geothermal fluids in the Chabu high-temperature geothermal system, Southern Tibet,” *Geofluids*, vol. 2018, Article ID 8532840, 15 pages, 2018.
- [45] X. Wang and X. Zhou, “Geothermometry and circulation behavior of the hot springs in Yunlong county of Yunnan in Southwest China,” *Geofluids*, vol. 2019, Article ID 8432496, 16 pages, 2019.

Research Article

Relationship between Movement Laws of the Overlaying Strata and Time Space of the Mined-Out Volume

Xiang Yu,¹ Kang Zhao ,^{1,2} Qing Wang ,¹ Yajing Yan,¹ Yongjun Zhang,³ and Junqiang Wang²

¹School of Architectural and Surveying & Mapping Engineering, Jiangxi University of Science and Technology, Ganzhou 341000, China

²Lingbao Jinyuan Mining Company Limited, Lingbao 472500, China

³School of Civil Engineering, Qingdao Technological University, Qingdao 266033, China

Correspondence should be addressed to Kang Zhao; zhaok_666666@163.com and Qing Wang; wangqsvip@163.com

Received 6 August 2019; Revised 2 January 2020; Accepted 6 February 2020; Published 27 March 2020

Guest Editor: Glenda Taddia

Copyright © 2020 Xiang Yu et al. This is an open access article distributed under the Creative Commons Attribution License, which permits unrestricted use, distribution, and reproduction in any medium, provided the original work is properly cited.

The study and accurate prediction of the movement of overburden rock mass and surface subsidence are crucial for a safe production in metal mines. This study investigates the relationship between the movement laws of overlaying strata and the time space of a mined-out volume using Rock Failure Process Analysis (RFPA) System. Furthermore, the movement, deformation, and failure laws of overlaying strata are examined in different positions when a goaf volume is certain and the failure behavior of the overlaying strata. This study analyzes the similarities and differences of the overlaying strata comparatively. Results show that, regardless of the movement range or subsidence value of the overlying rock mass, a power function relationship is observed between them and working face advancement. Setting the equation shows that the scope of the overlying rock mass is significant when the ratio of a certain position distance roof to the working face distance is small. The results provide a reference for controlling the displacement of the overlying rock mass and treating goaf.

1. Introduction

The 3D stress balance of surrounding rock is destroyed by underground mining and tunnel excavation [1, 2], which can easily cause overburden movement, surface subsidence, and even collapse [3]. The collapse of a work-out area can seriously threaten a safe production and adversely affect the surface buildings and environment [4]. Currently, overlaying strata movement theory mainly includes “three zones,” key strata, plate, and masonry beam theories [5, 6]. The main methods include probability integral, numerical simulation, similar model, stochastic medium, and neural network prediction [7–9]. Many studies on the coal seam movement with a satisfied application are available [10, 11]. The mining subsidence mechanism of a metal mine with fractured blocky rock mass is different from a coal mine with a layered rock mass. The rock mass in a metal mine has a typical inhomogeneous and discontinuous self-stressed block-hierarchical structure because the morphology of ore body, geological

structure, and mining methods in metal mines differ from those in coal mines [12, 13]. The subsidence of overlaying strata in a metal mine is abrupt, and its subsidence, such as collapse pit and tubular or funnel collapse, is discontinuous. However, coal mine subsidence changes quite slowly [14, 15]. Thus, applying the movement theories of coal strata to metal mines is unsuitable. Consequently, investigating the overburden movement mechanism of metal mines is crucial.

At present, domestic and international scholars have created numerous theories and experience studies on overlaying strata movement from different angles and have gained certain achievements [16–20]. However, research on the time space of a mined-cavity volume based on the movement laws of overlaying strata is limited. On the basis of certain references [21], the stability of overlaying strata in metal mining has been analyzed systemically through a numerical simulation using rock mass failure process analysis software Rock Failure Process Analysis (RFPA) System [22, 23]. From the angle of quantitative analysis, the characteristics of the metal

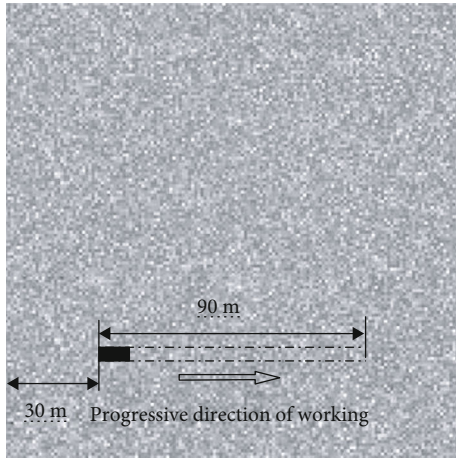


FIGURE 1: Calculation model.

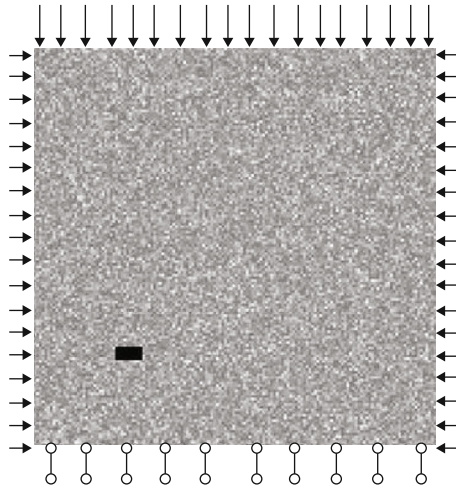


FIGURE 2: Mechanical model.

mine strata movement are investigated, and the formula between the overlying rock mass movement and the working face propulsion in different positions of goaves is obtained. This formula offers a new method for calculating the overlying rock mass movement.

2. Model Building and Parameter Setting

Based on a practical engineering [21], a gold metal mining has a background of a 500 m ore body depth, a dip near the horizontal, an ore body thickness near 5 m, and a 90 m ore body length. The region is mainly composed of silty clay and detritus. The overlying strata contain few crush zones. The occurrence is steady, and the structure is simple, that is, its roof comprises sandy clay and shale with few mudstones, and the bottom consists of sandy clay and shale. This study investigates the failure process of an overlying rock mass by using a plane strain model. The calculation model is located 150 m along the horizontal direction, 150 m in the vertical direction, has a 5 m ore body thickness, an ore body that is 35 m from the lower boundary, and 30 m far from the left and right boundaries. The model is illustrated

in Figures 1 and 2. The gravity stress function in the vertical direction and the model size are considered. Therefore, a 7 MPa stress must be applied to the vertical direction. According to the measured geostress data, a 2 MPa stress is applied to the horizontal direction combined with the geological features and tectonic stress in the mine. The model parameters are randomly assigned, in which an elasticity modulus is averaged, and other physical parameters are set in accordance with the mechanical properties of rocks to simulate the complexity of the geological occurrence conditions of metal mines accurately. The parameter is illustrated in Tables 1 and 2. Research on a dynamic damage rule of overlying rock mass under the condition of the ore mining process is conducted by using a step-by-step excavation model, and each step is 10 m.

3. Result Analysis of Overlying Strata Failure

A goaf roof generates microcracks and sporadic caving before the working face advances to 50 m. Evident microfissure, propagation, and partially sporadic collapses are observed on the roof when the working face advances to 50 m, which has a 5 m length and arch shape. The result is shown in Figures 3 and 4. The rupture continues to expand and cause periodic caving with the increase in the mined-out volume. After the end of mining, the overlying rock mass no longer collapses, and only sporadic caving appears above the roof. The appearance of cracks in the interior of the overburden rock does not continue its connection, thereby indicating the inexistence of a large collapse area inside the overburden rock, but the plastic zone continues to expand.

This section investigates the strata displacement and deformation in different positions through a quantitative analysis. We monitored different positions in the overlying strata (i.e., 5, 10, 20, 30, 50, and 80 m away from the roof) to investigate the displacement and deformation in the process of mining damage in different positions of the overlying rock mass. Given the proportion relationship between the ore body trend, mining length, and average mining depth, this study investigates the laws of overburden movement and failure of metal mines under the condition of nonfull mining.

Figure 5(a) illustrates the relationship among displacement changes with a 5 m distance from the roof in the overlying strata and working face advancement. The results showed that the range of the work-out area increases with the working face length. The subsidence range of rock mass, which has a 5 m distance from the roof, is gradually increased. The subsidence process of the overlying rock mass gradually changes before the working face advances to 40 m. The overlying rock mass displacement is small. Thus, a slight mutation has occurred, thus indicating that a small amount of rupture occurs in the rock material, and the change in the overlying rock displacement is limited given the change in the volume of the rock material molecule itself. Figure 5(a) also demonstrates that the maximum subsidence value is 2.17 mm, and the sinking range is 20 mm when the working face advances to 10 m. The maximum subsidence value is 12.03 mm, and the sinking range is approximately 20 mm when the working face advances to 30 m. All of these observations indicate that no major failure and coalescence

TABLE 1: Boundary condition and mining parameter.

Control condition	X direction stress	Simulation tectonic stress	2 MPa	Load type	Plane strain
	Y direction stress	Overlaying rock mass gravity	7 MPa	Strength criterion	Mohr-Coulomb criterion
Simulation mining	Ore body distance from upper boundary (m)	110	Working thickness (m)	5	
	Each step mining long (m)	10	Total mining step/step	9	

TABLE 2: Physical-mechanical parameters of the model.

Rock type	Elasticity modulus (MPa)	Uniaxial compressive strength (MPa)	Bulk density (kN/m ³)	Poisson ratio	Internal friction (°)
Sandy stone	10000	90	25	0.25	30
Shale	15000	100	28	0.24	35
Siltstone	5000	20	22	0.3	30
Mudstone	2000	10	20	0.3	25
Silty clay and detritus	1000	2	14	0.35	20

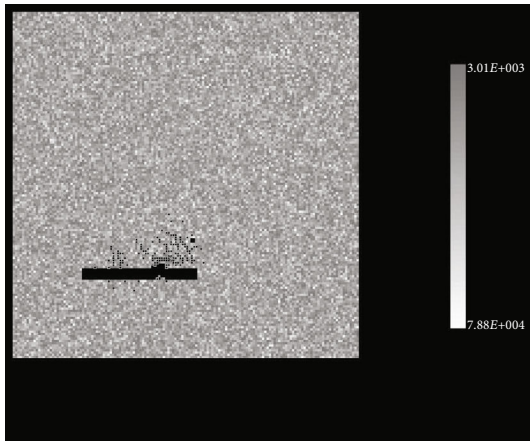


FIGURE 3: Breaking conditions in the roof.



FIGURE 4: Acoustic emission distribution.

occur in the overlying rock mass. When the working face advances to 40 and 50 m, the subsidence curve shows a mutation trend, especially when the working face advances to 50 m. A “sharp point” in the curve is observed, and the maximum subsidence reaches 34.32 mm. The result shows that the overburden rock material itself has numerous molecular damages. Furthermore, crack coalescence and interaction may induce mutation. The subsidence curve has been interrupted in the working face between 60 and 90 m, thereby indicating that the collapse occurs 5 m away from the roof. The subsidence range increases with the advancement in the working face. Overall, the large subsidence and abrupt change in the overburden are caused by fissures and coalescence inside the overlying rock mass.

Figure 5(b) depicts the relationship between displacement change with a 10 m distance from the roof in the overlying strata and the working face advancement. The range value of subsidence in the 5 m overlying distance from the roof increases with the advancement in the working face. When the working face advances to 50 m, the subsidence curve is gradual, thus implying that the overlying rock has not resulted in a hole-through crack, and the failure and movement of the rock material produce a large displacement. This phenomenon denotes that no collapse occurs in the overlying strata. The subsidence curve is interrupted when the working face advances from 60 m to 90 m, thereby signifying an occurrence of a collapse. However, the interval of interruptions is smaller than that demonstrated Figure 5(a). When the working face advances to 60 m, the caving length becomes 10 and 20 m with 10 and 5 m distance from the roof, correspondingly. When the working face advances to 90 m, the caving length becomes 11 and 22 mm with 10 and 5 mm distance from the roof, respectively. The strata subsidence is smaller at 10 m than at 5 m.

Figure 5(c) exhibits that the range and value of the overlying rock mass subsidence, which are 20 m away from the roof, increase with the advancement in the working face.

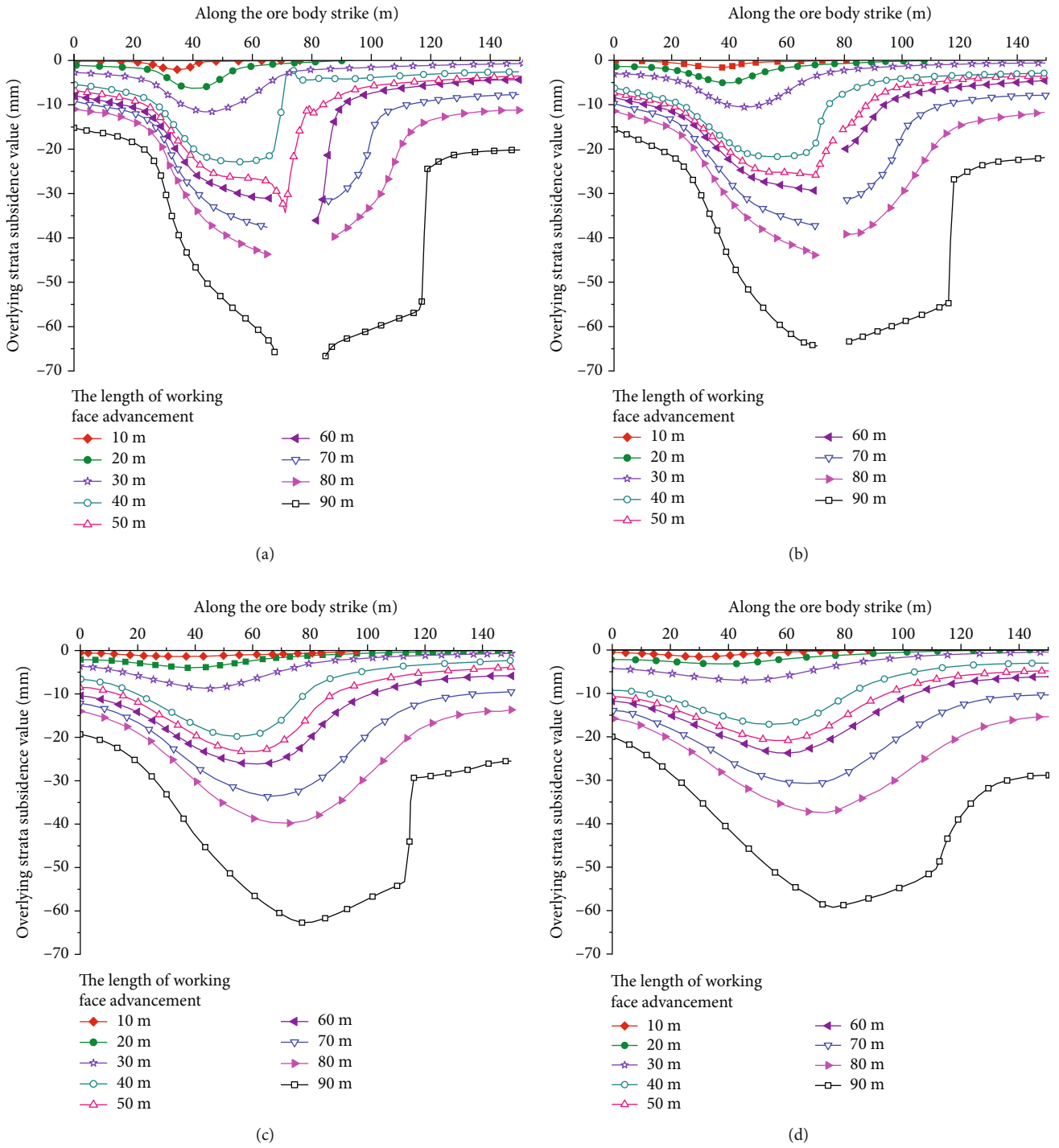


FIGURE 5: Continued.

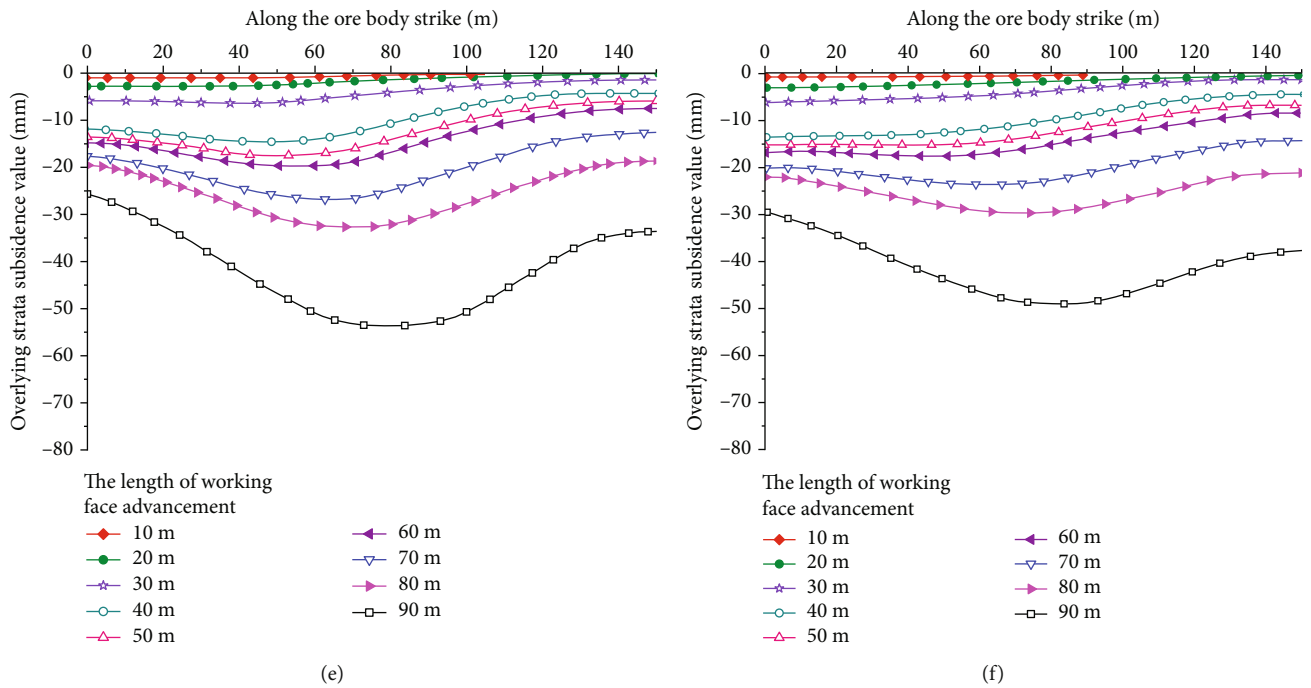


FIGURE 5: (a) Distance to roof 5 m. (b) Distance to roof 10 m. (c) Distance to roof 20 m. (d) Distance to roof 30 m. (e) Distance to roof 50 m. (f) Distance to roof 80 m.

Furthermore, the strata subsidence curve gradually changes. Thus, the internal material of the rock cover does not produce large fracture and caving before the working face advances to 80 m. The sinking curve is continuous until the working face advances to 90 m. Moreover, a polyline is produced, thereby indicating that the rock cover’s internal material fracture and the longevity of a small displacement are insufficient for fracture and caving. At this time, the maximum subsidence value reaches 62.82 mm, which is the tipping point of the caving area.

Figure 5(d) displays the relationship between the displacement change with a 30 m distance from the roof in the overlying strata and the working face advancement. The range and value of subsidence in the overlying strata with a 50 m distance from the roof gradually increase with the advancement in the working face. Although the subsidence curve, as a whole, is continuous, the curve is smoother than that with the 20 m distance from the roof. This finding shows the absence of microfissures in the overlying rock mass, but a few materials inside the damage still exist, thereby locally affecting its sinking displacement. The maximum sinking amount at this time is 58.83 mm.

Figure 5(e) presents the relationship between the displacement change with a 50 m distance from the roof in the overlying strata and the working face advancement. With the advancement in the working face, the range and value of subsidence with a 50 m distance from the roof in the overlying rock mass gradually increase. Figure 5(e) also illustrates that the subsidence curve of the overburden rock is smooth, thereby indicating no large fissure zone in the overlying rock at 50 m from the top of the roof from the beginning to the end of ore body mining. Moreover, the fracture is only found

inside the material, thereby denoting that the area belongs to the plastic zone. The acoustic emission and overburden rock burst figure in this region do not exhibit a large rupture, and an acoustic emission gathers nucleation. In the end, the ore body mining subsidence is 53.46 mm.

Figure 5(f) demonstrates that the subsidence curve is linear 80 m away from the roof before the working face advances to 80 m, thereby implying that this area is elastic. A minimal acoustic emission signal indicates the occurrence of a slight rupture inside the rock material. The subsidence curve has a downward bending trend, thus indicating that several material molecules have been destroyed at this time. The overlying strata can produce a small displacement and a maximum subsidence value of 48.71 mm, which denotes a plastic region.

The aforementioned diagrams depict the following laws of overburden failure and displacement through vertical and horizontal comparison.

Therefore, we can analyze and draw the following conclusions in a certain position in the overlying strata: the subsidence value and movement range of an overlying rock mass gradually increase with the advancement in the working face. The maximum subsidence vertex curve gradually moves toward the direction of the working face advancement.

Furthermore, we can analyze and draw the following conclusions when the working face advancement is certain: the subsidence value and movement range of an overlying rock mass decrease with the increase in the distance to the roof. The slope changes in the subsidence curve vertices reflect the rate of subsidence value change at a definite localization. The subsidence value and rate of change are large when the slope variation is also considerable. The

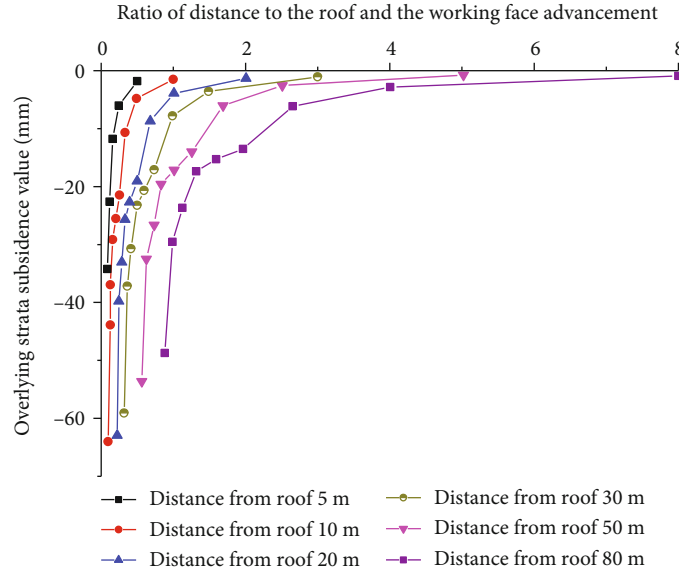


FIGURE 6: Relationship subsidence and ratio of distance to roof and working face advancement.

TABLE 3: Ratio of subsidence to working face advancement.

Distance from roof (m)	Coefficient a	Coefficient b	Correlation coefficient R^2
5	-0.52	-1.83	0.97
10	-1.94	-1.56	
20	-4.24	-1.72	
30	-7.19	-1.82	
50	-14.86	-2.03	
80	-34.57	-1.98	
Average value	-10.55	-1.82	

interruption in the curve reflects the occurrence of collapse in this area. The horizontal distance of the interruption indicates the size of the caving area. Under the condition of the same working face length, a high horizontal distance of the interruption indicates that the gob roof is near, and the collapse area is large.

4. Function Building and Discussion

Figure 6 exhibits the ratio relation between the subsidence value in the different positions in the overlying strata and the working face length to investigate the relationship between the subsidence and the movement range in different overlying rock mass positions. In accordance with the fitted curves under different conditions, the models of the working face distance and subsidence in the various positions of the overlying strata are established. The power function relationship between different position subsidence and overlying strata is evident. Power function can be expressed as $y = ax^b$. The parameters are shown in Table 3.

Thus, the final curve equation can be represented as $y = 10.55x^{1.82}$.

A small ratio of the position distance from the roof to the overlying strata and the working face advancement indicates a large subsidence by analyzing the curves and equations in Figure 7. When the ratio tends to 0, the subsidence tends to infinity. This result is consistent with the actual monitoring data. A collapse does not produce data, and the final subsidence amount cannot be monitored. A large ratio of the distance from a certain position to the gob roof and the working face advancement implies a considerable distance from the roof or a small mined-out volume and a small subsidence in the overlying strata. The overburden strata do not move when the position arrives at infinity or is not a goaf.

Figures 8 and 9 display the relationship between the overlying strata movement range and the working face advancement. This relationship is similar to the laws of strata subsidence. A power function relationship between these factors is observed through data analysis. The equation can be expressed as $y = ax^b$. The parameters are shown in Table 4.

Thus, the final curve equation can be represented as $y = 28.19x^{1.14}$.

The results show that, when the ratio of the position distance roof to the working face is small, the scope of the strata movement is extensive. In particular, the overlying rock mass that is close to the roof or the relatively large gob volume can considerably influence the strata movement. The scope of the strata movement is small when the ratio of the distance to the roof and the working face is large. When infinity or no goaf is reached, the overlying rock does not move.

5. Conclusion

In a certain position in the overburden, the subsidence value and movement range of overburden rock gradually increase with the advancement in a working face (the volume of goaf increases gradually). The maximum subsidence vertices of a

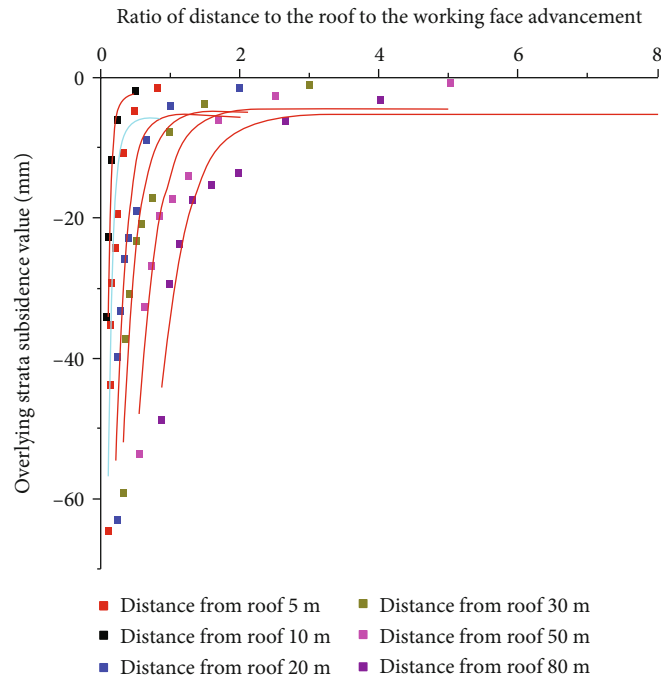


FIGURE 7: Fitting relationship subsidence and ratio of distance to roof and working face advancement.

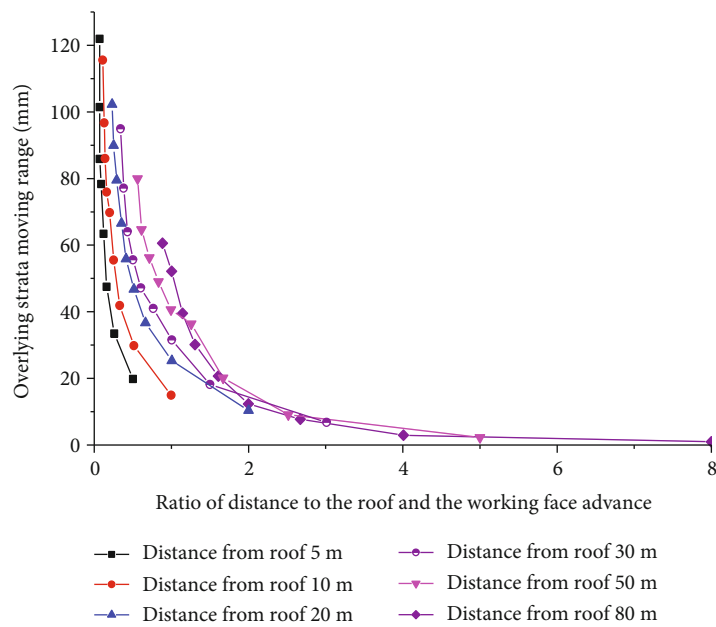


FIGURE 8: Relationship movement range and ratio of distance to roof and working face advancement.

curve gradually move toward the direction of the working face advancement.

- (1) When the working face advancement is certain, the movement range and subsidence value have decreased with the increase in the monitoring of the distance to the roof. The subsidence curve breakpoints reflect a collapse in this area. The horizontal distance of the interruption indicates the size of the caving area. Under the condition of the same working face length,

a high horizontal distance of the interruption that denotes a close roof indicates a large collapse area

- (2) Regardless of the subsidence or movement range of the overlying strata, all of subsidence or movement range and working face advancement perform the power function relationship ($y = ax^b$). The overlying strata subsidence and working face advancement satisfy the power function relationship as follows: $y = 10.55x^{1.82}$. The overlying strata movement range

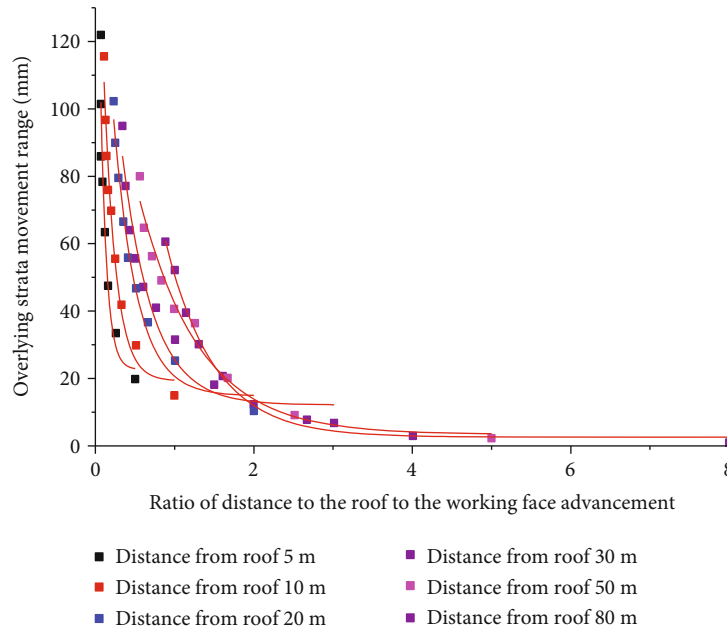


FIGURE 9: Fitting relationship movement range and ratio of distance to roof and working face advancement.

TABLE 4: Ratio of movement range to working face advancement.

Distance from roof (m)	Coefficient a	Coefficient b	Correlation coefficient R^2
5	10.28	-0.88	0.99
10	16.11	-0.88	
20	24.29	-0.95	
30	28.60	-1.05	
50	39.77	-1.16	
80	50.07	-1.9	
Average value	28.19	-1.14	

and working face advancement satisfy the power function relationship as follows: $y = 28.19x^{1.14}$

- (3) The scope of the strata movement is extensive when the ratio of the position distance to the roof and the working face advancement is small. When the ratio of the position distance to the roof and the working face is large, the strata movement demonstrates a small scope. The overburden strata do not move when infinity or no gob is reached

Data Availability

The test data used to support the findings of this study are included within the article. Readers can obtain data supporting the research results from the test data table in the paper.

Conflicts of Interest

No conflict of interest exists in the submission of this manuscript, and manuscript is approved by all authors for publica-

tion. I would like to declare on behalf of my co-authors that the work described was original research that has not been published previously, and not under consideration for publication elsewhere, in whole or in part. All the authors listed have approved the manuscript that is enclosed.

Acknowledgments

The study has been supported by the National Natural Science Foundation (No. 51764013), by the Science and Technology Support Plan Project of Jiangxi Provincial Science and Technology Department (Grant No. 20161BBG70075, 20143ACG70010), by the Key Research Project of Science and Technology of Jiangxi Provincial Education Department (Grant No. GJJ160592), and by the Undergraduate Innovation and Entrepreneurship Training Program (Grant No. XS2018-S012). Sincere thanks are given to Dr. Shuai Cao for his technical guidance on this manuscript.

References

- [1] W. A. Griffith, J. Becker, K. Cione, T. Miller, and E. Pan, "3D topographic stress perturbations and implications for ground control in underground coal mines," *International Journal of Rock Mechanics and Mining Sciences*, vol. 70, pp. 59–68, 2014.
- [2] P. Wang, L. S. Jiang, P. Q. Zheng, G. P. Qin, and C. Zhang, "Inducing mode analysis of rock burst in fault-affected zone with a hard-thick stratum occurrence," *Environmental Earth Sciences*, vol. 78, no. 15, p. 467, 2019.
- [3] S. J. Schatzel, C. Ö. Karacan, H. Dougherty, and G. V. R. Goodman, "An analysis of reservoir conditions and responses in longwall panel overburden during mining and its effect on gob gas well performance," *Engineering Geology*, vol. 127, pp. 65–74, 2012.

- [4] E. F. Salmi, M. Nazem, and M. Karakus, "Numerical analysis of a large landslide induced by coal mining subsidence," *Engineering Geology*, vol. 217, pp. 141–152, 2017.
- [5] L. Jiang, P. Wang, P. Zheng, H. Luan, and C. Zhang, "Influence of Different Advancing Directions on Mining Effect Caused by a Fault," *Advances in Civil Engineering*, vol. 2019, Article ID 7306850, 10 pages, 2019.
- [6] J. Cheng, G. Zhao, and S. Li, "Predicting underground strata movements model with considering key strata effects," *Geotechnical and Geological Engineering*, vol. 36, no. 1, pp. 621–640, 2018.
- [7] T. N. Do, J. H. Wu, and H. M. Lin, "Investigation of sloped surface subsidence during inclined seam extraction in a jointed rock mass using discontinuous deformation analysis," *International Journal of Geomechanics*, vol. 17, no. 8, article 04017021, 2017.
- [8] Z. Yang, Z. C. Zhu, and H. J. Mi, "Numerical simulation research of wall rock stability of multi-stage excavated workings at Chengchao iron mine," *Journal of Jiangxi University of Science and Technology*, vol. 34, pp. 34–40, 2013.
- [9] B. Ghabraie, G. Ren, J. Smith, and L. Holden, "Application of 3D laser scanner, optical transducers and digital image processing techniques in physical modelling of mining-related strata movement," *International Journal of Rock Mechanics and Mining Sciences*, vol. 80, pp. 219–230, 2015.
- [10] R. Singh, P. K. Mandal, A. K. Singh, R. Kumar, J. Maiti, and A. K. Ghosh, "Upshot of strata movement during underground mining of a thick coal seam below hilly terrain," *International Journal of Rock Mechanics and Mining Sciences*, vol. 45, no. 1, pp. 29–46, 2008.
- [11] B. Unver and N. E. Yasitli, "Modelling of strata movement with a special reference to caving mechanism in thick seam coal mining," *International Journal of Coal Geology*, vol. 66, no. 4, pp. 227–252, 2006.
- [12] J. Rošer, D. Potočnik, and M. Vulić, "Analysis of dynamic surface subsidence at the underground coal mining site in Velenje, Slovenia through modified sigmoidal function," *Minerals*, vol. 8, no. 2, p. 74, 2018.
- [13] N. L. Grigorenko, D. V. Kamzolkin, and D. G. Pivovarchuk, "Optimization of open-pit mining by the gradient method," *Computational Mathematics and Modeling*, vol. 27, no. 3, pp. 351–359, 2016.
- [14] G. Ren, B. N. Whittaker, and D. J. Reddish, "Mining subsidence and displacement prediction using influence function methods for steep seams," *Mining Science and Technology*, vol. 8, no. 3, pp. 235–251, 1989.
- [15] A. Jaiswal and B. K. Shrivastva, "Stability analysis of the proposed hybrid method of partial extraction for underground coal mining," *International Journal of Rock Mechanics and Mining Sciences*, vol. 52, pp. 103–111, 2012.
- [16] K. Zhao, Q. Li, Y. Yan, K. Zhou, S. Gu, and S. Zhu, "Numerical Calculation Analysis of the Structural Stability of Cemented Fill under Different Cement-Sand Ratios and Concentration Conditions," *Advances in Civil Engineering*, vol. 2018, Article ID 1260787, 9 pages, 2018.
- [17] A. M. Suchowerska, R. S. Merifield, J. P. Carter, and J. Clausen, "Prediction of underground cavity roof collapse using the Hoek-Brown failure criterion," *Computers and Geotechnics*, vol. 44, pp. 93–103, 2012.
- [18] K. Zhao, K. Zhao, and L. Shi, "Collapsing height prediction of overburden rock mass at metal mine based on dimensional analysis," *Rock and Soil Mechanics*, vol. 36, pp. 2012–2026, 2015.
- [19] K. W. Mills, O. Garratt, B. G. Blacka, L. C. Daigle, A. C. Rippon, and R. J. Walker, "Measurement of shear movements in the overburden strata ahead of longwall mining," *International Journal of Mining Science and Technology*, vol. 26, no. 1, pp. 97–102, 2016.
- [20] K. Zhao, Q. Wang, S. Gu et al., "Mining scheme optimization and stope structural mechanic characteristics for a deep and large ore body," *JOM*, vol. 71, no. 11, pp. 4180–4190, 2019.
- [21] K. Zhao, Z. Guo, and Y. Zhang, "Dynamic simulation research of overburden strata failure characteristics and stress dependence of metal mine," *Journal of Disaster Research*, vol. 10, no. 2, pp. 231–237, 2015.
- [22] C. A. Tang and T. Xu, "Rock failure process analysis method (RFPA) for modeling coal strata movement," *Advances in Coal Mine Ground Control*, pp. 345–377, 2017.
- [23] C. A. Tang, H. Liu, P. K. K. Lee, Y. Tsui, and L. G. Tham, "Numerical studies of the influence of microstructure on rock failure in uniaxial compression – Part I: effect of heterogeneity," *International Journal of Rock Mechanics and Mining Sciences*, vol. 37, no. 4, pp. 555–569, 2000.

Research Article

Hydraulic Fracturing Behavior in Shale with Water and Supercritical CO₂ under Triaxial Compression

Jianming He ^{1,2,3}, Yixiang Zhang ^{1,2,3}, Chao Yin,^{1,2,3} and Xiao Li^{1,2,3}

¹Key Laboratory of Shale Gas and Geoengineering, Institute of Geology and Geophysics, Chinese Academy of Sciences, Beijing 100029, China

²Innovation Academy for Earth Science, Chinese Academy of Sciences, Beijing 100029, China

³University of Chinese Academy of Sciences, Beijing 100049, China

Correspondence should be addressed to Jianming He; hjm@mail.iggcas.ac.cn and Yixiang Zhang; zhangyixiang@mail.iggcas.ac.cn

Received 6 August 2019; Revised 24 December 2019; Accepted 21 January 2020; Published 18 March 2020

Guest Editor: Paolo Dabove

Copyright © 2020 Jianming He et al. This is an open access article distributed under the Creative Commons Attribution License, which permits unrestricted use, distribution, and reproduction in any medium, provided the original work is properly cited.

Comparing to the water fracturing fluid regularly used in the hydraulic fracturing operation, supercritical CO₂ (SC-CO₂) as a promising nonaqueous fracturing fluid has the great potential for the improvement of production and protection of shale reservoir. This paper presents an experimental study of the mechanical response and fracture propagation of shale fractured using water and SC-CO₂ under the different stress status and injection rate. According to the experimental results, SC-CO₂ fracturing is more time-consuming due to its compressibility which takes about 20 times more time than hydraulic fracturing using water under the same preset conditions. The breakdown pressure of shale can be affected by not only the anisotropy of itself but also the external factors like injection rate and deviator stress. Similar tendency of the breakdown pressure with the variation of bedding orientation can be observed in both of the fracturing using water and SC-CO₂. However, all of the shale specimens fractured using SC-CO₂ show smaller breakdown pressure if compared with the shale specimens fractured using water. According to the results of fracture width evolution monitored by circumference during the fracturing, the fracture propping and proper size of the proppant are really important for the hydraulic fracturing.

1. Introduction

Shale is composed of fine debris, clay, and organic matter (the diameter is less than 0.0039 mm) with extremely low permeability of about $10e^{-3} - 10e^{-6}$ mD [1, 2]. Hydraulic fracturing is a major technology used for the commercial development of shale gas which can significantly enhance the permeability and improve the production capacity because of large surface contact area formed between the fractures and reservoir [3–5].

Currently, water is the only fracturing fluid regularly used in the commercial shale gas development due to its low cost, availability, and its suitability for fracturing [6]. However, plenty of problems or concerns are brought by the fracturing fluid of water such as water shortages [7] and pollution of the flow-back water [8]. More importantly, shale will expand and induce a considerable strength reduction due to rich clay minerals in the presence of water [9, 10]. Consequently, it

is necessary to reduce or even eliminate water requirements in hydraulic fracturing which stimulates the exploration into the use of nonaqueous fracturing fluids. Supercritical CO₂ is a notable nonaqueous fracturing fluid currently under consideration due to its particular characteristics. When temperature and pressure, respectively, exceed 31.10°C and 7.38 MPa, CO₂ is in the supercritical state. It has traits of small intermolecular forces, zero surface tension, and strong mobility. Supercritical CO₂ offers several significant advantages over water, including the water-sensitive mineral protection [10, 11], high penetration rate in the shale formation and effective gas transportation from fractures with poor connectivity [12, 13], enhanced desorption of methane (CH₄) from organics present in shale, and fast and complete flow back [14–17]. In addition, large volumes of CO₂ used for shale gas production can be stored in the deep formation which is a major option to solve the issue of greenhouse gas emission as well [18].

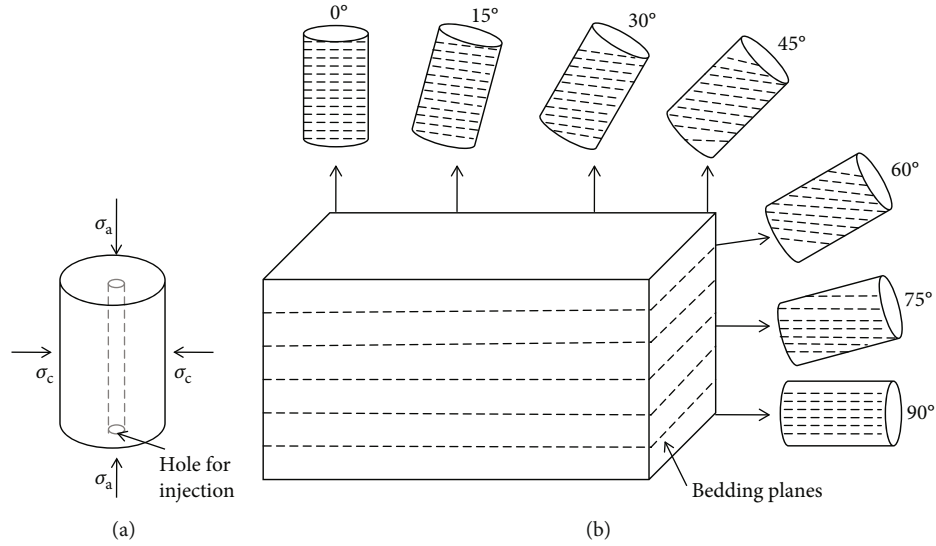


FIGURE 1: Diagram of (a) sample with injection hole and (b) sample with different bedding orientations.

Some researchers have compared the experimental results of hydraulic fracturing using water and SC- CO_2 , especially the influence of fracturing fluid viscosity. Ishida et al. [19, 20] found that CO_2 with low viscosity tends to generate cracks extending more three-dimensionally with a larger fractal dimension. Inui et al. [21] found that low-viscosity fluid, such as SC- CO_2 , could induce shear dominant fracture, while high-viscosity fluid could induce tensile dominant fracture. Chen et al. [22] observed the induced fractures of granite induced by SC- CO_2 , water, and viscous oil. The results showed that the most branches were induced by SC- CO_2 than the other fracturing fluids. Zhou et al. [23] used numerical simulations to investigate the influence of fluid viscosity and compressibility to the fracturing. The results indicated that thin fluid, such as CO_2 , would induce thinner and shorter fractures than water. Previous studies indicated that the natural fractures will affect the propagation of hydraulic fractures. The studies by Fan and Zhang [24] and Cheng et al. [25] indicated that both geological and engineering parameters determine whether hydraulic fractures cross the natural fractures. Zhang et al. [26] analyzed the different fracture geometry features induced by water and SC/L- CO_2 on cubic shale specimens. Zhou et al. [27] indicated that the expansion and thermal stresses due to SC- CO_2 phase change can extend the fractures.

Shale is a type of anisotropic rock with the well-developed sedimentary structures, especially the bedding planes with different orientation in the reservoir [28–31]. It is critical to study the mechanical response and fracture propagation of shale in hydraulic fracturing using water and SC- CO_2 considering its anisotropy. In this study, hydraulic fracturing experiments under triaxial compression were carried out using water and SC- CO_2 on shale specimens with varied bedding plane angles to study the characteristics of fracturing process. The shale specimens with different bedding plane angles were obtained from the same shale formation, and the borehole was drilled out along the central axis of the specimens. The effects of stress status and injection

rate on the mechanical response of shale during the hydraulic fracturing were discussed while the fracturing characteristics using water and SC- CO_2 were compared.

2. Experimental Methodology

2.1. Sample Preparation. Longmaxi shale formation of the Sichuan Basin in southern China was identified as one of the areas with the greatest potential in shale gas development [2]. The rock samples used for this laboratory experiment were taken from the outcrops of Silurian Longmaxi shale formation in Chongqing, China. The shale samples contain deep black carbonaceous shale with partly visible pyrite and calcite minerals. Cubic shale blocks with a size of 300 mm \times 300 mm \times 300 mm were obtained from the field, and then, the shale cores were drilled from the blocks in order to minimize the weathering during the transportation process as much as possible. The cylindrical specimen with a dimension of 100 mm in height and 50 mm in diameter was used in experiment. Both end sides of the cylindrical specimen were cut to flat and paralleled to each other. It was easy to determine the intersection angles between the drilling direction and the bedding plane, as the sedimentary planes were clearly visible on the surface of the blocks. The bedding plane angles were varied from 0° to 90° at the interval of 15° (0°, 15°, 30°, 45°, 60°, 75°, and 90°) as shown in Figure 1(b). A borehole with 8 mm in diameter and 100 mm in length was drilled at the central position along the coring direction for the injection of the fracturing fluid as shown in Figure 1(a). The drilled samples without obvious visible cracks on the surface were used to perform the fracturing experiment in this study.

2.2. Experimental System. All of the experiments of hydraulic fracturing in this paper were completed on the triaxial rock testing system accompanied with the injection system of fracturing fluid. The triaxial loading system allows for the triaxial loading of rock specimens along with the

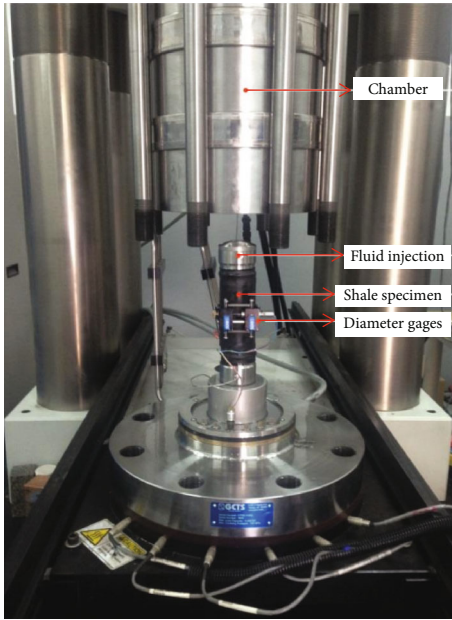


FIGURE 2: Shale specimen installed in the triaxial compression chamber.

simultaneous injection of fracturing fluid. Figure 2 shows the shale specimen installed in the triaxial compression chamber. Two metal blocks were glued on the shale specimens by epoxy to separate the fracturing fluid from the hydraulic oil for confining pressure. One of the metal blocks had the channel for fracturing fluid entering into the borehole. In addition, the circumferential extensometer was applied around the specimen to measure the radial strain in the process of experiment. Figure 3 shows the schematic diagram of the SC-CO₂ fracturing system. Compared with the room temperature of hydraulic fracturing using water, liquid CO₂ discharged from the cylinder was heated and controlled at 45°C after pressurization by ISCO pump to guarantee the super critical state of CO₂. A detailed discussion about SC-CO₂ fracturing system was reported by Zhang et al. (2019).

2.3. Testing Procedures. The injection rate of the fracturing fluid in the fracturing experiment was set as 0.2 or 0.3 ml/s. The confining pressure was set as 20 MPa, and the axial stress was set as 25, 30, and 35 MPa, respectively, to achieve the different deviator stresses. Step 1 was to set the stress state of the shale specimen to the target value. The rate of the confining pressure was 0.1 MPa/s while the increasing rate of axial stress was 0.2 MPa/s to achieve the target value. Thereafter, the stress status was servo controlled during the whole process of hydraulic fracturing. The next step was injecting the fracturing fluid at a preset rate into the specimen through the drilling hole. Finally, to reach an equilibrium state in the experimental system, the constant injection would last 1 more minute after the specimen fractured. The data of the axial stress, confining pressure, radial deformation, and pump pressure were recorded during the process of fracturing experiment.

To understand the effects of different fracturing fluid on the shale, the specimens were grouped into two sets for hydraulic fracturing using water and SC-CO₂, respectively. Seven different bedding plane angles (0°, 15°, 30°, 45°, 60°, 75°, and 90°) of the shale were considered in each set of specimens.

3. Results and Discussion

Experiment results can be used for understanding the fracturing process and its mechanism, especially the difference between the water fracturing and SC-CO₂ fracturing. Table 1 shows the preset conditions and breakdown pressure (peak value of pump pressure) of the different shale specimens with varied bedding plane angles. In this section, the pump pressure development and breakdown pressure variation of sample with different bedding directions are shown. The influence of deviator stress on the shale breakdown pressure is analyzed. In addition, shale fracture propagation and development of the fracture width are discussed.

3.1. Evolution of the Pump Pressure. The constant injection rate (0.3 ml/s) of water and SC-CO₂ was applied into the borehole for the fracturing of specimen under the preset triaxial stress conditions (axial stress $\sigma_a = 25$ MPa, confining pressure $\sigma_c = 20$ MPa). Figure 4 shows some typical pump pressure development for specimens with different bedding plane angles (0°, 30°, 60°, and 90°). The pump pressure increases with the injection of fracturing fluid until it peaks at the breakdown pressure, and the specimen fracturing occurs instantaneously. After that, the pump pressure dropped to a value equivalent to the confining pressure in general, which can be attributed to the connection between the fracturing fluid and confining oil in the compression chamber. It indicated that the equilibrium state between the pump pressure and confining pressure had been reached in the triaxial rock testing system.

The pressure curves of SC-CO₂ fracturing (Figure 4) show that the initial pressure is approximate 6 MPa when the liquid CO₂ is injected into the borehole. With the constant injection of the SC-CO₂, the pump pressures increase with a relatively low increase rate due to the volume compressibility of CO₂. The increase rate of CO₂ pressure increases gradually even the injection rate keeps constant, and its amplitude increased obviously before peaking at the breakdown pressure. Compared with the SC-CO₂ fracturing, the pump pressure of water fracturing only shows a little increase during the initial pressurization stage and it increases sharply at a much higher rate before the peak value breached. Therefore, hydraulic fracturing using SC-CO₂ is more time-consuming than the fracturing using water under the same experimental conditions. Table 2 shows the comparison of exact time taken for pump pressure development of fracturing using water and SC-CO₂. In general, SC-CO₂ fracturing takes about 20 times more time than water fracturing under the same experimental conditions.

3.2. Variation of the Breakdown Pressure. Shale reveals strong anisotropy in the failure strength under triaxial compression

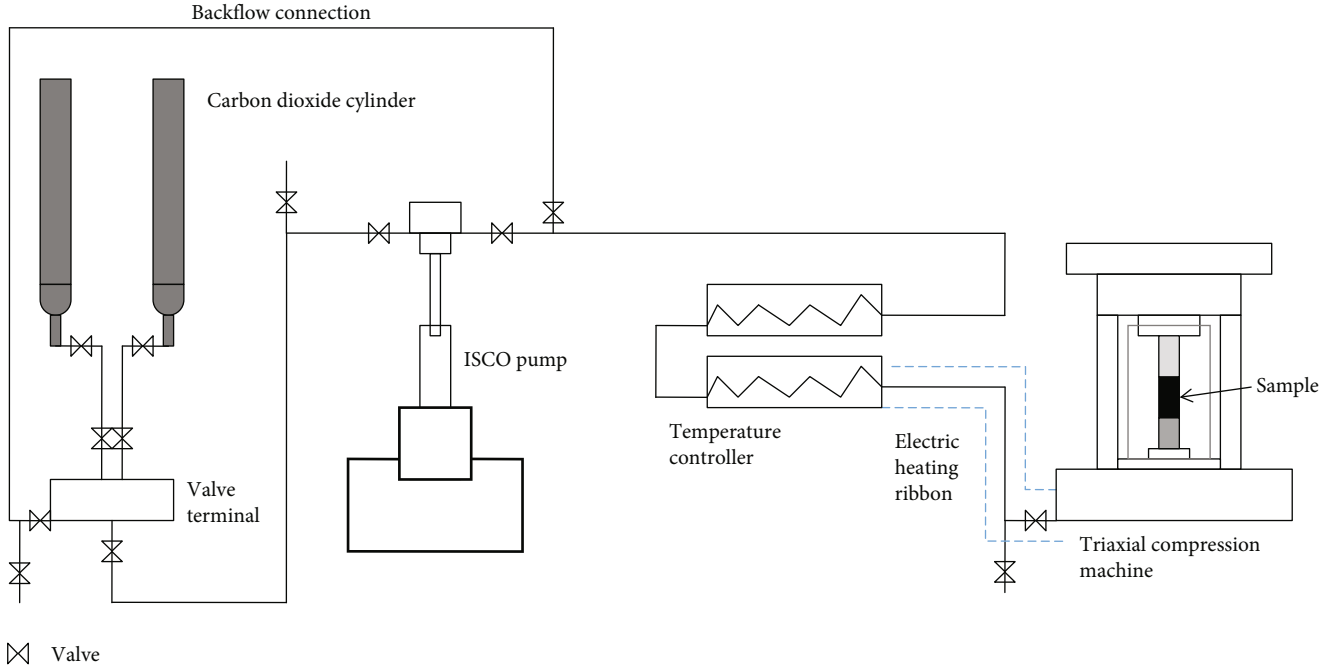


FIGURE 3: Schematic of SC-CO₂ fracturing system.

and Brazilian test conditions [32–34], as does in the breakdown pressure of hydraulic fracturing. The variations of breakdown pressure in hydraulic fracturing using water and SC-CO₂ versus bedding plane angle are shown in Figure 5, respectively. Breakdown pressure of the specimen with the bedding plane angle of 0° shows the highest value, and the specimen with the bedding plane angle of 90° shows the minimum value under the same experimental conditions, regardless of the fracturing fluid being water or SC-CO₂. The values of breakdown pressure of the rest of the specimens with different bedding plane angles (15°, 30°, 45°, 60°, and 75°) occur to fluctuate in a certain range depending on the failure pattern. When the sample is fractured along the bedding plane, it shows the relatively low breakdown pressure. In contrast, the samples have high breakdown pressures with failure patterns across the bedding plane. It also indicates that the breakdown pressure of the shale increases generally with the increase of injection rate of the fracturing fluid if the results of breakdown pressure in Figures 5(a) and 5(b) are compared.

The specimen fractured using SC-CO₂ shows the smaller breakdown pressure if compared with the corresponding specimen fractured using water. Table 3 shows the breakdown pressure variation of the specimens with bedding plane angle of 0° and 90° under the injection rate of 0.2 ml/s and 0.3 ml/s, respectively. The reduction proportion of breakdown pressure using water is higher than the reduction proportion of breakdown pressure using SC-CO₂ regardless of the injection rate. Therefore, the anisotropy in breakdown pressure of shale under SC-CO₂ fracturing is weaker than that under water fracturing. Furthermore, the higher injection rate of 0.3 ml/s can induce a bigger gap (from 27.06% to 39.68%) between the breakdown pressures of the fractur-

ing using water and SC-CO₂ if compared with the lower injection rate of 0.2 ml/s (from 23.25% to 28.26%).

3.3. Effects of Deviator Stress on the Breakdown Pressure. The shale reservoir has a large depth which causes the in situ stress state to be close to the hydrostatic state, which can attribute to an insignificant deviator stress in the reservoir (Lin et al., 2018). In order to study the effects of this deviator stress on the fracturing, the confining stress of the specimens was set as 20 MPa and the axial stress was set as 25, 30, and 35 MPa, respectively. The injection rate was kept constant as 0.3 ml/s in the experiment for the comparison. The experimental results of the specimens with bedding plane angle of 0° and 90° fractured using water and SC-CO₂ under different deviator stress are shown in Figure 6.

The relationships between the deviator stress and breakdown pressure of the fracturing are shown in Figure 6. It indicates that the breakdown pressure decreases with the increase of deviator stress in the fracturing using water or SC-CO₂. It is consistent with the elasticity theory to calculate the breakdown pressure as follows [35, 36]:

$$P_b = 3\sigma_{\min} - \sigma_{\max} + \sigma_T, \quad (1)$$

where σ_{\min} , σ_{\max} represent the minimum and the maximum value in situ stress, respectively, and σ_T represents the tensile failure stress of the rock. Equation (1) shows that stress condition and tensile strength influence the breakdown pressure of rock regardless of the fracturing fluid and the higher deviator stress ($\sigma_{\max} - \sigma_{\min}$) can result in a lower breakdown pressure value. The specific values of the relationship are shown in Table 4. It indicates that the breakdown pressure of shale decreases by around 20% as the deviator stress

TABLE 1: Summary of the fracturing experiments results.

No.	Bedding plane angle	Fracturing fluid	σ_a (MPa)	σ_c (MPa)	q (ml/s)	P_b (MPa)
W1	0°	Water	25	20	0.3	70.37
W2	15°	Water	25	20	0.3	59.78
W3	30°	Water	25	20	0.3	51.77
W4	45°	Water	25	20	0.3	53.09
W5	60°	Water	25	20	0.3	59.52
W6	75°	Water	25	20	0.3	50.13
W7	90°	Water	25	20	0.3	42.45
W8	0°	Water	30	20	0.3	61.89
W9	0°	Water	35	20	0.3	57.02
W10	90°	Water	30	20	0.3	38.91
W11	90°	Water	35	20	0.3	34.53
W12	0°	Water	25	20	0.2	54.56
W13	15°	Water	25	20	0.2	44.21
W14	30°	Water	25	20	0.2	42.29
W15	45°	Water	25	20	0.2	49.86
W16	60°	Water	25	20	0.2	46.82
W17	75°	Water	25	20	0.2	43.02
W18	90°	Water	25	20	0.2	39.14
S1	0°	SC-CO ₂	25	20	0.3	52.15
S2	15°	SC-CO ₂	25	20	0.3	41.81
S3	30°	SC-CO ₂	25	20	0.3	42.91
S4	45°	SC-CO ₂	25	20	0.3	39.94
S5	60°	SC-CO ₂	25	20	0.3	44.46
S6	75°	SC-CO ₂	25	20	0.3	45.75
S7	90°	SC-CO ₂	25	20	0.3	38.04
S8	0°	SC-CO ₂	30	20	0.3	43.20
S9	0°	SC-CO ₂	35	20	0.3	41.31
S10	90°	SC-CO ₂	30	20	0.3	30.08
S11	90°	SC-CO ₂	35	20	0.3	28.88
S12	0°	SC-CO ₂	25	20	0.2	40.51
S13	15°	SC-CO ₂	25	20	0.2	36.38
S14	30°	SC-CO ₂	25	20	0.2	34.42
S15	45°	SC-CO ₂	25	20	0.2	35.89
S16	60°	SC-CO ₂	25	20	0.2	32.31
S17	75°	SC-CO ₂	25	20	0.2	34.49
S18	90°	SC-CO ₂	25	20	0.2	31.09

Note: σ_a denotes axial stress; σ_c denotes confining pressure; q denotes injection rate; P_b denotes breakdown pressure which is the pressure value of fracturing fluid when the specimen is fractured.

increased from 5 MPa to 15 MPa. In addition, the reduction proportion of the breakdown pressure in SC-CO₂ fracturing is slightly higher than that of hydraulic fracturing using water.

3.4. Fracture Propagation. The fracture always propagates along mechanically favorable direction in the process of hydraulic fracturing. When the fracture encounters the pre-existing plane of weakness in shale, the fracture propagation would be complicated and different patterns of the fracture

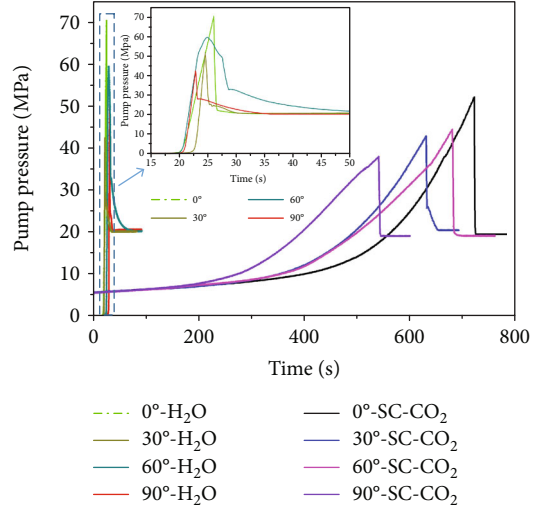


FIGURE 4: Typical pump pressure curves of shale fractured using water and SC-CO₂.

TABLE 2: Time comparison of pump pressure to peak using water and SC-CO₂.

No.	Bedding plane angle	Fracturing fluid	Injection rate (ml/s)	Time (s)	Time ratio (t_s/t_w)
W1	0°	Water	0.3	26	27.73
S1	0°	SC-CO ₂		721	
W3	30°	Water		25	25.20
S3	30°	SC-CO ₂		630	
W5	60°	Water	25	27.16	
S5	60°	SC-CO ₂	679		
W7	90°	Water	23	23.48	
S7	90°	SC-CO ₂	540		

t_s denotes the time of SC-CO₂ pump pressure reaching peak. t_w denotes the time of water pump pressure reaching peak.

propagation could be observed depending on the fracturing fluid, preexisting planes, and in situ stress state ([37]; Lin et al., 2017).

Previous experimental study on the hydraulic fractures demonstrated that simple and symmetrical fractures were generated around the injection hole in relatively homogeneous rocks [38]. In this study, the anisotropy of the shale caused by the variation of bedding orientation could make the propagation pattern of hydraulic fracture more complex. Figure 7 shows the morphology of main fractures formed in shale specimens after the fracturing experiment, in which different patterns of fracture propagation with complex morphology can be observed. Three typical propagation patterns can be found according to the relative orientation of hydraulic fracture with respect to the bedding plane, which include propagating across, propagating along, and being arrested.

As the case of water fracturing shown in Figure 7(a), the fracture just propagate along the bedding plane in the specimen with bedding plane angle of 45° and 90°. The fractures of

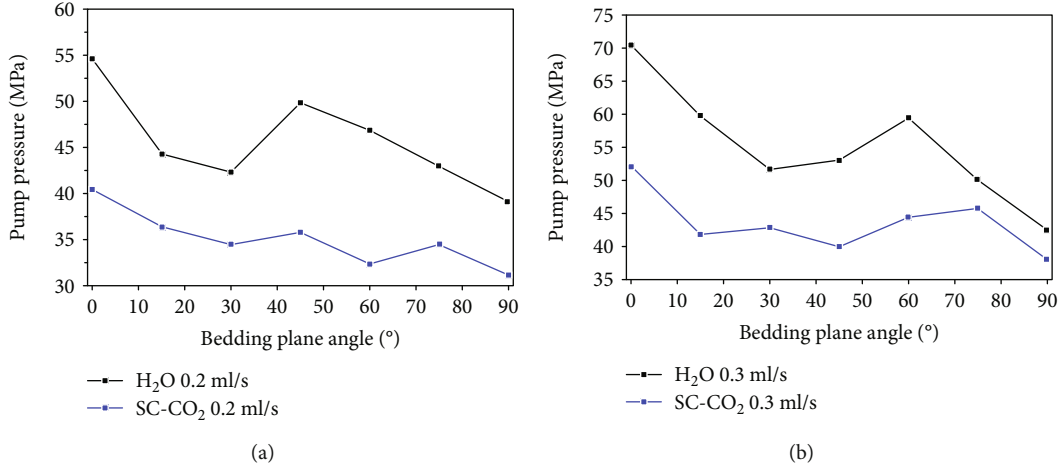


FIGURE 5: Variation of the breakdown pressure of fracturing using water and SC-CO₂ with the injection rate of (a) 0.2 ml/s and (b) 0.3 ml/s.

TABLE 3: Comparison of shale breakdown pressure variation.

No.	Bedding plane angle	Fracturing fluid	Injection rate (ml/s)	Breakdown pressure (MPa)	Reduction proportion (((P ₀ - P ₉₀)/P ₀) × 100%)
W12	0°	Water	0.2	54.56	28%
W18	90°			39.14	
S12	0°	SC-CO ₂		40.51	23%
S18	90°			31.09	
W1	0°	Water	0.3	70.37	40%
W7	90°			42.45	
S1	0°	SC-CO ₂		52.15	27%
S7	90°			38.04	

P₀ denotes the breakdown pressure of shale with a bedding plane angle of 0°. P₉₀ denotes the breakdown pressure of shale with a bedding plane angle of 90°.

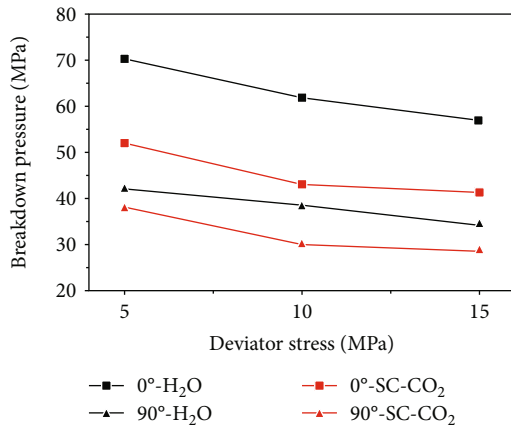


FIGURE 6: Influence of deviator stress on breakdown pressure with bedding plane angles 0° and 90°.

the specimens with bedding plane angle of 30° and 60° propagate across the bedding plane initially before being arrested. Both of the propagating across and propagating along the bedding plane occur in the specimens with bedding plane angle of 0°, in which the fracture can cut across the bedding plane before opening it. Comparing with the fracture formed

by water fracturing, the fractures formed by SC-CO₂ fracturing can be more likely to have steep dips as shown in Figure 7(b). Most of the specimens using SC-CO₂ have fracture propagations across the bedding planes. Influenced by the bedding plane, local fractures also happen to deflect during the fracture propagation. The specimen with bedding plane angle of 45° shows the fracture propagation across the bedding plane initially before being arrested. According to the results of shale breakdown pressures, the hydraulic fracture propagation patterns have an obvious effect on the breakdown pressures with higher values across the bedding planes while relatively lower values along the bedding planes.

3.5. Evolution of the Fracture Width. In the fracturing experiment, the circumference of the specimen was monitored by circumferential extensometer installed in the compression chamber (Figure 8). The monitoring of circumference can reflect the evolution process of the fracture width to a large extent (Figure 9). The following equation can be used for the calculation of the width of main fracture.

$$D_f = \frac{\Delta C}{2}, \quad (2)$$

TABLE 4: Reduction proportion of shale breakdown pressure under different deviator stresses.

No.	Bedding plane angle	Fracturing fluid	Deviator stress (MPa)	Breakdown pressure (MPa)	Reduction proportion $((P_5 - P_{15})/P_5) * 100\%$
W1	0°	Water	5	70.37	19%
W9	0°		15	57.02	
W7	90°		5	42.45	
W11	90°		15	34.53	
S1	0°	SC-CO ₂	5	52.15	21%
S9	0°		15	41.31	
S7	90°		5	38.04	
S11	90°		15	28.88	

P_5 denotes the breakdown pressure of shale under the deviator stress of 5 MPa in hydraulic fracturing using water or SC-CO₂. P_{15} denotes the breakdown pressure of shale under the deviator stress of 15 MPa in hydraulic fracturing using water or SC-CO₂.

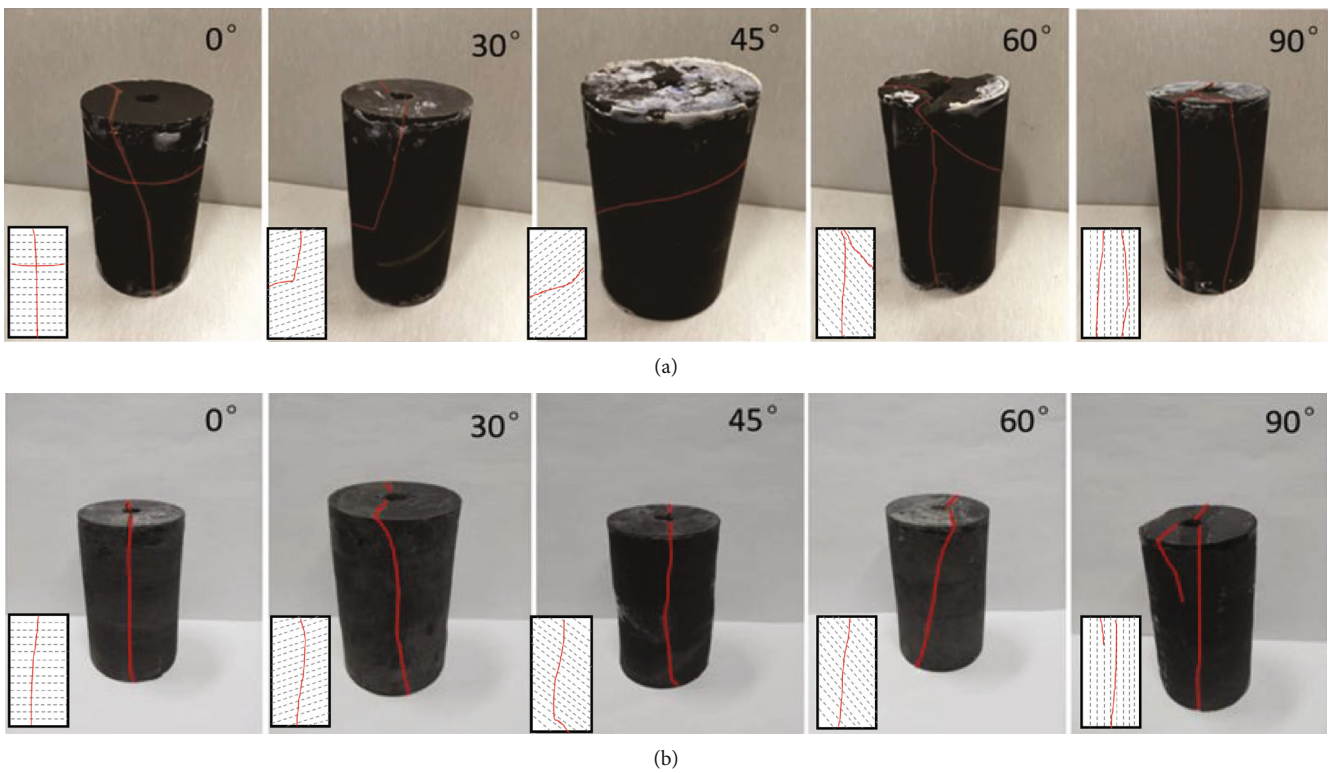


FIGURE 7: Macroobservation of the shale fracture morphology after fracturing. (a) Shale specimens with different bedding plane angles fractured using water. (b) Shale specimens with different bedding plane angles fractured using SC-CO₂. (The left-bottom diagrams show the relative orientation of hydraulic fracture with respect to the bedding plane. The red lines represent the macrofractures while the dashed lines represent the bedding planes.)

where ΔC means the variation of the circumference [38]. To improve the accuracy of fracture width calculation, the specimens with simple and symmetrical fracture morphology were selected for the study. It should be mentioned that this is an indirect method to characterize the evolution of fracture width. Table 5 shows the fracture width at different stages during the fracturing using water and SC-CO₂, which include maximum fracture width when the breakdown occurred (circumference from fracture initiation to the valley), opening fracture width during the equilibrium state (circumference

from fracture initiation to the stable), closure of the fracture (circumference from fracture stable to the valley), and the closure proportion that the fracture closure takes in the maximum width.

Comparing the experiment results of the specimens with bedding plane angles of 0° and 90°, the fracture widths (including the maximum width and opening width), fracture closure, and closure proportion of the specimens fractured using SC-CO₂ are greater than the corresponding values of specimens fractured using water. The volume expansion of

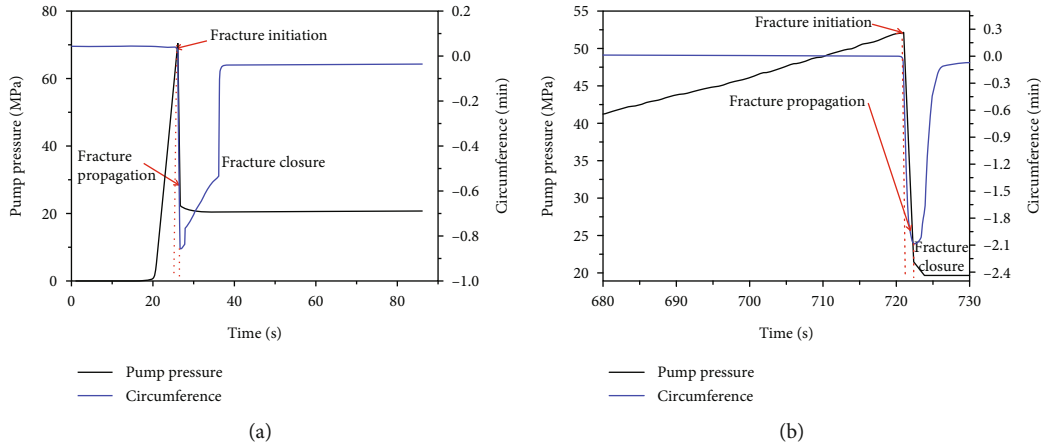


FIGURE 8: Curves of hydraulic fracturing using (a) water and (b) SC-CO₂ of shale with bedding plane angle of 0° under axial stress 25 MPa, confining pressure 20 MPa, and injection rate 0.3 ml/s. (The fracture width evolution was calculated. The maximum fracture width was calculated by the circumference difference from fracture initiation to the valley. The opening fracture width during the equilibrium state was by circumference difference from fracture initiation to the stable. The closure of the fracture was by circumference difference from fracture stable to the valley.)

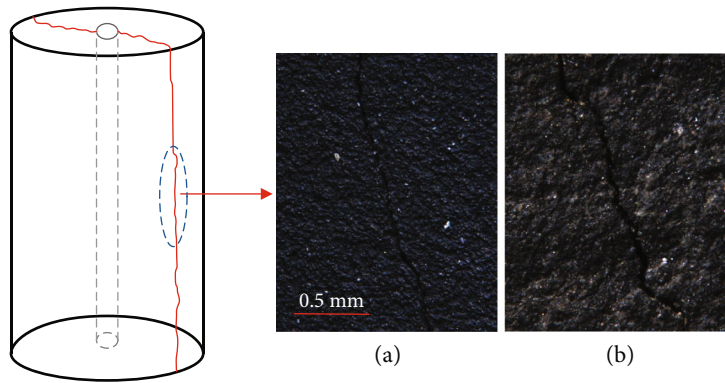


FIGURE 9: Microscopic images of the local cracks fractured using (a) water and (b) SC-CO₂.

TABLE 5: Variation of the fracture width during the hydraulic fracturing experiments.

No.	Bedding plane angle (°)	Fracturing fluid	Maximum width (mm)	Opening width (mm)	Closure (mm)	Closure proportion (closure/max) (%)
W1	0°	Water	0.428	0.019	0.409	96
S1	0°	SC-CO ₂	1.054	0.039	1.015	96
W7	90°	Water	0.052	0.014	0.038	73
S7	90°	SC-CO ₂	1.000	0.040	0.960	96

SC-CO₂ would be more significant after the fracture initiation occurs, which could result in the greater fracture width. In addition, the closure of fracture is considerable and the closure proportions are over 96.00% for SC-CO₂ fracturing, which is much greater than water fracturing. The fracture width of the initiation, propagation, and closure stages indicate that the fracture closure dominates the fracture evolution process. The fracture propping and proper size of the proppant are really important for the hydraulic fracturing.

4. Conclusion

The economic viability of shale reservoir development largely depends on the effective hydraulic fracture operation. The fracturing treatment using water has become a common method for the exploitation and SC-CO₂ fracturing, which can be seen as a promising method, really can bring some different effects to the shale reservoir. In this study, hydraulic fracturing experiments under triaxial compression using water and SC-CO₂ were carried out on the shale specimens

with different bedding plane angles for better understanding the different fracturing behavior. The following conclusions can be drawn:

- (1) Under constant injection of the fracturing fluid, the loading rate of SC-CO₂ pressure increases gradually due to the compressibility of CO₂ while the loading rate of water pressure increases sharply before it reaches the peak value during the fracturing process. Therefore, SC-CO₂ fracturing is more time-consuming which takes about 20 times more time than hydraulic fracturing using water under the same experimental conditions
- (2) Multiple external factors have influence on the breakdown pressure of shale, such as fracturing fluid and deviator stress. The shale specimens fractured using SC-CO₂ show the smaller breakdown pressure and weaker anisotropy. The breakdown pressure decreases with the increase in the deviator stress in the fracturing process, of which the reduction proportion in SC-CO₂ fracturing is slightly higher than that of water fracturing
- (3) Anisotropy of the shale caused by the variation of bedding orientation can affect the fracture propagation with respect to the bedding plane, which shows three typical patterns, including propagating across, propagating along, and being arrested. The fractures formed by SC-CO₂ are more likely to propagate across the bedding plane if compared with the fractures formed by water due to its low viscosity and strong diffusibility
- (4) The monitoring of pump pressure and circumference can indicate the evolution of hydraulic fractures. The fracture width in the process of SC-CO₂ fracturing shows greater value at different stages, which either does the closure between the breakdown and opening width. The fracture propping and proper size of the proppant are really important for the hydraulic fracturing

Data Availability

All data of the research results are presented in the paper.

Conflicts of Interest

The authors declare that they have no conflicts of interest.

Acknowledgments

This work was supported by the National Natural Science Foundation of China (Grant Nos. 41572310 and 41877270).

References


- [1] H. Wang, G. Li, and Z. Shen, "A feasibility analysis on shale gas exploitation with supercritical carbon dioxide," *Energy Sources, Part A: Recovery, Utilization, and Environmental Effects*, vol. 34, no. 15, pp. 1426–1435, 2012.

- [2] C. Zou, D. Dong, S. Wang et al., "Geological characteristics and resource potential of shale gas in China," *Petroleum Exploration and Development*, vol. 37, no. 6, pp. 641–653, 2010.
- [3] B. Faraj and M. Brown, *AV Key Attributes of Canadian and US Productive Shales: Scale and Variability*, AAPG Annual Convention, New Orleans, LA, USA, 2010.
- [4] G. E. King, "Thirty years of gas shale fracturing: what have we learned?," in *SPE Annual Technical Conference and Exhibition*, Florence, Italy, September 2010.
- [5] M. C. Vincent, "Refracs: why do they work, and why do they fail in 100 published field studies?," in *SPE Annual Technical Conference and Exhibition*, Florence, Italy, September 2010.
- [6] R. S. Middleton, J. W. Carey, R. P. Currier et al., "Shale gas and non-aqueous fracturing fluids: opportunities and challenges for supercritical CO₂," *Applied Energy*, vol. 147, no. 3, pp. 500–509, 2015.
- [7] B. R. Scanlon, R. C. Reedy, and J. P. Nicot, "Comparison of water use for hydraulic fracturing for unconventional oil and gas versus conventional oil," *Environmental Science & Technology*, vol. 48, no. 20, pp. 12386–12393, 2014.
- [8] R. E. Jackson, A. W. Gorody, B. Mayer, J. W. Roy, M. C. Ryan, and D. R. van Stempvoort, "Groundwater protection and unconventional gas extraction: the critical need for field-based hydrogeological research," *Ground Water*, vol. 51, no. 4, pp. 488–510, 2013.
- [9] H. Emadi, M. Y. Soliman, R. Samuel, L. R. Heinze, R. B. Moghaddam, and S. Hutchison, "An experimental study of the swelling properties of unconventional shale oil rock samples using both water-based and oil-based muds," in *SPE/IADC Drilling Conference and Exhibition*, London, England, UK, March 2015.
- [10] K. Makhanov, A. Habibi, H. Dehghanpour, and E. Kuru, "Liquid uptake of gas shales: a workflow to estimate water loss during shut-in periods after fracturing operations," *Journal of Unconventional Oil and Gas Resources*, vol. 7, pp. 22–32, 2014.
- [11] H. Dehghanpour, H. A. Zubair, A. Chhabra, and A. Ullah, "Liquid intake of organic shales," *Energy & Fuels*, vol. 26, no. 9, pp. 5750–5758, 2012.
- [12] R. Heller and M. Zoback, "Adsorption of methane and carbon dioxide on gas shale and pure mineral samples," *Journal of Unconventional Oil and Gas Resources*, vol. 8, pp. 14–24, 2014.
- [13] J. W. Jung, D. N. Espinoza, and J. C. Santamarina, "Properties and phenomena relevant to CH₄-CO₂ replacement in hydrate-bearing sediments," *Journal of Geophysical Research Atmospheres*, vol. 115, no. B10, pp. 155–162, 2010.
- [14] A. Abedini and F. Torabi, "On the CO₂ storage potential of cyclic CO₂ injection process for enhanced oil recovery," *Fuel*, vol. 124, pp. 14–27, 2014.
- [15] K. E. Frieauf and M. M. Sharma, "Fluid selection for energized hydraulic fractures," in *SPE Annual Technical Conference and Exhibition*, New Orleans, LA, USA, October 2009.
- [16] A. P. Gupta, A. Gupta, and J. Langlinais, "Feasibility of Supercritical Carbon Dioxide as a Drilling Fluid for Deep Underbalanced Drilling Operation," in *SPE Annual Technical Conference and Exhibition*, Dallas, TX, USA, October 2005.
- [17] W. Yu, H. R. Lashgari, K. Wu, and K. Sepehrnoori, "CO₂ injection for enhanced oil recovery in Bakken tight oil reservoirs," *Fuel*, vol. 159, pp. 354–363, 2015.

- [18] Y. Gensterblum, A. Busch, and B. M. Krooss, "Molecular concept and experimental evidence of competitive adsorption of H₂O, CO₂ and CH₄ on organic material," *Fuel*, vol. 115, pp. 581–588, 2014.
- [19] T. Ishida, Q. Chen, Y. Mizuta, and J. C. Roegiers, "Influence of fluid viscosity on the hydraulic fracturing mechanism," *Journal of Energy Resources Technology*, vol. 126, no. 3, pp. 190–200, 2004.
- [20] T. Ishida, K. Aoyagi, T. Niwa et al., "Acoustic emission monitoring of hydraulic fracturing laboratory experiment with supercritical and liquid CO₂," *Geophysical Research Letters*, vol. 39, no. 16, article 16309, 2012.
- [21] S. Inui, T. Ishida, Y. Nagaya, Y. Nara, Y. Chen, and Q. Chen, "AE monitoring of hydraulic fracturing experiments in granite blocks using SC-CO₂, water and viscous oil," in *48th US Rock Mechanics/Geomechanics Symposium*, Minneapolis, MN, USA, June 2014.
- [22] Y. Chen, Y. Nagaya, and T. Ishida, "Observations of fractures induced by hydraulic fracturing in anisotropic granite," *Rock Mechanics and Rock Engineering*, vol. 48, no. 4, pp. 1455–1461, 2015.
- [23] X. Zhou and T. J. Burbey, "Fluid effect on hydraulic fracture propagation behavior: a comparison between water and supercritical CO₂-like fluid," *Geofluids*, vol. 14, no. 2, pp. 174–188, 2014.
- [24] T. Fan and G. Zhang, "Laboratory investigation of hydraulic fracture networks in formations with continuous orthogonal fractures," *Energy*, vol. 74, pp. 164–173, 2014.
- [25] W. Cheng, Y. Jin, and M. Chen, "Experimental study of step-displacement hydraulic fracturing on naturally fractured shale outcrops," *Journal of Geophysics and Engineering*, vol. 12, no. 4, pp. 714–723, 2015.
- [26] X. Zhang, Y. Lu, J. Tang, Z. Zhou, and Y. Liao, "Experimental study on fracture initiation and propagation in shale using supercritical carbon dioxide fracturing," *Fuel*, vol. 190, pp. 370–378, 2017.
- [27] D. Zhou, G. Zhang, X. Zhang et al., "Effects of super-critical CO₂ phase change on dynamic multi-fracturing process in reservoir stimulation," in *51th U.S. Rock Mechanics/Geomechanics Symposium*, San Francisco, CA, USA, June 2017.
- [28] D. N. Dewhurst and A. F. Siggins, "Impact of fabric, micro-cracks and stress field on shale anisotropy," *Geophysical Journal of the Royal Astronomical Society*, vol. 165, no. 1, pp. 135–148, 2006.
- [29] J. E. Johnston and N. I. Christensen, "Seismic anisotropy of shales," *Journal of Geophysical Research Solid Earth*, vol. 100, no. B4, pp. 5991–6003, 1995.
- [30] H. Kim, J. W. Cho, I. Song, and K. B. Min, "Anisotropy of elastic moduli, p-wave velocities, and thermal conductivities of Asan gneiss, Boryeong shale, and Yeoncheon schist in Korea," *Engineering Geology*, vol. 147–148, no. 5, pp. 68–77, 2012.
- [31] A. Zhubayev, M. E. Houben, D. M. J. Smeulders, and A. Barnhoorn, "Ultrasonic velocity and attenuation anisotropy of shales, Whitby, United Kingdom," *Geophysics*, vol. 81, no. 1, pp. D45–D56, 2016.
- [32] Z. K. Hou, C. H. Yang, Y. T. Guo et al., "Experimental study on anisotropic properties of Longmaxi formation shale under uniaxial compression," *Rock and Soil Mechanics*, vol. 36, pp. 2541–2550, 2015.
- [33] J. He and L. O. Afolagboye, "Influence of layer orientation and interlayer bonding force on the mechanical behavior of shale under Brazilian test conditions," *Acta Mechanica Sinica*, vol. 34, no. 2, pp. 349–358, 2018.
- [34] Y. Chuanliang, D. Jingen, H. Lianbo et al., "Brittle failure of shale under uniaxial compression," *Arabian Journal of Geosciences*, vol. 8, no. 5, pp. 2467–2475, 2015.
- [35] D. R. Schmitt and M. D. Zoback, "Poroelastic effects in the determination of the maximum horizontal principal stress in hydraulic fracturing tests—a proposed breakdown equation employing a modified effective stress relation for tensile failure," *International Journal of Rock Mechanics and Mining Sciences & Geomechanics Abstracts*, vol. 26, no. 6, pp. 499–506, 1989.
- [36] S. Timoshenko and J. N. Goodier, *Theory of Elasticity*, McGraw-Hill Book Company, 2nd edition, 1951.
- [37] D. Xu, R. Hu, W. Gao, and J. Xia, "Effects of laminated structure on hydraulic fracture propagation in shale," *Petroleum Exploration and Development*, vol. 42, no. 4, pp. 573–579, 2015.
- [38] J. He, C. Lin, X. Li, Y. Zhang, and Y. Chen, "Initiation, propagation, closure and morphology of hydraulic fractures in sandstone cores," *Fuel*, vol. 208, pp. 65–70, 2017.

Research Article

Geological Structural Surface Evaluation Model Based on Unascertained Measure

Kang Zhao ^{1,2}, Qing Wang,¹ Yajing Yan,¹ Junqiang Wang,² Kui Zhao,¹ Shuai Cao,³ and Yongjun Zhang⁴

¹School of Architectural and Surveying & Mapping Engineering, Jiangxi University of Science and Technology, Ganzhou 341000, China

²Lingbao Jinyuan Mining Company Limited, Lingbao 472500, China

³School of Civil and Resources Engineering, University of Science and Technology Beijing, Beijing 100083, China

⁴School of Civil Engineering, Qingdao University of Technology, Qingdao 266033, China

Correspondence should be addressed to Kang Zhao; zhaok_666666@163.com

Received 6 August 2019; Accepted 2 November 2019; Published 9 December 2019

Guest Editor: Paolo Dabove

Copyright © 2019 Kang Zhao et al. This is an open access article distributed under the Creative Commons Attribution License, which permits unrestricted use, distribution, and reproduction in any medium, provided the original work is properly cited.

The surrounding rock structure plane survey is the basis for mine geological structure evaluation and stability of surrounding rock. On the basis of the unascertained measurement theory and scanline method, the surrounding rock stability of the underground geological structure plane in Lingbao Luoshan Gold Mine is evaluated. First, according to the structural plane five grading standards, the 9 single-index measure functions are constructed. Second, the information entropy is used to determine the weight of each indicator. Accordingly, a multi-index comprehensive measure evaluation vector is established. Finally, the confidence level is used to determine the structural plane stability level. Results show that surrounding rock grades of middle sections of R_1 , R_2 , and R_3 are Grades III, IV, and IV in Lingbao Luoshan Gold Mine, respectively. The evaluation grade is consistent with the actual situation of the mine, and strengthening the surrounding rock support for the middle sections of R_2 and R_3 is necessary. According to engineering practice, the evaluation model of the underground structure of metal mines established in this study has a practical value.

1. Introduction

The structural plane survey is the basis for understanding the geological structure, geostress analysis, and surrounding rock stability evaluation of mining areas. The structural face is a discontinuous surface with low or no tensile strength, including all geological separation surfaces. Different structural planes have different mechanical properties and scales, and common structural planes are divided into fractures, cleavage, unconformity, and folds. Rock mass discontinuity is caused by the existence of joints (faults, joints, and folds). On the one hand, when the rock mass is relatively complete, it can be analyzed by using the mechanical method of continuous media. On the other hand, when the rock mass has good integrity, it can be analyzed by using the mechanical method

of the continuous medium. However, the majority of rock masses are discontinued bodies formed by cutting the plurality of structural planes and has anisotropy. The structural surface can be used to reflect the geological structure within the area because its presence reduces the strength of the rock mass. Soft mud and weak surface in the interlayer often cause remarkable harm in engineering [1] (as shown in Figure 1). Hence, investigating and analyzing structural planes in engineering are often necessary.

According to the classification standard of engineering rock mass, the structural plane scale is divided into five grades. The length of structural planes I, II, and III is several tens or even hundreds of meters and directly affects the stability of the entire engineering rock mass. Grades IV and V are mainly statistical structural planes. A structural plane



FIGURE 1: Collapsed highway slope.

destroys the rock mass integrity and affects the physical-mechanical properties and stress distribution state. The distribution of structural planes IV and V is random. Hence, statistical methods are needed to investigate the structural plane. Common survey methods include statistical window, borehole lithology, and scanline [2, 3]. Zhao et al. [4] used a detailed scanline method to investigate the structural plane of tungsten mines. García-Luna et al. [5] applied digital camera technology to structural surface analysis, thereby providing a new idea for structural surface investigation. As the distribution of structural planes is affected by many factors, randomness and uncertainty exist in its distribution. Therefore, Hekmatnejad et al. [6] evaluated the methods of statistical analysis of joint length and distribution utilization probability. Yang et al. [7] estimated the length and distribution of the joints by using the probabilistic method.

The engineering rock mass classification standards commonly used in engineering mainly adopt the RMR classification [8] method and the Q classification method [9]. The RMR classification method is the uniaxial compressive strength (P1), rock quality index (P2), joint spacing (P3), joint condition (P4), groundwater condition (P5) of the rock block, and the orientation and foundation according to the joint plane, and the edge. The correction coefficient (P6) determined by the between the slope and the cavity is six signals as basic boundaries. According to the condition of the rock mass, the RMR total score of the rock mass quality can be obtained by scoring and adding one by one. With more influencing, such as groundwater, blast damage, stress changes, and other effects on the stability of surrounding rock, it is necessary to improve the RMR classification method. Barton et al. [9] proposed the Q grading method is based on the full strength of the rock, the shear strength of the chimeric rock mass, and the active stress product of the surrounding rock. Neither of these methods considers many uncertainties in the stability evaluation of surrounding rock. Uncertain measures can solve the uncertain reasons in the evaluation problem. The quantitative signals are used for analysis, and the weight of each is considered. Reduce the error of people's subjective evaluation. The unascertained mathematical theory established by Liu et al. [10] was based on the unascertained information and mathematical processing proposed by Professor Wang Guangyuan [11] in his earlier days. Unascertained information is defined as indeter-

minate information that is different from fuzzy, random, and gray information [12–14]. Unascertained measure theory is widely used in risk assessment in fields, such as slope risk assessment, urban environmental assessment, underground goaf collapse, enterprise innovation capability evaluation, and coal mine safety assessment [15–17].

In this study, on the basis of the unascertained measure theory, influencing factors and grading standards are determined based on the survey scanline structure and engineering rock mass grading standards. Influencing factors mainly include structural surface lithology, rock quality designation, rock integrity coefficient, joint mean track length, joint occurrence, joint spacing, joint roughness, joint opening degree, and water seepage on the rock surface. We investigate the structural plane by using the scanline method in the three production middle sections of Luoshan Gold Mine located in Lingbao City. This study establishes a single-indicator measure function and uses information entropy [18] to determine the weight of each indicator first. A multi-indicator measure function is then established. Finally, the confidence criteria to analyze the results are used. Research shows that the unascertained measure theory is suitable for structural plane evaluation. A new method is proposed for evaluating the stability of surrounding rock and performing support measures.

2. Unascertained Measure Theory

When n evaluation influencing factors exist in an evaluation object, these factors are recorded as $X_1, X_2, X_3, \dots, X_n$, and the survey evaluation space is recorded as $X = \{X_1, X_2, \dots, X_n\}$ ($i = 1, 2, \dots, n$). Each evaluation factor includes an m evaluation index, and the index space is recorded as $I = \{I_1, I_2, \dots, I_m\}$ ($j = 1, 2, \dots, m$). x_{ij} represents the evaluation value of the j th indicator of the i th evaluation influencing factor. p levels exist in x_{ij} , and C_k is the evaluation level k as C_k ($k = 1, 2, \dots, p$). If the k th level is stronger than the $k + 1$ th level, then this lever is recorded as $C_k > C_{k+1}$. If $C_1 > C_2 > \dots > C_p$, then $\{C_1, C_2, \dots, C_m\}$ is an ordered segmentation class of the evaluation space U .

2.1. Single-Index Unascertained Measure. If $u_{ijk} = u(x_{ij} \in C_k)$ represents the degree to which the observed value x_{ij} belongs to the k th evaluation level C_k , and it satisfies boundedness, normality, and additivity, then it can be expressed as the following relationship:

$$0 \leq u(x_{ij} \in C_k) \leq 1, \quad (1)$$

$$u(x_{ij} \in U) = 1, \quad (2)$$

$$u\left(x_{ij} \in \bigcup_{l=1}^k C_l\right) = \sum_{l=1}^k u_{ij}(x_{ij} \in C_l), \quad (3)$$

where u is the unascertained degree that is generally referred to as the measure. If u fails to satisfy Formulas

(1) to (3), then the value of u cannot guarantee its correctness. $(u_{ijk})_{n \times p}$ is a single-index evaluation matrix that uses a linear unascertained measure function and can be expressed as

$$(u_{ijk})_{n \times p} = \begin{bmatrix} u_{i11} & u_{i12} & \cdots & u_{i1p} \\ u_{i21} & u_{i22} & \cdots & u_{i2p} \\ \cdots & \cdots & \cdots & \cdots \\ u_{in1} & u_{in2} & \cdots & u_{inp} \end{bmatrix}. \quad (4)$$

2.2. Determining the Weight of Indicators. Let w_j be the weight of X_j , and w_j denotes the relative importance degree of the measurement index x_{ij} compared with other indicators, $0 \leq w_j \leq 1$, $\sum_{j=1}^n w_j = 1$, where $w = \{w_1, w_2, \dots, w_n\}$ is called the index weight vector. By using the information entropy [16] theory to determine the index weight, we obtain

$$v_j = 1 + \frac{1}{\lg p} \sum_{k=1}^p u_{jk} \lg u_{jk}, \quad (5)$$

$$w_j = \frac{v_j}{\sum_{i=1}^m v_i}. \quad (6)$$

As the evaluation matrix of a single-index measure is known, the weight w_j of each index can be obtained by using Formulas (5) and (6).

2.3. Multi-Index Comprehensive Measure Evaluation Vector. If $u = u_0$ ($R \in C_k$) indicates the degree to which the evaluation target R belongs to the k th evaluation level, then

$$u_{ik} = \sum_{j=1}^n w_j u_{ijk}, \quad (7)$$

where w_j is the weight of the indicator I_j that satisfies

$$\begin{aligned} 0 &\leq w_j \leq 1, \\ \sum_{j=1}^m w_j &= 1. \end{aligned} \quad (8)$$

u_{ik} satisfies the following relationships:

$$\begin{aligned} 0 &\leq u_{ik} \leq 1, \\ \sum_{k=1}^p u_k &= 1. \end{aligned} \quad (9)$$

u_k is the uncertainty degree determined by using Equation (4). $u_k = (u_1, u_2, \dots, u_k)$ is a multi-index comprehensive measure evaluation vector of the evaluation object.

2.4. Confidence Recognition Criteria. Use the confidence recognition criteria, confidence λ (normally $\lambda = 0.6$ or 0.7), for the sequence $C_1 > C_2 > \dots > C_p$ to satisfy the following formula:

$$k_0 = \min \left\{ k : \sum_{i=1}^k u_i > \lambda, k = 1, 2, \dots, p \right\}. \quad (10)$$

Then, the evaluation object belongs to the k_0 evaluation level grade C_{k_0} .

3. Steps in the Structural Surface Evaluation Analysis Based on Unascertained Measure

- (1) Determine the influencing factors and classification criteria for structural surface evaluation. The main influencing factors of structural plane survey based on the scanline method include lithology, rock quality designation, rock integrity, joint track length, joint occurrence, fracture roughness, joint opening degree, and rock moisture content
- (2) Determine the single-index unascertained measure function of the structural plane evaluation according to the grading standard
- (3) Determine the evaluation matrix according to measured structural surface indicators and the single unascertained measure function
- (4) By using information entropy to determine the weight of the evaluation index, the multi-index measure evaluation vector is obtained via Formula (7)
- (5) Evaluate the structural plane level by using the confidence criteria

4. Case Study

The Luoshan Gold Mine at Lingbao City is located in the Xiaoqingling District in the southern margin of the North China Platform. The lithology of the mining area is mainly composed of black cloud slanted gneiss, mixed gneiss, and mixed granite. Fault structures are well developed in the mining area. An ore-controlling structure is a set of ductile shear zones and faults that are distributed near the east-west direction. This structure generally occurs near the east-west direction and slightly inclined to the north. The majority of inclination angles are gently inclined between 30° and 40° with a few steeply reaching 60° .

Gold ore bodies, produced in ductile shear zones and faults, are strictly controlled by fault structures. The main surrounding rock is composed of fragmented mixed granite. In recent years, the frequent occurrence of ground pressure activities is caused by the formation of a large number of goafs via stratified caving. Mining pressure activities remarkably threatens the safety of mining workers. Mining methods need to be optimized to ensure safe production in mines.

Structural planes of the three middle operations (R_1 , R_2 , and R_3) are evaluated from top to bottom. Sections R_1 and R_2 are mainly composed of mixed granite, and section R_3 is mixed with gneiss.

4.1. Structural Surface Evaluation Indicators and Grading Standards. Line surveying method is mainly used for statistical investigation of microstructural planes of Grades IV and V. Based on investigation and experimental results, the rock uniaxial compressive strength R_c , engineering rock quality index RQD , rock integrity coefficient Kv , joint trace length L , and joint occurrence (strike angle θ_1 and dip angle θ_2 , where θ_1 and θ_2 are calculated by using the dominant structural plane, and strike angle θ_1 represents the strike difference between joint and roadway), fracture roughness coefficient JCR , joint opening degree B , and rock moisture content ω are the main parameters that represent the rock mass quality. According to the engineering rock mass quality grading standards [19], Table 1 lists the structural surface grading standards. Table 2 presents the parameters of each middle section.

4.2. Single-Index Measure Function Model. On the basis of the evaluation criteria of the rock structural plane, the single-index measure function of uniaxial compressive strength R_c , rock quality designation RQD , rock integrity coefficient Kv , joint trace length L , joint occurrence (strike θ_1 and dip angle θ_2), fracture roughness coefficient JCR , joint opening degree B , and rock moisture content ω was established as shown in Figures 2–10.

The parameters in Table 2 show that the evaluation matrix of each middle section is obtained from the graph. Taking middle section R_1 as an example, the evaluation matrix is calculated as follows:

$$(u_{1jk})_{9 \times 5} = \begin{bmatrix} 0 & 0 & 1 & 0 & 0 \\ 0 & 0 & 0 & 0 & 1 \\ 0 & 0 & 0.6 & 0.4 & 0 \\ 0 & 0 & 0.75 & 0.25 & 0 \\ 0 & 0.875 & 0.125 & 0 & 0 \\ 0 & 0 & 0 & 0.4 & 0.6 \\ 0 & 1 & 0 & 0 & 0 \\ 0 & 0 & 0.231 & 0.769 & 0 \\ 0.25 & 0.75 & 0 & 0 & 0 \end{bmatrix}. \quad (11)$$

4.3. Multi-Index Comprehensive Measure Evaluation Vector. Information entropy is used to determine the weight of each indicator. From Equations (5) and (6), the weight vector of middle section R_1 is $W = \{0.145, 0.145, 0.084, 0.094, 0.111, 0.084, 0.145, 0.096, 0.094\}$. The specific calculation process is as follows:

$$\begin{aligned} v_1 = v_2 = v_7 &= 1 + \frac{1}{\lg 5} (1 \lg 1 + 0) = 1, \\ v_3 = v_6 &= 1 + \frac{1}{\lg 5} (0.6 \lg 0.6 + 0.4 \lg 0.4) = 0.582, \\ v_4 = v_9 &= 1 + \frac{1}{\lg 5} (0.75 \lg 0.75 + 0.25 \lg 0.25) = 0.651, \\ v_5 &= 1 + \frac{1}{\lg 5} (0.875 \lg 0.2 + 0.125 \lg 0.125) = 0.766, \\ v_8 &= 1 + \frac{1}{\lg 5} (0.231 \lg 0.231 + 0.769 \lg 0.769) = 0.664, \\ v &= v_1 + v_2 + v_3 + v_4 + v_5 + v_6 + v_7 + v_8 + v_9 = 6.896, \\ w_1 = w_2 = w_7 &= \frac{v_1}{v} = \frac{1}{6.896} = 0.145, \\ w_3 = w_6 &= \frac{v_3}{v} = \frac{0.582}{6.896} = 0.084, \\ w_4 = w_9 &= \frac{v_4}{v} = \frac{0.651}{6.896} = 0.094, \\ w_5 &= \frac{v_5}{v} = \frac{0.766}{6.896} = 0.111, \\ w_8 &= \frac{v_8}{v} = \frac{0.664}{6.896} = 0.096. \end{aligned} \quad (12)$$

The multi-index comprehensive measure evaluation vector of the middle segment of R_1 can be obtained from the weight vector W and Formula (11) as follows:

$$u_1 = \{0.024, 0.313, 0.302, 0.165, 0.195\}. \quad (13)$$

4.4. Evaluation Result Analyses. The confidence is introduced in this section to evaluate the result with a confidence value of $\lambda = 0.6$. From the multi-index comprehensive evaluation vector and confidence criterion evaluation, $k_0 = 0.024 + 0.313 + 0.302 = 0.639 > \lambda$ exist from large to small, and the structural plane evaluation level of middle section R_1 is Grade III. However, $k_0 = 0.195 + 0.165 + 0.302 = 0.769 > \lambda$ exist from small to large, and the evaluation level is also Grade III. Therefore, the two judgment results are consistent, and the structural plane evaluation level of the R_1 middle section is Grade III.

Similarly, the same method is used to evaluate the middle sections of R_2 and R_3 , and the surrounding rock stability evaluation results of the middle sections of R_2 and R_3 are all Grade IV.

From an overall view of the three middle sections, the entire area of the mining area is mainly composed of mixed granite, and the rock is broken. Joints with a trace dominant length of approximately 1 m and the dominant occurrence that substantially differs from the roadway direction have a major impact on the surrounding rock stability. These features are the main reason for the poor evaluation of the structural surface. Other major factors affecting the structural plane include lithology, rock integrity, joint trace length, and joint occurrence.

TABLE 1: Structural plane evaluation classification standard.

Influencing factor indicator	Classification criteria				
	I grade (C_1)	II grade (C_2)	III grade (C_3)	IV grade (C_4)	V grade (C_5)
Uniaxial compressive strength R_c (MPa)	>150	150~120	120~80	80~30	30~0
Rock quality designation RQD (%)	100~90	90~80	80~60	60~30	30~0
Rock integrity coefficient K_v	0.75~1	0.55~0.75	0.35~0.55	0.15~0.35	0~0.15
Joint trace length L (m)	0~0.3	0.3~0.5	0.5~0.8	0.8~1.2	1.2~1.5
Strike θ_1 ($^\circ$)	90~75	75~60	60~45	45~30	30~0
Dip angle θ_2 ($^\circ$)	0~30	30~45	45~60	60~75	75~90
Fracture roughness coefficient JCR	20~12	12~8	8~4	2~4	2~0
Joint opening degree B (mm)	0~0.2	0.2~1.0	1.0~2.0	2.0~5.0	>5
Rock moisture content ω (%)	0~20	20~30	30~45	45~65	65~100

TABLE 2: The middle section structural surface parameters.

Middle section	R_c (MPa)	RQD (%)	K_v	L (m)	θ_1 ($^\circ$)	θ_2 ($^\circ$)	JCR	B (mm)	ω (%)
R_1	120	25	0.37	0.7	54	66	8	1.2	26
R_2	95	35	0.33	0.8	67	72	6.5	2	43
R_3	100	28	0.20	1.1	43	63	5	2.5	58

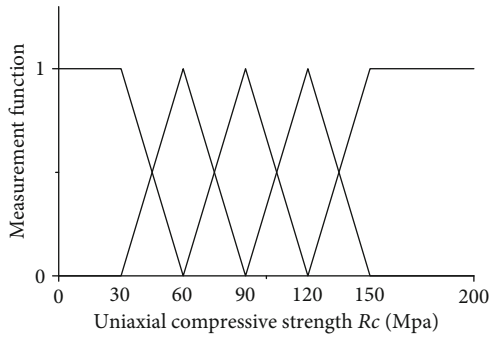


FIGURE 2: Uncertainty measurement function of R_c .

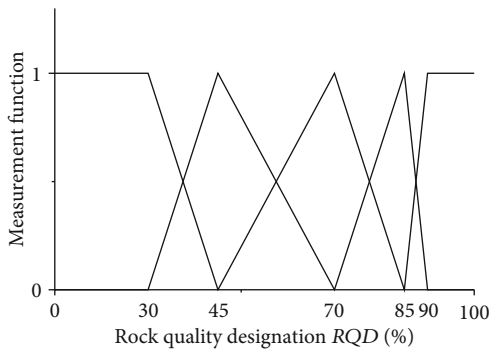


FIGURE 3: Uncertainty measurement function of RQD .

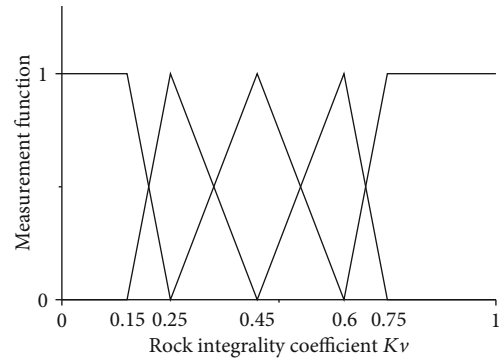


FIGURE 4: Uncertainty measurement function of rock integrity coefficient.

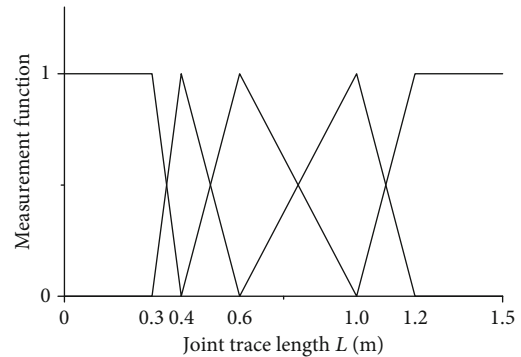


FIGURE 5: Uncertainty measurement function of joint trace length.

Looking at the relevant data of the mine, the rock in middle section R_1 is relatively dry, and the roadway surface in middle sections R_2 and R_3 is mildly to severely wet. The groundwater of middle section R_1 penetrates along the joint surface and into middle sections R_2 and R_3 because middle sections R_2 and R_3 are mined. A large amount of groundwater weakens the strength and reduces the stability of sur-

rounding rock, making the surrounding rock in middle sections R_2 and R_3 vulnerable to failure. Therefore, strengthening the support of middle sections R_2 and R_3 and improving the hydrophobic drainage of the lower middle section in time are necessary. The design of the main transportation

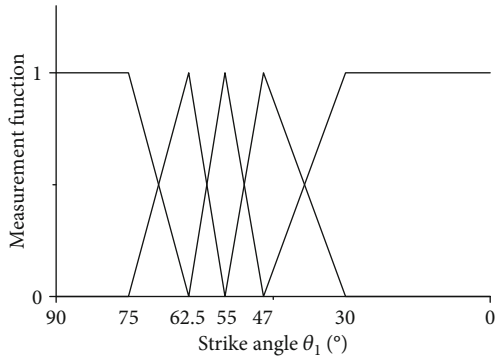


FIGURE 6: Uncertainty measurement function of joint strike angle.

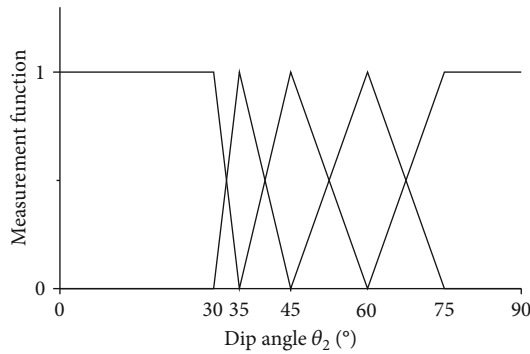


FIGURE 7: Uncertainty measurement function of joint dip angle.

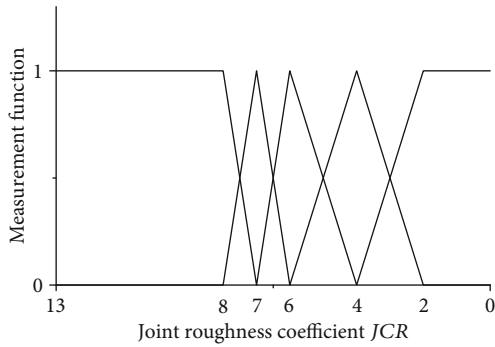


FIGURE 8: Uncertainty measurement function of joint roughness coefficient.

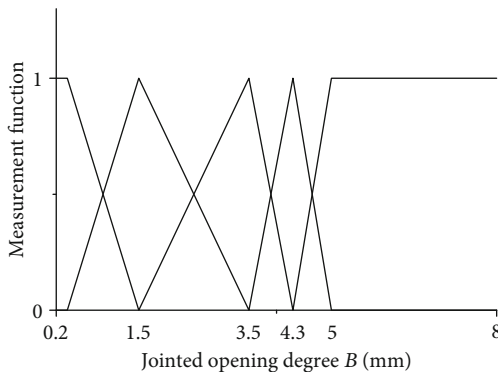


FIGURE 9: Uncertainty measurement function of jointed opening degree.

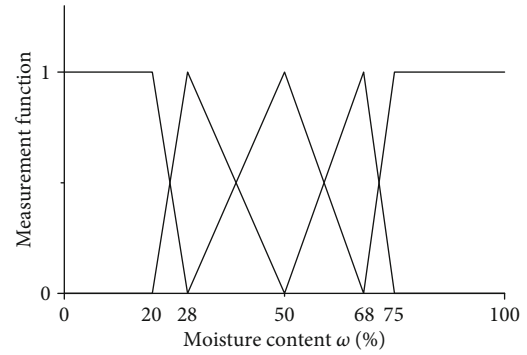


FIGURE 10: Uncertainty measurement function of rock moisture content.

lane direction should be kept as small as possible considering the dominant surface of the structural plane to avoid wider damage areas.

5. Conclusion

- (1) On the basis of the structural plane investigation via the scanline method, the evaluation factors and grading standards of the structural plane are determined. Quantitative analysis of the evaluation by using the scanline method overcomes the shortcomings of the original qualitative evaluation criteria. On the basis of the mine example, the unascertained measure theory is used in the evaluation and analysis of underground structural planes. The models of single- and comprehensive-index functions are constructed. Information entropy is used to determine the weight, whereas the confidence recognition criterion is used to evaluate the structural surface level.
- (2) From the three middle section survey results of the mine, the unascertained measure theory is suitable to evaluate the structural plane. The evaluation results show that the structural evaluation grades of R_1 , R_2 , and R_3 are Grades III, IV, and IV, respectively. Therefore, middle sections R_2 and R_3 should establish a strengthened support to ensure safe operation. The unascertained measure theory provides a new method for structural plane evaluation by using the scanline method.
- (3) As the geological structure surface is affected by many factors, further selecting accurate and reasonable underground structural surface parameters and grading standards in the future is necessary to ensure the reliability of the evaluation survey.

Data Availability

The test data used to support the findings of this study are included within the article. Readers can obtain data supporting the research results from the test data table in the paper.

Conflicts of Interest

No potential conflicts of interests were reported by the authors.

Acknowledgments

The study has been supported by the National Natural Science Foundation (No. 51764013), by the China Postdoctoral Science Foundation funded project (Grant No. 2019M652277), by the Natural Science Youth Foundation Key Projects of Jiangxi Province of China (Grant No. 20192ACBL21014), and by the Jiangxi Province Postdoctoral Science Foundation funded project (Grant No. 2018KY356).

References

- [1] M. Koopialipoor, D. Jahed Armaghani, A. Hedayat, A. Marto, and B. Gordan, "Applying various hybrid intelligent systems to evaluate and predict slope stability under static and dynamic conditions," *Soft Computing*, vol. 23, no. 14, pp. 5913–5929, 2019.
- [2] M. Mauldon, W. M. Dunne, and M. B. Rohrbaugh Jr., "Circular scanlines and circular windows: new tools for characterizing the geometry of fracture traces," *Journal of Structural Geology*, vol. 23, no. 2-3, pp. 247–258, 2001.
- [3] G. H. Davis, S. J. Reynolds, C. F. Kluth, and C. Kluth, *Structural Geology of Rocks and Regions*, John Wiley & Sons, 2011.
- [4] K. Zhao, K. Zhou, J. Zhang, X. Tu, and K. Zhao, "Analysis of structure plane characteristic for rock mass of a tungsten mine," *Metal Mine*, vol. 12, pp. 1–5, 2017.
- [5] R. García-Luna, S. Senent, R. Jurado-Piña, and R. Jimenez, "Structure from motion photogrammetry to characterize underground rock masses: experiences from two real tunnels," *Tunnelling and Underground Space Technology*, vol. 83, pp. 262–273, 2019.
- [6] A. Hekmatnejad, X. Emery, and J. A. Vallejos, "Robust estimation of the fracture diameter distribution from the true trace length distribution in the Poisson-disc discrete fracture network model," *Computers and Geotechnics*, vol. 95, pp. 137–146, 2018.
- [7] C. Yang, H. Bao, G. Wang, and T. Mei, "Estimation of mean trace length and trace midpoint density of rock mass joints," *Yanshilixue Yu Gongcheng Xuebao/Chinese Journal of Rock Mechanics and Engineering*, vol. 25, no. 12, pp. 2475–2480, 2006.
- [8] Z. T. Bieniawski, "Classification of rock masses for engineering: the RMR system and future trends," in *In Rock Testing and Site Characterization*, pp. 553–573, Elsevier, Pergamon, 1993.
- [9] N. Barton, R. Lien, and J. Lunde, "Engineering classification of rock masses for the design of tunnel support," *Rock Mechanics*, vol. 6, no. 4, pp. 189–236, 1974.
- [10] K. Liu, Y. Lin, and L. Yao, "Informational uncertainties and their mathematical expressions," *Kybernetes*, vol. 30, no. 4, pp. 378–397, 2001.
- [11] G. Y. Wang, "Uncertainty information and its mathematical treatment," *Journal of Harbin University of Civil Engineering and Architecture*, vol. 23, no. 4, pp. 1–9, 1990.
- [12] L. A. Zadeh, "Fuzzy sets," *Information and Control*, vol. 8, no. 3, pp. 338–353, 1965.
- [13] G. Matheron, *Random Sets and Integral Geometry*, Wiley, New York, 1975.
- [14] D. Ju-Long, "Control problems of grey systems," *Systems and Control Letters*, vol. 1, no. 5, pp. 288–294, 1982.
- [15] S. C. Li, J. Wu, Z. H. Xu, and L. P. Li, "Unascertained measure model of water and mud inrush risk evaluation in karst tunnels and its engineering application," *KSCE Journal of Civil Engineering*, vol. 21, no. 4, pp. 1170–1182, 2017.
- [16] C. Huang, S. Tian, Q. Li, and J. Huang, "Evaluation of rock quality of tunnel wall rock based on rough set theory and unascertained measurement theory," *Mathematical Problems in Engineering*, vol. 2018, 10 pages, 2018.
- [17] Y. Z. Chang and S. C. Dong, "Study on evaluation model of international trade in agricultural products based on unascertained measure," *Chemical Engineering Transactions*, vol. 51, pp. 673–678, 2016.
- [18] A. Shamilov, "Generalized entropy optimization problems and the existence of their solutions," *Physica A: Statistical Mechanics and its Applications*, vol. 382, no. 2, pp. 465–472, 2007.
- [19] V. M. Khatik and A. K. Nandi, "A generic method for rock mass classification," *Journal of Rock Mechanics and Geotechnical Engineering*, vol. 10, no. 1, pp. 102–116, 2018.

Research Article

Hazard Scenarios Related to Submarine Volcanic-Hydrothermal Activity and Advanced Monitoring Strategies: A Study Case from the Panarea Volcanic Group (Aeolian Islands, Italy)

Davide Romano ^{1,2}, **Alessandro Gattuso** ¹, **Manfredi Longo** ¹, **Cinzia Caruso**¹, **Gianluca Lazzaro**¹, **Andrea Corbo**¹, and **Francesco Italiano**¹

¹*Istituto Nazionale di Geofisica e Vulcanologia, Palermo 90146, Italy*

²*Dipartimento di Scienze Matematiche e Informatiche, Scienze Fisiche e Scienze della Terra (MIFT), Università di Messina, Messina 98166, Italy*

Correspondence should be addressed to Alessandro Gattuso; alessandro.gattuso@ingv.it

Received 12 April 2019; Accepted 23 August 2019; Published 13 October 2019

Guest Editor: Alessandro Santilano

Copyright © 2019 Davide Romano et al. This is an open access article distributed under the Creative Commons Attribution License, which permits unrestricted use, distribution, and reproduction in any medium, provided the original work is properly cited.

Geohazards associated to submarine hydrothermal systems still represent a tricky enigma to face and solve for the scientific community. The poor knowledge of a submarine environment, the rare and scarce monitoring activities, and the expensive and sometimes complicated logistics are the main problems to deal with. The submarine low-energy explosion, which occurred last November 3, 2002, off the volcanic island of Panarea, highlighted the absence of any hazard scenario to be used to manage the volcanic crisis. The “*unrest*” of the volcanic activity was triggered by a sudden input of deep magmatic fluids, which caused boiling water at the sea surface with a massive CO₂ release besides changes in the fluids’ geochemistry. That event dramatically pushed scientists to develop new methods to monitor the seafloor venting activity. Coupling the information from geochemical investigations and data collected during the unrest of volcanic activity, we were able to (a) develop theoretical models to gain a better insight on the submarine hydrothermal system and its relationships with the local volcanic and tectonic structures and (b) to develop a preliminary submarine volcanic hazard assessment connected to the Panarea system (Aeolian Islands). In order to mitigate the potential submarine volcanic hazard, three different scenarios are described here: (1) ordinary hydrothermal venting, (2) gas burst, and (3) volcanic eruption. The experience carried out at Panarea demonstrates that the best way to face any submarine volcanic-hydrothermal hazard is to improve the collection of data in near real-time mode by multidisciplinary seafloor observatories and to combine it with periodical sampling activity.

1. Introduction

The seven emerged volcanoes of the Aeolian Archipelago represent the youngest volcanism that migrated southeastward from the central and southern sectors of the Tyrrhenian Sea during the Lower Pleistocene [1].

The entire volcanic arc is nowadays well known to be a multihazard prone area for which risk assessments have been constrained due to the occurrences of volcanic phenomena, seismic events, and tsunamis. According to historical catalogues [2], several strong earthquakes hit the western and central sectors of the Aeolian Archipelago (e.g., the Mw =

6.2 in March 1786 or the recent Mw = 6.1 in April 1978) related to a NNW-SSE trending right-lateral strike-slip fault system and caused severe damages and casualties in the surrounding localities [3]. On April 20, 1988, a small landslide of approximately 200,000 m³ occurred on the external northeastern flank of the “La Fossa” crater on the island of Vulcano. The landslide fell into the sea, producing a small tsunami that was locally observed in the neighbouring harbour called Porto Levante [4].

The island of Vulcano suffered a strong explosive activity during 1888-1890 at the end of 15 years of low-energy phreatic blasts [5, 6]. The products of that eruption (blocks

weighing up to 5 tons) covered the area where the tourist village is located. Recently, between 1988 and the late 90s, the volcanic activity reactivated the crater fumaroles with temperatures above 700°C; a huge amount of volcanic gases was released inside the crater. In the eastern part of the Archipelago, a variety of different eruptive periods took place at Stromboli volcano (see Francalanci et al.'s study [7] and the references therein). On December 28, 2002, a flank eruption started after almost a year of growing explosive activity from the summit craters [8]. Effusion of lava took place from several vents along the Sciara del Fuoco. Two days later, a huge flank collapse induced a 20 km³ landslide producing tsunami waves that caused damages around the island of Stromboli and other Aeolian Islands (Lipari and Vulcano) and along the Sicily and Calabria coastlines. Damages to a chemical plant and to an oil tank occurred at the industrial area in Milazzo, located 35 nautical miles away to the south of the island. Different strong paroxysms occurred at Stromboli, causing huge damages to the village of Ginostra (ca. 40 inhabitants) mainly on April 5, 2003, and March 15, 2007. The fallout of incandescent blocks with the diameters between 0.3 and 2 m reached ballistic distances from 400 to 1300 m from the craters, and some of them triggered wildfires [9]. At Stromboli (about 500 inhabitants), during the summer period, the number of residents considerably increases exceeding 5000 people [10]. The last two main eruptive crises of the Stromboli volcano of 2002–2003 and 2007 occurred in winter, which is the low-tourist season and thus did not cause any fatality. The most recent effusive eruption along the Sciara del Fuoco was in 2014; however, a permanent Strombolian explosive activity is still ongoing. The different volcanic products (blocks, ash, etc.) produce variable hazard scenarios. For instance, lava flows, pyroclastic flows, and surges are able to damage populated areas, whereas ashes emitted during intense and prolonged eruptions usually have an important effect on the air traffic. Any volcanic activity can also inject large amounts of gases and aerosols into the atmosphere during both eruptions and degassing activity, inducing a health risk for the local population. Moreover, volcanic activity can trigger secondary hazardous phenomena such as landslides and tsunamis. Different geochemical surveys carried out [11] at Vulcano island indicated that during and after periods of volcanic activity unrest, there are potential hazards deriving from endogenous gas release in the inhabited area of Vulcano Porto. The CO₂ and H₂S air concentration measurements identified sites with a significant gas hazard at Levante Beach, where intense submarine degassing activity is also present. During the summer period, the number of exposed people, mainly at the Vulcano porto area, grows exponentially, often exceeding 27.000 presences, mainly composed of tourists and seasonal workers. In wintertime, the resident population is less than 800 people.

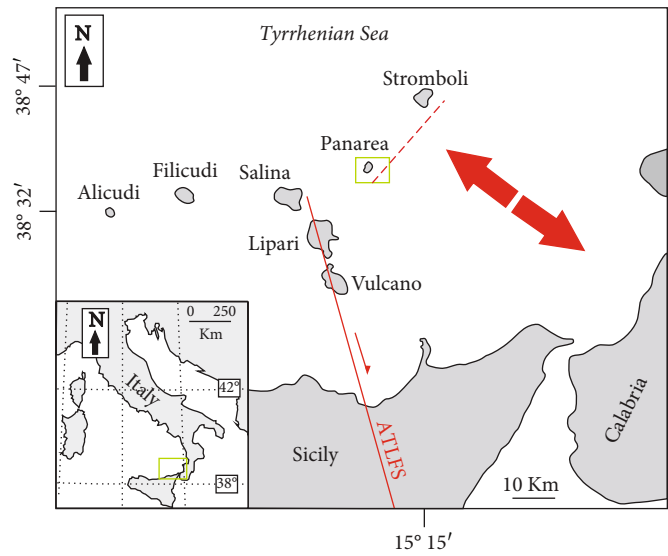
In November 3, 2002, an explosion occurred 2.5 nautical miles off Panarea island, inducing an intense and long-lasting gas eruption over a shallow depth (2 to 30 m deep) and 2.3 km² wide area surrounded by the islets of Panarelli, Lisca Bianca, Bottaro, Lisca Nera, and Dattilo [12]. The “degassing

crisis” lasted several months and killed all the living matter in the submarine area [13].

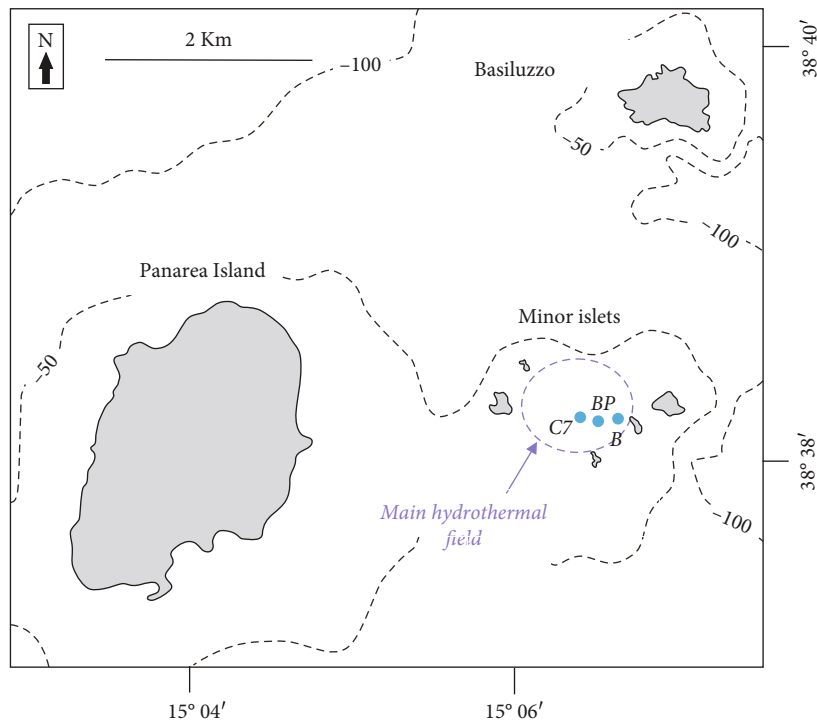
In contrast to the hazard assessment related to submarine volcanic activity, the volcanic-hydrothermal hazard assessments have never been estimated due to a range of reasons: (i) the submarine hydrothermal fields are mostly undiscovered, and the known ones are generally not easily accessible; (ii) the venting areas are commonly characterized by weak hydrothermal discharges which do not reflect the destructive potential of gas bursts; (iii) the hydrothermalism within the Mediterranean Sea is often associated with late volcanism keeping a steady state for the venting activity; (iv) the historical information of submarine gas burst events is significantly rarer compared to the catastrophic earthquakes and to the subaerial eruptions. All of the above-mentioned reasons led to the erroneous conclusion that the submarine hydrothermal activity is not hazardous.

The improvement of our knowledge about the submarine hydrothermal systems has to be framed in terms of life safety and environmental preservation. Hydrothermal fields in the Southern Tyrrhenian offshore are located over the seamounts [14–16] and in the coastal areas of the Aeolian Archipelago [17–21], in front of Capo Vaticano [22, 23], along the coast of Ischia island [19], in the Bay of Naples and Pozzuoli [24, 25], and off the coast of Ventotene and Zannone (Pontine Islands) [26, 27]. All the systems are characterized by CO₂-rich emissions and thermal waters commonly associated to past or recent volcanic activity. Moreover, investigating the hydrothermal activity, namely, the venting activity of submarine thermal fluids, especially in steady-state volcanism, is a key tool of highlighting the behavior of residual magmatic bodies at depth and the contamination of the seawater due to natural processes (hydrothermalism) in comparison to anthropic effects. It is accepted that the seeping process is driven by active tectonic lineaments which usually control the local permeability that drives the fluids upraise and their emission rates.

The well-known and documented submarine hydrothermal manifestations located at shallow depth off Panarea island (Aeolian Islands) are located inside a large paleocaldera formed in the central part of the volcanic edifice. The main exhalative field falls within the area of the minor islets (Bottaro, Dattilo, Lisca Nera, Lisca Bianca, and Panarelli; Figure 1) about 2 miles to the east of the main island [17]. The Panarea hydrothermal field has extensively been investigated for many different reasons (e.g., in [13]): it represents an important natural laboratory in order to better understand the processes governing the thermal fluid migration from the deep reservoir to the seafloor, the impact of an active hydrothermal system on the seafloor ecology, the role of bubbling and dissolved CO₂ on the living matter, and the contribution of natural gas emissions to the ocean acidifications. The geochemical features of the hot fluids provide important information on several interactions among seawater, meteoric water, magmatic gases, and hosting rocks, and they help in defining the relationship between the hot deep source and its surrounding area.



(a)



(b)

FIGURE 1: (a) Location map of the Aeolian Islands together with the main tectonic features (modified after De Astis et al. [1]). ATLFS: Aeolian-Tindari-Letojanni Fault System (Billi et al. [76]); dashed red line: N40°E fault joining Panarea and Stromboli (Heinicke et al. [43]); red arrows: late quaternary extension (Monaco and Tortorici [77]). (b) Location map of the Panarea volcanic group with the main hydrothermal field and the sampling points. C7: Campo 7 (coordinates WGS84 zone 33 N: 4276654 N-509266 E); BP: Black Point (coordinates WGS84 zone 33 N: 4276417 N-508951 E); B: Bottaro (coordinates WGS84 zone 33 N: 4276521 N-509519 E) (bathymetry after Gabbianelli et al. [34]).

The main purpose of this paper is to describe different hazard scenarios connected to the hydrothermal and volcanic activity of the Panarea volcanic island that can be of general application to correctly assess the hydrothermalism-related hazards at least at a Mediterranean scale. Moreover, we investigate on the finest monitoring strategy to adopt

in order to mitigate this kind of hazard. Considering the economic role of Panarea, one of the most important tourist destinations within the Mediterranean Sea, with an exponential increase of exposed population during the tourist season, this study could represent a useful support for the Civil Protection Authorities to perform an

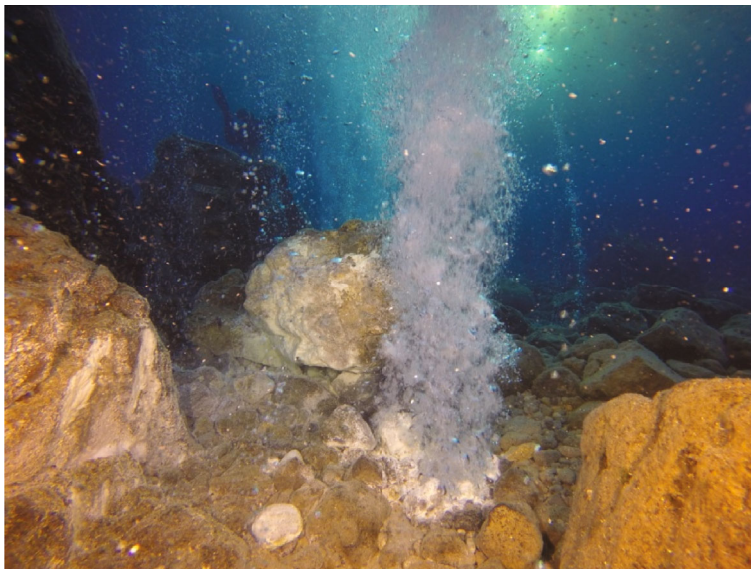


FIGURE 2: Hydrothermal fluids emitted from submarine vents at the main hydrothermal field (Bottaro location, 8 m.b.s.l., 2017).

appropriate emergency planning related to submarine volcanic phenomena.

2. Geo-Volcanological Setting

The Aeolian Archipelago is composed of seven main emerged islands (Alicudi, Filicudi, Salina, Lipari, Vulcano, Panarea, and Stromboli) (Figure 1(a)).

The Aeolian volcanism probably started during Lower Pleistocene [28], as supported by the volcanoclastic sequence interbedded within the Lower-Middle Pleistocene clays outcropping along the Tyrrhenian margin of the Peloritani Mountains [29] dated 980-589 kyr. On the contrary, the age of the oldest subaerial volcanic products has been estimated to be 260 kyr [30–32].

Panarea is located in the eastern sector of Aeolian Islands between Stromboli and Salina volcanoes (see Figure 1(a)). The Panarea edifice rises from depths of ~1700 m.b.s.l. and consists of a truncated cone hugely modified by erosion and volcano-tectonic activities. The volcanic group is commonly defined as a dome field, and the emerged part started to assemble in ~155 kyr. Around 50-60 kyr, the volcanic activity definitely shifted eastward in the minor islet area and culminated with the emplacement of the Basiluzzo dome structure. The Panarea volcanic system is formed by the main island and some minor islets (Basiluzzo, Dattilo, Panarelli, Lisca Bianca, Bottaro, and Lisca Nera) distributed over a shallow water platform (Figure 1(b)). The volcanic products drift from basaltic andesite to rhyolite compositions and show calc-alkaline and high-K calc-alkaline signatures. The main island is dissected by two tectonic systems, which have controlled the dome effusion and the feeder dyke layout. The NE-SW-oriented trend is recognized as dominant and modeled the western flank of the edifice; on the contrary, the NW-SE-oriented features are less evident and are exposed in the northern and in the southeastern portions of the island [33].

3. Submarine Hydrothermal Activity

The Panarea volcanic group hosts one of the most active submarine hydrothermal system of the Mediterranean Sea. The main submarine hydrothermal field is located within the area of the minor islets (Figure 1(b)) recognized as the remnants of a crater rim [34, 35]. As reported by Italiano and Nuccio [17], several gaseous emissions spread over the sea bottom around the Panarea area up to the northeastern margin of the Basiluzzo islet, up to a depth of 400 m (F. Italiano, personal communication). Hydrothermal fluids come out from the main tectonic directrices crossing the Aeolian arc following NE-SW and NW-SE trending alignments [17, 36]. Chimneys and other areas of venting fluids have recently been discovered between the island of Panarea and the islet of Basiluzzo, along a possible caldera border [13]. The tectonics drive the distribution of the hydrothermal vents, deposits, crusts, and mineralizations characterizing the whole Panarea offshore [37].

3.1. Fluid Geochemistry. The hydrothermal fluids vented at the sea bottom consist of both gases and thermal waters (see Figure 2) in which temperatures, detected at the emission points, are in the range of 40-140°C. Table 1 summarizes the chemical and isotopic composition of the bubbling gases collected in 2015, 2016, 2017, and 2018 from three different sites located within the main geothermal field. Gases have been sampled directly from submarine vents using an inverted funnel connected to two-way glass bottles (see Italiano's study [18] for further details). The chemical composition of the bubbling gases was determined by gas chromatography (GC) using an Agilent equipped with a double TCD-FID detector and argon as the carrier gas. The gaseous samples had been admitted to the GC by a syringe, and the uncertainties are within $\pm 5\%$. Measurements of carbon isotopic compositions ($\delta^{13}\text{C}_{\text{CO}_2}$) of the vented gases were made by a Delta Plus XP IRMS equipped with a Thermo

TABLE 1: Chemical and isotopic composition of the bubbling gases. CO₂, H₂S, N₂, and O₂ are expressed in vol. % and H₂, He, CO, and CH₄ in vol. ppm.

Sample ID	Site	Data	He	H ₂	O ₂	N ₂	CO	CH ₄	CO ₂	H ₂ S	$\delta^{13}\text{C}_{\text{CO}_2}$	R/R _A
1	Bottaro	05/05/2015	8	4,10	0,078	0,54	<1	1,20	92,30	6,16	-2,69	4,27
2	Black Point	04/06/2015	8	3,10	0,031	3,85	6	676	95,63	0,82	-2,37	4,26
3	Bottaro	05/06/2015	10	bdl	0,24	1,06	11	22	95,99	1,31	-2,66	4,23
4	Black Point	02/09/2015	12	241	0,077	0,56	<1	895	97,87	0,52	n.d.	4,19
5	Bottaro	03/09/2015	8	4,20	0,0077	0,29	<1	<1	91,69	5,63	n.d.	4,20
6	C7	03/09/2015	7	1,10	0,056	0,41	<1	177	95,35	2,28	n.d.	4,24
7	Black Point	27/09/2016	11	211	0,97	4,51	<1	775	94,19	bdl	n.d.	4,31
8	Bottaro	29/09/2016	8	bdl	0,0025	0,23	1	16	97,25	0,90	n.d.	4,31
9	Black Point	23/03/2017	11	5	0,082	0,55	13	769	98,28	0,65	n.d.	4,25
10	C7	08/05/2018	10	bdl	0,067	0,55	1,10	186	96,20	1,60	n.d.	4,11
11	Bottaro	01/06/2018	9	5	0,028	0,34	<1	<1	91,70	3,83	n.d.	4,30

bdl: below detection limits; n.d.: not detected.

TRACE GC interfaced with Thermo GC/C III. The results (expressed in $\delta^{13}\text{C}\text{‰}$) are relative to the V-PDB (Vienna-Pee Dee Belemnite) standard, and the standard deviation of the $^{13}\text{C}/^{12}\text{C}$ ratio was $\pm 0.2\text{‰}$. The He isotope ratio ($^3\text{He}/^4\text{He}$) was analyzed by a Helix SFT-Thermo static vacuum mass spectrometer after purification of He under high-vacuum and cryogenic separation from Ne. Helium isotope compositions are given as R/R_A , namely, $^3\text{He}/^4\text{He}$ of the sample versus the atmospheric $^3\text{He}/^4\text{He}$ ($R_A = 1.386 \times 10^{-6}$). Typical uncertainties are within $\pm 5\%$.

The chemical and isotopic composition of gaseous emissions collected from 2015 to 2018 is comparable to that reported in the literature (e.g., [17]) for gases sampled during prolonged steady-state conditions. Bubbling Gases exhibit high CO₂ contents (~95-98 vol. %) and variable contents of H₂S (from 0 to ~6.5 vol. %), associated to minor amounts of H₂, N₂, He, CH₄, and CO. The composition is strongly influenced by gas/water interaction (GWI) processes occurring at either high or low temperatures. GWI induces severe changes in the pristine geochemical features of the vented fluids due to the following: (i) steam condensation; (ii) loss of highly soluble species (i.e., SO₂, HCl, and HF); (iii) depletion and fractionation of soluble species partially dissolved in water (i.e., H₂S and CO₂); and (iv) enrichment in He, CH₄, and atmospheric components (i.e., O₂ and N₂) dissolved in seawater. The isotopic composition of carbon ($\delta^{13}\text{C}_{\text{CO}_2}$ varying between -1‰ and -3‰ V-PDB) and helium (R/R_A ranging from 4.1 to 4.4) clearly indicates the presence of a magmatic component in the gases [17].

The gas sample collection (2015-2018) carried out in the frame of this study is part of the periodical monitoring activity carried out by INGV over the area of Panarea.

3.2. The Submarine Panarea Crisis. The sudden unrest of submarine volcanic activity which occurred off the island of Panarea in November 2002 was interpreted as a submarine low-energy explosion that opened a “crater” of 20 by 10 meters wide and 7 meters deep [38, 39].

A huge degassing activity increased the CO₂ flow rate by orders of magnitude: degassing rate estimations carried out

over a 4 km² wide hydrothermal area before the event provided an integrated flow rate in the range of 10⁷ litres/day of CO₂, in contrast with the gas vented only by the crater, estimated to be in the order of 1 – 2 × 10⁹ l/d CO₂. Due to the high solubility of CO₂ in seawater, such a large amount of gas made the surrounding marine environment anoxic killing all the living matter in the area. Moreover, the injection in the atmosphere might form a cloud of about 10⁻³ km³ in the absence of wind.

According to Caliro et al. [38] and Caracausi et al. [40, 41], the unrest episode was caused by a sudden and short-lived input of deep magmatic fluids in the geothermal reservoir. Within a more open view, the 2002 unrest event represents the only submarine hydrothermal explosion observed in the Mediterranean Sea over modern times.

Besides the periodical sample collection (gases and hot waters for laboratory analyses), a continuous monitoring has been carried out by a seafloor observatory developed to perform near real-time data transmission [42]. Among the other sensors, the acoustic probe (hydrophone), installed for a long-term recording of the noise of the bubbling gases in a frequency range of 0.5 Hz⁻³ kHz, gave useful information for a tight tectonic link between the submarine volcanic activity of Panarea island and the crater explosions of the nearby active volcanic island of Stromboli [43].

3.3. Historical Explosive Episodes. Greek and Roman historians from the past, such as Strabo, Titus Livius, Orosius Paulus, Pliny the Elder, and Panaetius (see [44]), widely described violent exhalative events that occurred off the island of Panarea that generated heat, death of fish, and bad smells. Particularly, Strabo told about fire, flames, and ash, which appeared above the sea surface between Hiera (Vulcano island) and Euonymos (Panarea island); this event is dated 126 BC, and the geographic illustration can match the crater area location in between the minor islets in front of Panarea. Mercalli [45] reported jets of hot steam observed by Fouqu e in 1865; this event was concomitant with powerful eruptions of Stromboli and Mount Etna.

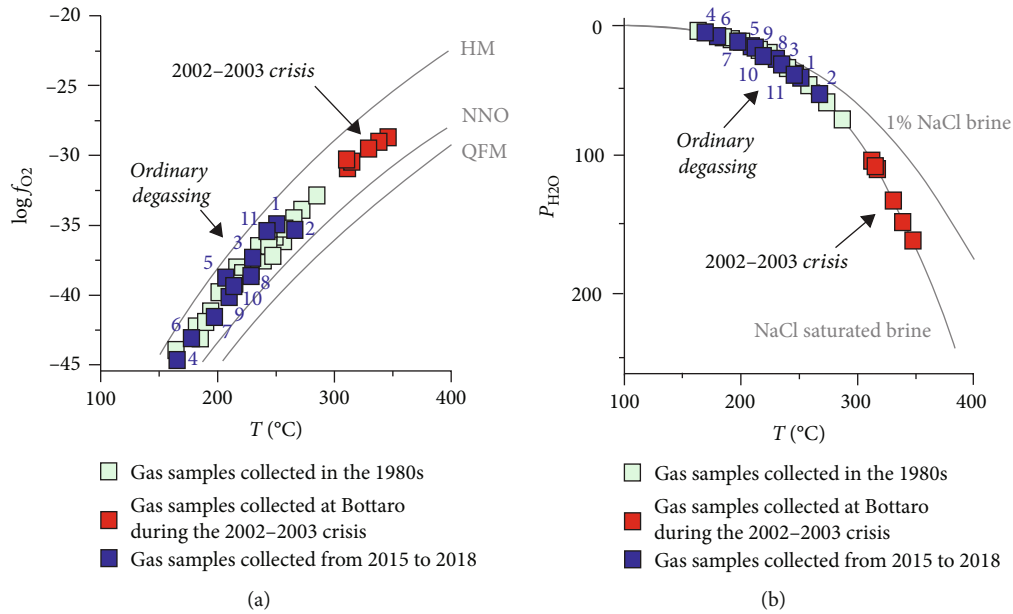


FIGURE 3: Geothermometric and geobarometric estimations (see the text for further details) of the bubbling gases collected at Panarea in the 1980s (data after [17]), during the 2002–2003 volcanic crisis (data after [40]), and from 2015 to 2018 (this paper). (a) Temperature vs. oxygen fugacity (expressed as $\log f_{O_2}$) diagram. The solid buffers quartz-fayalite-magnetite (QFM), nickel-nickel oxide (N-NO), and hematite-magnetite (HM) are plotted as reference (after Eugster and Wones [78]). (b) Estimated equilibrium pressure of the hydrothermal reservoirs. The pressure is shown on the vertical axis as P_{H_2O} (bars). The boiling curves for saturated NaCl and 1% NaCl waters (brines) are shown. P_{H_2O} is calculated by using the estimated equilibrium temperatures.

A similar sequence can be recognized in 2002: the gas burst (November 3) was preceded by a sequence of tectonic events which started with $M = 5.6$ earthquake (6/9/2002 [46]) in the Southern Tyrrhenian Sea and by the onset of the Mount Etna eruption (27/10/2002). A few weeks later (28/12/2002), it was followed by the onset of an intense eruptive phase which started from the flank of Stromboli. According to Walter et al. [47], the earthquake-induced strain may have triggered fluid pressure migration within the active hydrothermal and magmatic systems, generating the Panarea gas burst and the Mount Etna and Stromboli eruptions.

Further indications about the volcanic activity related to the hydrothermal system of Panarea come from geomorphological studies carried out after the crisis (Anzidei et al. [36]; Esposito et al. [48]). The results show how the shallow water platform, located between 0 and -30 m among the islets where the main Panarea hydrothermal area is located, is dotted by a large number of crater-like depressions. More than a hundred of those structures have been recorded, the biggest of them being 175 m wide by 5 m deep. It seems probable that these crater-like structures have been formed by past submarine gas explosions, quite similar to the 2002 event in terms of energy, amount of gas released, and time length; this assumption underlines the fact that this area has been very “hydrothermally” active in recent historical times.

According to Heinicke et al. [43], the seismic, volcanic, and hydrothermal activity of the Panarea volcanic group is controlled by a N40°E normal fault on which Panarea and Stromboli edifices developed. In the Panarea sector, the

N40°E fault and its associated fracture network symbolize the preferential way allowing the hydrothermal fluids to ascend and reach the seafloor; in this environment, a sudden increase of temperature and fluid pressure, in response to changes in the regional stress field, can generate hydrofracturing and rupture [12, 41, 48].

3.4. The Volcanic-Hydrothermal System. Fluids vented at Panarea originate from a reservoir, located at some level beneath the seafloor, kept at the boiling conditions by the thermal energy released by hot magmatic fluids [17, 40]. The results allowed Italiano and Nuccio [17] to model the hydrothermal system composed of several separated geothermal reservoirs fed by hot hydrothermal fluids with a magmatic component. The hot fluids are released by a deep geothermal reservoir ($T > 350^{\circ}C$) constantly recharged by seawater and by magmatic fluids. Inside the deep geothermal reservoir, intense water-rock interactions (WRI) [17] change the original seawater composition by selective extraction of chemical elements from the hosting rocks. During the hydrothermal fluid uprising, the pressure drops inducing boiling and thus phase separation with the production of steam besides high-density liquid phases. Those fluids feed the shallower reservoirs, and the number and intensity of the interactions drive the final geochemical features of the fluids vented at the seafloor.

The chemical composition of the vented hydrothermal fluids is buffered by pressure, temperature, and redox conditions. Following the indications and constrains proposed by Italiano and Nuccio [17], we used the reactive gas

concentrations of CO, CH₄, and CO₂ to estimate the reservoir equilibrium temperatures. Figure 3 shows the results of the performed geothermometric and geobarometric estimations considering the analytical composition of the bubbling gases collected at the main hydrothermal vents over a 30-year long time span including data recorded in the 1980s (after [17]), during the 2002-2003 volcanic crisis (after [40]), and from 2015 to 2018 (this work). We have to take into consideration that the temperature estimations, based on the system H₂O, CO₂, CH₄, and CO, are reasonably valid in the range between 100 and 400°C [17, 49]. The very high CO₂ solubility in seawater during GWI processes, especially in comparison to those of CO and CH₄, provokes severe alterations of the CO₂/CO and CO₂/CH₄ ratios. The slow CO and CH₄ reaction kinetics allows them to retain their abundance ratios keeping the deep equilibrium conditions during their uprising. At the same time, due to their similar solubility coefficients, the CO/CH₄ ratio remains rather constant. The adopted system, however, is more sensitive to the CO and CH₄ contents than that of CO₂; thus, the extent of GWI responsible for the variations of the CO₂ concentration do not influence the estimated equilibrium temperatures (see Italiano and Nuccio's study [17] and Italiano et al.'s study [50] for further details). According to Italiano and Nuccio [17], the equilibrium constants are a function of temperature and oxygen fugacity (f_{O_2}). The latter is buffered by the mineral assemblage (quartz, olivine, magnetite, hematite, and nickel) of the hosting rocks, whereas the temperature influences the water molecule breaking (H₂O = H₂ + (1/2 O₂)). The results have been plotted on the already adopted temperature (f_{O_2} graph) (Figure 3(a)) showing that Panarea samples fall between two theoretical f_{O_2} buffers proving that an equilibrium is attained in every geothermal system. The calculated geotemperatures can also be used to constrain the depth of the geothermal reservoir (Figure 3(b)), by estimating the P_{H_2O} according to the T - P_{H_2O} relationship for 2 M and NaCl-saturated waters ($\log f_{H_2O} = 5.479 - 2047/T$; Chiodini et al. [51]). The estimations show equilibrium temperatures ranging from 150°C to 280°C with P_{H_2O} in the range of 5-70 bars during ordinary degassing (samples collected in the 1980s and from 2015 to 2018). Those values increased up to 350°C and P_{H_2O} ranging between 100 and 160 bars for samples collected at Bottaro during the 2002-2003 crisis. The higher values obtained for the samples collected during the crisis reflect the short rising time due to the high degassing rate that marked the entire crisis time. During the 2002-2003 crisis, the reactive species kept their initial concentrations that had been reached at the reservoir level, bringing the original signature up to seafloor [40].

If a steady state condition is kept at the reservoir level, no significant changes in the geochemical features of the vented hydrothermal fluids are observed with the time, with tides being the main factor acting on the fluid escape. Sudden or wide changes are clear indications that the deep magmatic feeding is not simply related to a cooling magma body, but additional processes (e.g., changes in vertical permeability due to tectonics and fluids from an active magma degassing) have occurred.

4. Hazard Scenarios

Concerning the last eruptive activity of the Panarea volcanic group, several doubts and uncertainties still exist. The most recent papers (e.g., Lucchi et al. [33]) indicate the Drauto pumices (Drauto Formation) as the latest products referred to the Panarea volcanism; no radiometric dating has been carried out, and the age proposed is confined between 24 and 8.7 kyr on the basis of tephrostratigraphic relationships. The Drauto pumices are, in fact, embedded within the Upper Brown Tuffs (fallout eruption units from Vulcano island) which lie above a 27-24 kyr marker bed and below a 8.7-8.4 kyr tephra layer (both markers are external). The Drauto Formation has been interpreted as the result of moderate explosive episodes which originated from a vent situated in the area of the minor islets in light of the geochemical and mineralogical composition and the east-west decrease of thickness and grain size.

During submarine investigations, Bellia et al. [52] and Italiano and Nuccio [17] discovered basic dykes and pillow lavas near the Bottaro islet. The rocks resulted to be deeply altered by the hydrothermal activity precluding any attempt to characterize and dating those products. Their basic composition suggests a totally different age, melt evolution, and emplacement mechanism in comparison to the latest volcanic eruptions located to the East of the main island of Panarea (i.e., Basiluzzo lava dome and Drauto Formation); therefore, we could consider these dykes and pillow lavas as the result of the most recent volcanic event which occurred in this area. Further investigations found out the presence of submerged remnants of probable Roman age [52-56] close to Basiluzzo and Lisca Bianca islets, at a depth of 3-14 meters. This localized subsidence can be related to a magma chamber deflation or to the extensional neotectonic activity. Both scenarios might have been connected with volcanic eruptions.

The explosions associated with the observed craters at the main hydrothermal field have involved the sediment cover formed during the seawater rise following the Wurmian lowstand [48]; hence, they must be younger than 10,000 years at least. Considering the presence of ~150 craters within the area of the minor islets, the average probability of the occurrence of hydrothermal explosions was calculated by Monecke et al. [20] as to be one event per ~65-70 years. As a matter of fact, explosive events, such as the 2002 unrest episode, have to be considered common phenomena, and therefore, the occurrence of an explosive gas eruption cannot be ruled out.

Taking into account the above-mentioned considerations, constraints, and speculations from previous and historical works about volcanism, we hypothesize and describe three distinct hazard scenarios for the area (Table 2): (i) ordinary hydrothermal venting activity; (ii) occurrence of a gas burst; and (iii) occurrence of a volcanic eruption (Drauto-type). Our scenarios are also supported by the multidisciplinary data showing the close link between hydrothermalism, volcanic, and geodynamic processes affecting the Panarea volcanic group.

4.1. Scenario 1: Ordinary Hydrothermal Venting. The potential geohazard associated to the normal discharge activity are

TABLE 2: Hazard scenarios connected to Panarea activity.

Hazard scenario	(1) Ordinary venting	(2) Gas burst	(3) Eruption (Drauto-type)
<i>Probability of occurrence</i>	Permanent.	High.	Low.
<i>Recurrence interval</i>	Permanent.	One event per 65/70 years [20].	Unknown.
<i>Hazard</i>	Low.	High.	Very high.
<i>Extremely dangerous phenomena</i>	Constant release of CO ₂ and H ₂ S-rich gases.	Poisonous gas clouds (toxic clouds); tsunamis.	Intermittent eruptive columns; tephra fallout; pyroclastic density currents; toxic clouds; tsunamis.
<i>Mitigation measurements</i>	Near real-time monitoring of CO ₂ and H ₂ S concentrations in the seawater surface/atmosphere.	Evacuation of Panarea villages located downwind to the gas burst area; interdiction of tourist activity and marine navigation in the gas burst area; near real-time monitoring of the gas output and CO ₂ and H ₂ S concentrations.	Evacuation of the whole Panarea island and the coasts of the surrounding Aeolian Islands; interdiction of marine navigation and tourist activity.

mainly centered on the role of hydrothermal fluids constantly released by the submarine vents. In this situation, bubbling gases can be totally or partially dissolved in seawater during their rise through the water column as a function of their mass ratio. The possibility that deep-originated gases reach the atmosphere depends on the gas emission rate, the depth, the bubble size, the time length, and the intensity of the interactions between bubbling gases and marine waters along the seawater column. When the amount of gas vented at the seafloor increases, a larger gas fraction could reach the sea surface and interact with the lower atmosphere. This occurrence could be very hazardous to the human health, especially under certain weather conditions such as low atmospheric pressure and no wind. Those conditions may easily occur in summer during the tourist season when Panarea hosts thousands of people in land and a huge number of luxury boats in between the main island and the islets.

The bubbling gases from submarine vents are mainly composed of CO₂ and H₂S, and their dangerous (and sometimes lethal) effects are controlled by two factors: their concentrations and the exposure times.

Carbon dioxide (CO₂) is an odorless and colorless gas with higher density than the dry air; it is commonly defined as a “killer gas,” and in the atmosphere, its content is around 400 ppm. In case of the wind absence and a continuous gas injection from the seafloor to the atmosphere, the CO₂ could accumulate just over the sea surface forcing the generation of air volumes depleted in O₂ and enriched in CO₂. This hazardous situation could be responsible for the following: (i) asphyxia phenomena that usually appear when the O₂ concentration is <16 vol. % and O₂ concentration of 13-10 vol. % that could induce unconsciousness and death [57] and (ii) exposure to low-level CO₂ concentration (<4 vol. %) that could produce different short-term effects such as weakness, headache, and cough and CO₂ concentration above 4 vol. % that has been defined by Rice [58] as the *IDHL* (immediately dangerous to life/health) causing an immediate risk for the human health and life.

Hydrogen sulfide (H₂S) is acutely toxic and colorless, and at low concentration, it is well known for the traditional “rotten egg” smell. The H₂S may cause severe health

troubles under prolonged exposures [59]. It becomes very harmful in case of long-term exposure at concentration levels of 1 ppm: it could provoke weakness, headache, and neurological diseases. At high concentrations, in the range of 200-250 ppm, it can trigger some respiratory system diseases and death whereas at 1,000 ppm it is lethal.

4.2. Scenario 2: Gas Burst-Type Event. The results of recent geophysical investigations [48] remarked how the gas explosions are common phenomena over the submarine Panarea hydrothermal area; thus, trying to analyze the possible evolution of a gas burst event in terms of intensity, features, damages, and short-term effects has become a critical goal. According to Monecke et al. [20], the average probability of the occurrence of gas bursts is around one event per 65/70 years; this result was obtained assuming that all the ~150 craters detected at the seafloor formed after the end of the glacial era, thus over the last ~10 kyr. Unluckily, a valid and reliable value cannot be calculated because too many undefined factors are in play. Evaluating the onset time of crater formation is not possible; the sediment cover reworked during hydrothermal explosions represents the unique temporal marker applicable in this context. These sediments are referred to the seawater rise associated to the last lowstand, and therefore, 10 kyr represents the oldest available time for the onset. Additionally, the fastest phase of sea level rise ended ~7 kyr [60] and we have no clear evidence that the top of the sediment cover is confined at ~10 kyr. Moreover, new craters could be superimposed over the older ones, or a single crater might have been involved by more than one gas burst. For those reasons, one event per 65/70 years could be considerably underestimated. We cannot also ignore the evidence that gas burst episodes are controlled by faults (e.g., [43]), and it is extremely plausible that since 10-7 kyr the occurrence probability has changed many times in response to changes in the tectonic activity. As a matter of fact, the current probability results to be unknown. This hypothesis is corroborated by the fact that several changes in the eruption style and in magma composition affected Stromboli during the last 15-13 ka (see Francalanci et al.’s study [7] and the references therein). These features, together with

the multistage genesis of the Sciara del Fuoco depression, indicate that the recent volcanic evolution of Stromboli has been driven by the occurrence of tectonic pulses over the same tectonic structure in which also Panarea island developed.

We have to consider that the intensity of gas bursts can be variable and unpredictable, as testified by different shapes and extension of the craters. The released energy generally depends on the amount of the magmatic fluids injected into the geothermal reservoir at depth; for example, the energy estimate carried out for the 2002 gas burst episode was 1.3×10^8 J [41] and the volume of removed sediments resulted around 3×10^3 m³ [48]. The maximum potential energy that can be released as a consequence of a gas explosion caused by a 2002-like mechanism was roughly calculated by Caracausi et al. [41] in the order of 10^9 J.

The features expected for this scenario are the same with those observed during the burst which occurred in 2002, with changes in the geochemical composition of hydrothermal fluids, decrease of seawater pH, total gas output enhancement along with the reworking of rocks and sediments, the death of fish, and sulfurous smell. The anomalous high gas output from seafloor (orders of magnitude higher than the ordinary degassing) drives the formation of extremely dangerous and lethal gas clouds (mostly CO₂ and H₂S) in the atmosphere just above the venting zone. Toxic clouds are the main hazardous effects correlated with this event because they can be moved by wind and reach the Panarea village, boats at the anchor, or the other islands located even several kilometers away from the venting field causing diseases or death to exposed people. A similar condition occurred during the 1650 Kolumbo submarine eruption that caused clouds of poisonous gases which reached the adjacent Santorini island ([61, 62] and references therein). All of these aspects (i.e., CO₂ and H₂S released and volume of toxic clouds and of reworked sediments) could have different impacts as a consequence of the gas burst energy.

Prevention activities in order to mitigate the potential risks of this area, mainly during summertime, consist in the evacuation of the downwind villages to the respect of the gas venting zone, with the interdiction of the entire degassing area to tourists and navigation.

An exceptionally powerful explosion could also induce submarine ruptures, collapses, and landslides with a tsunamigenic potential. According to Caracausi et al. [41], tsunamis might be triggered if the energy (and consequently the amount of volatiles involved in the gas explosion) is at least two orders of magnitude higher than that estimated for the 2002 event.

4.3. Scenario 3: Volcanic Eruption (Drauto-Type) Event.

Panarea island has long been considered by local people (and scientific community as well) an extinct volcano. Italiano and Nuccio, in 1991, first proposed that the island was an active volcano based on the energy estimations related to the gas output. The most recent information and events highlight how Panarea volcanism is still active and potentially dangerous. The presence of magmatic bodies beneath the Panarea area is supported by the geochemical informa-

tion coming from the bubbling gases showing $\delta^{13}\text{C}_{\text{CO}_2}$ values and $^3\text{He}/^4\text{He}$ ratios in the same range of those recorded at the active volcano of Stromboli. As a matter of fact, it cannot be excluded that there is a possibility that a volcanic eruption might take place in the future in agreement with Lucchi et al. [33] who pointed out that the occurrence of an explosive eruption similar to that which produced the Drauto Formation cannot be ruled out. The scientific community has interpreted the Drauto pumices as the formation which recorded the latest eruptive event(s) of Panarea; moreover, considering that no absolute evidence has been identified against it, we decided to adopt the “Drauto-type event” as the plausible scenario connected to a volcanic eruption.

The Drauto eruptions, according to Lucchi et al. [33], is composed of two distinct fallout units, probably generated from a proximal source area in the Panarea volcanic group, with a rapid east-west decrease of thickness from about 25 cm at Basiluzzo to 20 cm at Drauto, to less than 10 cm at Castello di Salvamento. According to Lucchi et al. [33], these fallout units were emitted from a vent located in the area of the minor islets and presently completely eroded and submerged. This provenance is supported by the high-K to SHO affinity (high-K andesite-dacite to latite) and the distinctive biotite-amphibole mineralogic content of the Drauto pumices, which are comparable to some volcanic products of the Lisca Bianca and Bottaro islets [63].

The Drauto-type volcanic activity can be expressed by moderate fallout eruptions from intermittent volcanian-type eruptive columns comparable to those which generated the Soldata pumices (Eruptive Epoch 2 of Panarea [33]). The volume of magma involved in a possible Drauto-type eruption could be similar to the values estimated from Drauto and Soldata pumices events (1.5×10^7 m³ and 2.3×10^7 m³, respectively, [33]); obviously, this assumption is purely indicative as the amount of magma emitted during volcanic eruptions depends on various aspects. This eruptive style can generate several dangerous phenomena such as toxic clouds and dilute wet-type pyroclastic density currents (PDCs); however, tephra fallout from the explosive eruptive columns is surely the most significant outcome. The fallout intensity reflects the combined effect of wind variability, column height, duration, and total erupted mass. The tephra fallout hazard assessment has recently caught the attention of some researchers [64–69], who assumed a few representative eruptive scenarios for the Phlegrean Fields and Somma-Vesuvius areas where over three million of people are perilously exposed.

The combination of different data allowed to explain the 2002 gas burst of Panarea and the following eruption at Stromboli as the result of hot fluids and magma migration through tectonic lines caused by reactivation of geodynamic structures [43]. We can infer that volcanic activity in this zone is totally controlled by the WNW-ESE extensional deformation affecting the eastern sector of the Aeolian Islands. The magmatic source sampled intermittently by the Panarea volcanism seems to be extinct, but even small movements along normal faults may cause an abrupt permeability increase which could induce hot magma rise even from zones far away from the Panarea edifice; this means

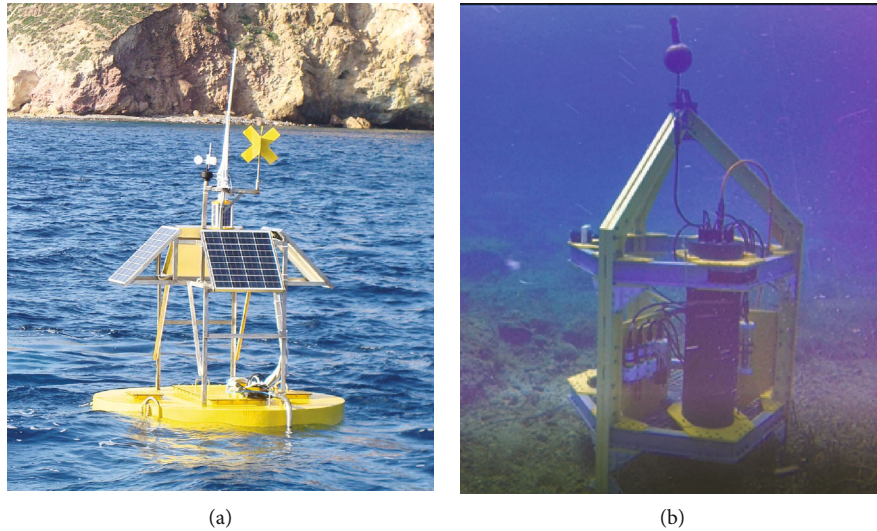


FIGURE 4: The multidisciplinary monitoring system operating within the main hydrothermal field offshore Panarea: (a) surface buoy and (b) seafloor observatory.

that the occurrence of volcanic eruptions within the Panarea area is closely addicted to the normal faulting activity. Extensional tectonics, Stromboli volcanism, and Panarea activity compose a unique geodynamic system, which can activate an enormous amount of energy; consequently, a hypothetical eruptive episode could be accompanied by tsunami waves. Among the *tsunamigenic mechanisms*, we can account (i) earthquakes associated to NE-SW normal faults; (ii) eruptive pulses in the minor islet area (the energy released in case of phreatomagmatic explosions can reach 10^{17} - 10^{18} J [70, 71]); and (iii) landslides along the Stromboli cone due to earthquakes, effusive lateral eruption, and paroxysmal activity.

Regarding this scenario, it is worth noting that in view of the strong link between volcanism and tectonics, a combined approach which considers both the seafloor monitoring observatory [42] and the seismicity is largely the best way to follow in order to provide valid answers about the state and possible changes of the Panarea volcanic-hydrothermal system. In the context of managing natural hazards, prevention measurements to minimize the potential volcanic risk are the evacuation of Panarea island and the interdiction of tourist activities and marine navigation around the island and its surroundings. However, we consider the probability of occurrence of a Drauto-type eruption as extremely low.

5. The Multidisciplinary Submarine Monitoring Activity

A common way to minimize any natural or industrial hazard is to develop a correct monitoring activity of the main hazard factors. The monitoring activity in Panarea has been carried out following a periodical sampling of submarine vents (including bubbling gases and thermal waters) and using data from a continuous monitoring provided by an automatic system (Figure 4) made of a seafloor observatory connected by cable to a surface buoy [42]. The multidisciplinary

submarine observatory has been recently upgraded (see Italiano et al.'s study [72] and Caruso et al.'s study [73]) with the addition of a new set of sensors including a hydrophone and probes for dissolved CO_2 , pH, and electric conductivity. Moreover, 4 temperature probes monitor the temperature at the hottest vent and in three different thermal water emissions at the seafloor around the observatory. An example of data series recorded from the seafloor observatory is reported in Figure 5.

The acoustic records are considered the proxy of the degassing activity and may provide information on sudden changes not related to natural forces: tides, waves, etc. As already observed by Heinicke et al. [43], the hydrothermal fluids vented at the hydrothermal area of Panarea have shown changes related to the volcanic activity of the nearby Stromboli island. A continuous monitoring associated to the geochemical features of the vented gases (including helium and carbon isotopic compositions) may provide important and early information on changes occurring at the submarine vents. Enhancing the surveillance system by the monitoring of CO_2 and H_2S concentrations in air at the seawater interface could represent the key for success against the gas hazard related to the ordinary degassing activity, mainly at the tourist attractions in the Panarea island and its surrounding islets. Recently, many improvements have been made about the understanding of the submarine hydrothermal system of Panarea, and the near real-time monitoring of the hot fluids vented from thermal areas allows detecting variations and changes within the volcanic-hydrothermal reservoirs. Changes in CO_2 concentration, increase in the temperature, and pH decrease of the vented fluids could represent the initial condition for an enhancement of magmatic volatiles supply. Those geochemical anomalies might be associated to the rising of deep, hot magmatic fluids, and in some cases, they could be responsible for the reactivation of the Panarea volcanic system, triggering a potential and dangerous submarine gas explosion. No evident geophysical changes preceded the 2002 submarine explosion, and GPS data demonstrated

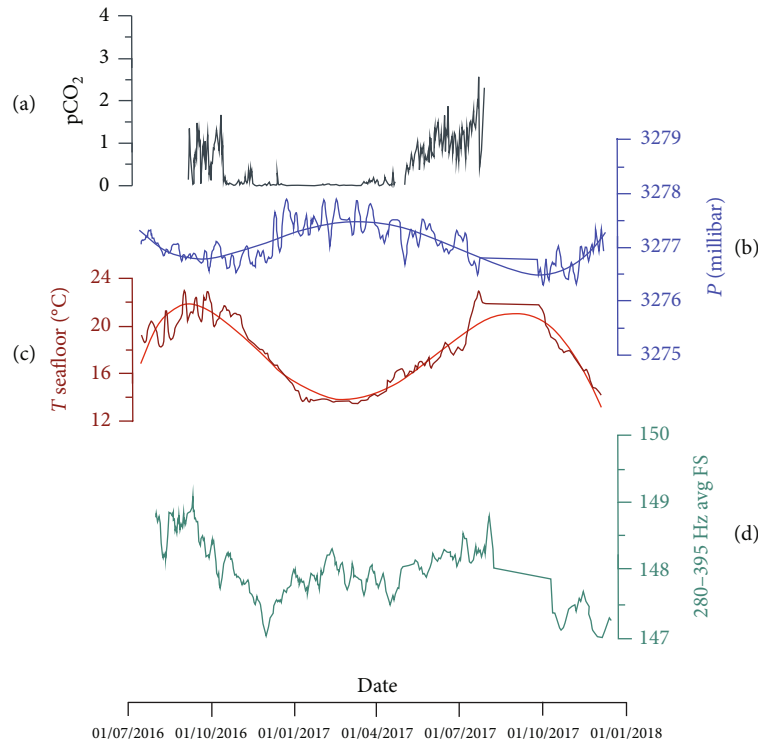


FIGURE 5: Example of long data series acquired by the multidisciplinary observatory: (a) percentage of dissolved CO_2 ; (b) seafloor hydrostatic pressure together with the 3rd order polynomial line highlighting its seasonality; (c) seafloor temperature (dark-red line) together with the 3rd order polynomial (light-red line) highlighting its seasonality; and (d) passive acoustic record RMS modulation over the range 280–395 Hz (associated to bubble stream cluster acoustic source), representing how sound pressure intensity changes over time. Acoustic series was further filtered by seasonality induced by environmental parameters.

that no significant differences in the subsidence rate had been observed before November 2002 [12]. Geochemical anomalies seem to be the most reliable resource to precociously identify changes of the Panarea volcanic system. Ordinary venting (Scenario 1) represents the permanent activity of the geothermal system of Panarea. Therefore, the values registered by the multidisciplinary observatory during the steady-state condition correspond to the threshold values to take into consideration in order to detect, and maybe anticipate, any unrest of the volcanic/hydrothermal activity as a consequence of deep inputs of thermal energy at the level of the geothermal reservoir. Taking into account the model proposed for the Panarea hydrothermal system by Italiano and Nuccio [17], the deep energy input can be transferred to shallower geothermal systems increasing their temperature and enhancing the gas output. We do not expect a gas output increase all over the submarine hydrothermal system, but only localized changes in the gas flow rates, even associated to increases of the thermal water temperature. Among the parameters automatically monitored by the seafloor observatory, the dissolved CO_2 , pH, and acoustic data are probably the most prone to undergo severe modification during the establishment of Scenario 2 (gas burst event) as well as the temperature of the thermal waters measured at the emission point. Moreover, since the hydroacoustic noise is associated to the bubbling activity, every change of the gas flow rate (namely, change of the total gas output) is expressed by frequency shifts and increases in terms of energy (decibels) of

the signal. The increase of dissolved pCO_2 and the consequent drop of pH due to the gas flow rate enhancement can be recorded besides an increase of the magmatic component with respect to the hydrothermal one revealed by the laboratory analysis of the bubbling gases periodically taken at the seafloor. Although we might not be able to appreciate a significant increase of the outlet temperature measured by the seafloor observatory before or during a gas burst episode, the equilibrium temperatures of the fluids inside the reservoir will change a lot as it occurred during the 2002–2003 crisis when the estimated equilibrium temperatures were at least 25% higher than those calculated for the ordinary degassing (1980s and 2015–2018 data). For the above-mentioned reasons, we want to stress that the correct strategy to approach the evaluation of the hydrothermal hazard is to couple the continuous monitoring activity with periodical sampling and measurements of the vented fluids.

In the volcanic eruption case (Scenario 3), we expect severe changes in the dissolved pCO_2 , pH, temperature, and acoustic signals due to a larger thermal energy input with respect to Scenario 2. Periodical measurements of the isotopic composition of helium in the vented fluids are very helpful to identify possible undegassed magma batches intruding underneath the deep geothermal system.

We propose that a local network of multidisciplinary seafloor monitoring observatories, as described by Italiano et al. [42], with continuous data recording and transmission, could represent the best monitoring tool in submarine volcanic

environments, able to catch changes in the chemical and physical conditions of the hydrothermal fluids over a wide submarine area.

6. Conclusions

This work represents a preliminary study on the submarine volcanic-hydrothermal hazard assessment connected to the Panarea activity. Since the 2002 gas burst, this kind of hazard began to be perceived and analyzed with more care [74, 75], but a lot of work is still needed to be done. In this paper, three different hazard scenarios have been described with the aim of giving useful information for scientific as well as possible civil protection purposes. For the risk assessment, we have to take into account that Panarea island counts, in the winter period, less than 250 inhabitants, most of them fishermen, and no marine activities, are carried out over the area between the volcanic islands of Panarea and Stromboli. Contrastingly, during the summer season, Panarea island hosts a number of inhabitants and an order of magnitude higher than in winter, and, moreover, the area off the east coast of the island, where most of the hydrothermal vents are located, becomes a tourist attraction with hundreds of vessels per day moving over the area. In this framework, evaluating the hazard scenarios results in a key point for a correct risk assessment.

It has been observed that explosive hydrothermal episodes are driven by gas migration from deep magma source and are probably controlled by fault activity; then, we argue that geodynamic processes assume a dominant role in this area influencing the magmatic behavior of the whole eastern Aeolian sector. Changes of geochemical parameters induced by a deep gas input are crucial factors for the deep system overpressure, which could lead to the rupture and to the genesis of a potential gas explosion, favored in many cases by the extensional tectonics at a regional/local scale.

Hazard associated with submarine hydrothermalism represents a new type of challenge concerning the implementation of risk mitigation actions. Continuous monitoring of the seismic activity, gas fluxes, and geochemical parameters is the best way to deal with this significant issue in order to improve our knowledge about any submarine hydrothermal system at a global scale for which Panarea may represent a reference.

Data Availability

The data used to support the findings of this study are included within the article. In order to strengthen our assumptions, we used some geochemical data from previously reported studies which have been cited.

Conflicts of Interest

The authors declare that there are no conflicts of interest regarding the publication of this paper.

Acknowledgments

The authors wish to thank the Regional Department of Civil Protection of Sicily for the financial support. The cooperation between the Italian Civil Protection Agency, Regional Department of Civil Protection of Sicily, and National Institute of Geophysics and Volcanology has been officially determined by the Accordo Quadro DPC-INGV 2012-2021 and the DDG 30-12-2016 n.1840 agreements, respectively. The authors are also grateful to Francesco Salerno, Mariano Tantillo, Aldo Sollami, and Ygor Oliveri for their support in the laboratory work.

References

- [1] G. De Astis, G. Ventura, and G. Vilardo, "Geodynamic significance of the Aeolian volcanism (Southern Tyrrhenian Sea, Italy) in light of structural, seismological and geochemical data," *Tectonics*, vol. 22, no. 4, article 1040, 2003.
- [2] A. Rovida, M. Locati, R. Camassi, B. Lolli, and P. Gasperini, Eds., *CPT115, the 2015 version of the Parametric Catalogue of Italian Earthquakes*, INGV, 2016.
- [3] F. Cultrera, G. Barreca, P. Burrato et al., "Active faulting and continental slope instability in the Gulf of Patti (Tyrrhenian side of NE Sicily, Italy): a field, marine and seismological joint analysis," *Natural Hazards*, vol. 86, Supplement 2, pp. 253–272, 2017.
- [4] S. Tinti, E. Bortolucci, and A. Armigliato, "Numerical simulation of the landslide-induced tsunamis of 1988 on Vulcano Island, Italy," *Bulletin of Volcanology*, vol. 61, no. 1–2, pp. 121–137, 1999.
- [5] G. Mercalli and O. Silvestri, "Le eruzioni dell'isola di Vulcano incominciate il 3 Agosto 1888 e terminate il 22 Marzo 1890. Relazione scientifica," *Annali Ufficiali del Centenario Meteorologico e Geodinamico*, vol. 10, no. 4, pp. 1–216, 1891.
- [6] G. De Astis, F. Lucchi, P. Dellino et al., "Geology, volcanic history and petrology of Vulcano (central Aeolian archipelago)," in *The Aeolian Islands Volcanoes*, F. Lucchi, A. Peccerillo, J. Keller, C. A. Tranne, and P. L. Rossi, Eds., no. 37pp. 281–349, Geological Society Memoir, 2013.
- [7] L. Francalanci, F. Lucchi, J. Keller, G. De Astis, and C. A. Tranne, "Eruptive, volcano-tectonic and magmatic history of the Stromboli volcano group (north-eastern Aeolian archipelago)," in *The Aeolian Islands Volcanoes*, F. Lucchi, A. Peccerillo, J. Keller, C. A. Tranne, and P. L. Rossi, Eds., no. 37pp. 397–471, Geological Society Memoir, 2013.
- [8] A. Bonaccorso, S. Calvari, G. Garfi, L. Lodato, and D. Patanè, "Dynamics of the December 2002 flank failure and tsunami at Stromboli volcano inferred by volcanological and geophysical observations," *Geophysical Research Letters*, vol. 30, no. 18, pp. 1941–1944, 2003.
- [9] M. Pistolesi, D. Delle Donne, L. Pioli, M. Rosi, and M. Ripepe, "The 15 March 2007 explosive crisis at Stromboli volcano, Italy: assessing physical parameters through a multidisciplinary approach," *Journal of Geophysical Research*, vol. 116, no. B12, article B12206, 2011.
- [10] M. Rosi, M. Pistolesi, A. Bertagnini, P. Landi, M. Pompilio, and A. Di Roberto, "Stromboli volcano, Aeolian Islands (Italy): present eruptive activity and hazards," in *The Aeolian Islands Volcanoes*, F. Lucchi, A. Peccerillo, J. Keller, C. A. Tranne,

- and P. L. Rossi, Eds., no. 37pp. 473–490, Geological Society Memoir, 2013.
- [11] M. L. Carapezza, F. Barberi, M. Ranaldi et al., “Diffuse CO₂ soil degassing and CO₂ and H₂S concentrations in air and related hazards at Vulcano Island (Aeolian arc, Italy),” *Journal of Volcanology and Geothermal Research*, vol. 207, no. 3–4, pp. 130–144, 2011.
- [12] A. Esposito, M. Anzidei, S. Atzori, R. Devoti, G. Giordano, and G. Pietrantonio, “Modeling ground deformations of Panarea volcano hydrothermal/geothermal system (Aeolian Islands, Italy) from GPS data,” *Bulletin of Volcanology*, vol. 72, no. 5, pp. 609–621, 2010.
- [13] V. Esposito, F. Andaloro, S. Canese et al., “Exceptional discovery of a shallow-water hydrothermal site in the SW area of Basiluzzo islet (Aeolian archipelago, South Tyrrhenian Sea): An environment to preserve,” *PLoS ONE*, vol. 13, no. 1, article e0190710, 2018.
- [14] J. Lupton, C. de Ronde, M. Sprovieri et al., “Active hydrothermal discharge on the submarine Aeolian Arc,” *Journal of Geophysical Research*, vol. 116, no. B2, article B02102, 2011.
- [15] S. L. Walker, S. Carey, K. L. Bell et al., “Near-bottom water column anomalies associated with active hydrothermal venting at Aeolian arc volcanoes, Tyrrhenian Sea, Italy,” in *Paper presented at AGU Fall Meeting Abstracts*, San Francisco, CA, USA, 2012.
- [16] F. Italiano, A. de Santis, P. Favali, M. Rainone, S. Rusi, and P. Signanini, “The Marsili volcanic seamount (southern Tyrrhenian Sea): a potential offshore geothermal resource,” *Energies*, vol. 7, no. 7, pp. 4068–4086, 2014.
- [17] F. Italiano and P. M. Nuccio, “Geochemical investigations of submarine volcanic exhalations to the east of Panarea, Aeolian Islands, Italy,” *Journal of Volcanology and Geothermal Research*, vol. 46, no. 1–2, pp. 125–141, 1991.
- [18] F. Italiano, “Hydrothermal fluids vented at shallow depths at the Aeolian islands: relationships with volcanic and geothermal systems,” *FOG Freiberg Online Geology*, vol. 22, pp. 55–60, 2009.
- [19] T. L. Maugeri, G. Bianconi, F. Canganella et al., “Shallow hydrothermal vents in the southern Tyrrhenian Sea,” *Chemistry and Ecology*, vol. 26, Supplement 1, pp. 285–298, 2010.
- [20] T. Monecke, S. Petersen, M. D. Hannington et al., “Explosion craters associated with shallow submarine gas venting off Panarea island, Italy,” *Bulletin of Volcanology*, vol. 74, no. 9, pp. 1937–1944, 2012.
- [21] S. Graziani, S. E. Beaubien, S. Bigi, and S. Lombardi, “Spatial and temporal pCO₂ marine monitoring near Panarea Island (Italy) using multiple low-cost GasPro sensors,” *Environmental Science and Technology*, vol. 48, no. 20, pp. 12126–12133, 2014.
- [22] M. F. Loreto, F. Pepe, R. De Ritis et al., “On the relationships between tectonics and volcanism in the offshore capo Vaticano, SE Tyrrhenian Sea, during the Plio-Pleistocene,” *Rendiconti Online Società Geologica Italiana*, vol. 31, no. 1, pp. 85–98, 2014.
- [23] M. F. Loreto, F. Italiano, D. Deponte, L. Facchin, and F. Zgur, “Mantle degassing on a near shore volcano, SE Tyrrhenian Sea,” *Terra Nova*, vol. 27, no. 3, pp. 195–205, 2015.
- [24] S. Passaro, S. Genovese, M. Sacchi et al., “First hydroacoustic evidence of marine, active fluid vents in the Naples Bay continental shelf (Southern Italy),” *Journal of Volcanology and Geothermal Research*, vol. 285, pp. 29–35, 2014.
- [25] S. Passaro, S. Tamburrino, M. Vallefucio et al., “Seafloor doming driven by degassing processes unveils sprouting volcanism in coastal areas,” *Scientific Reports*, vol. 6, no. 1, article 22448, 2016.
- [26] M. Ingrassia, E. Martorelli, A. Bosman, L. Macelloni, A. Sposato, and F. L. Chiocci, “The Zannone Giant Pockmark: first evidence of a giant complex seeping structure in shallow-water, central Mediterranean Sea, Italy,” *Marine Geology*, vol. 363, pp. 38–51, 2015.
- [27] F. Italiano, D. Romano, C. Caruso, M. Longo, A. Corbo, and G. Lazzaro, “Magmatic signature in submarine hydrothermal fluids vented offshore Ventotene and Zannone Islands (Pontine Archipelago, Central Italy),” *Geofluids*, vol. 2019, Article ID 8759609, 15 pages, 2019.
- [28] L. Beccaluva, G. Gabbianelli, F. Lucchini, P. L. Rossi, and C. Savelli, “Petrology and K/Ar ages of volcanics dredged from the Eolian seamounts: implications for geodynamic evolution of the southern Tyrrhenian basin,” *Earth and Planetary Science Letters*, vol. 74, no. 2–3, pp. 187–208, 1985.
- [29] M. Di Bella, F. Italiano, G. Sabatino et al., “Pleistocene volcanoclastic units from North-Eastern Sicily (Italy): new evidence for calc-alkaline explosive volcanism in the Southern Tyrrhenian Sea,” *Geologica Carpathica*, vol. 67, no. 4, pp. 371–389, 2016.
- [30] E. Leocat, *Histoire eruptive des volcans du secteur occidental des Iles Eoliennes (Sud de la Mer Tyrrhenienne, Italie) et evolution temporelle du magmatisme*, Unpublished PhD thesis, University of Paris 11 Orsay, France, 2011.
- [31] E. Leocat, P. Y. Gillot, and A. Peccerillo, “Temporal evolution of the western and central volcanism of the Aeolian Island Arc (Italy, southern Tyrrhenian Sea),” in *Paper presented at EGU General Assembly, Geophysical Research Abstracts*, vol. 11, Vienna, Austria, 2009.
- [32] E. Leocat, P. Y. Gillot, and A. Peccerillo, “Eruptive history of western and central Aeolian volcanoes (South Tyrrhenian Sea): insights from K/Ar dating,” in *44th Annual conference of the Volcanic and Magmatic Studies Group (VMSG)*, Geological Society of London and Mineralogical Society, Abstract Volume, 2010.
- [33] F. Lucchi, C. A. Tranne, A. Peccerillo, J. Keller, and P. L. Rossi, “Geological history of the Panarea volcanic group (eastern Aeolian archipelago),” in *The Aeolian Islands Volcanoes*, F. Lucchi, A. Peccerillo, J. Keller, C. A. Tranne, and P. L. Rossi, Eds., no. 37pp. 3–11, Geological Society Memoir, 2013.
- [34] G. Gabbianelli, C. Romagnoli, P. L. Rossi, and N. Calanchi, “Marine geology of the Panarea-Stromboli area (Aeolian Archipelago, Southeastern Tyrrhenian Sea),” *Acta Vulcanologica*, vol. 3, pp. 11–20, 1993.
- [35] P. L. Rossi, G. Bocchi, N. Calanchi, G. Lanzafame, F. Lucchini, and R. Romano, “Evoluzione vulcano-tettonica e geochimica dell’apparato di Panarea (Isole Eolie),” *Rendiconti Società Italiana di Mineralogia e Petrografia*, vol. 41, no. 1, pp. 144–145, 1986.
- [36] M. Anzidei, A. Esposito, G. Bortoluzzi, and F. De Giosa, “The high resolution bathymetric map of the exhalative area of Panarea Aeolian islands, Italy,” *Annals of Geophysics*, vol. 48, no. 6, pp. 899–921, 2005.
- [37] F. Gamberi, M. Marani, and C. Savelli, “Tectonic, volcanic and hydrothermal features of a submarine portion of the Aeolian arc (Tyrrhenian Sea),” *Marine Geology*, vol. 140, no. 1–2, pp. 167–181, 1997.

- [38] S. Caliro, A. Caracausi, G. Chiodini et al., "Evidence of a recent input of magmatic gases into the quiescent volcanic edifice of Panarea, Aeolian Islands, Italy," *Geophysical Research Letters*, vol. 31, no. 7, article L07619, 2004.
- [39] B. Capaccioni, F. Tassi, O. Vaselli, D. Tedesco, and R. Poreda, "Submarine gas burst at Panarea Island (southern Italy) on 3 November 2002: A magmatic versus hydrothermal episode," *Journal of Geophysical Research*, vol. 112, no. B5, article B05201, 2007.
- [40] A. Caracausi, M. Ditta, F. Italiano et al., "Changes in fluid geochemistry and physico-chemical conditions of geothermal systems caused by magmatic input: The recent abrupt outgassing off the island of Panarea (Aeolian Islands, Italy)," *Geochimica et Cosmochimica Acta*, vol. 69, no. 12, pp. 3045–3059, 2005.
- [41] A. Caracausi, M. Ditta, F. Italiano, M. Longo, P. M. Nuccio, and A. Paonita, "Massive submarine gas output during the volcanic unrest off Panarea Island (Aeolian arc, Italy): inferences for explosive conditions," *Geochemical Journal*, vol. 39, no. 5, pp. 459–467, 2005.
- [42] F. Italiano, R. Maugeri, A. Mastrolia, and J. Heinicke, "SMM, a new seafloor monitoring module for real-time data transmission: an application to shallow hydrothermal vents," *Procedia Earth and Planetary Science*, vol. 4, pp. 93–98, 2011.
- [43] J. Heinicke, F. Italiano, R. Maugeri et al., "Evidence of tectonic control on active arc volcanism: the Panarea-Stromboli tectonic link inferred by submarine hydrothermal vents monitoring (Aeolian arc, Italy)," *Geophysical Research Letters*, vol. 36, no. 4, article L04301, 2009.
- [44] Storia Geofisica Ambientale, *Fenomeni vulcanici nell'arcipelago delle Eolie dall'antichità al XX secolo*, vol. 156, Studio di fattibilità RPT, Bologna, Italy, 1996.
- [45] G. Mercalli, "Vulcani e fenomeni Vulcanici," in *Geologia d'Italia*, G. Negri, A. Stoppani, and G. Mercalli (Milano), Eds., p. 374, F. Vallardi, Milan, Italy, 1883.
- [46] R. Azzaro, M. S. Barbano, R. Camassi et al., "The earthquake of 6 September 2002 and the seismic history of Palermo (northern Sicily, Italy): implications for the seismic hazard assessment of the city," *Journal of Seismology*, vol. 8, no. 4, pp. 525–543, 2004.
- [47] T. R. Walter, R. Wang, V. Acocella, M. Neri, H. Gresser, and J. Zschau, "Simultaneous magma and gas eruptions at three volcanoes in southern Italy: an earthquake trigger?," *Geology*, vol. 37, no. 3, pp. 251–254, 2009.
- [48] A. Esposito, G. Giordano, and M. Anzidei, "The 2002–2003 submarine gas eruption at Panarea volcano Aeolian Islands, Italy: volcanology of the seafloor and implications for the hazard scenario," *Marine Geology*, vol. 227, no. 1–2, pp. 119–134, 2006.
- [49] W. F. Giggenbach, "Redox processes governing the chemistry of fumarolic gas discharges from White Island, New Zealand," *Applied Geochemistry*, vol. 2, no. 2, pp. 143–161, 1987.
- [50] F. Italiano, A. Sasmaz, G. Yuce, and O. O. Okan, "Thermal fluids along the East Anatolian Fault Zone (EAFZ): geochemical features and relationships with the tectonic setting," *Chemical Geology*, vol. 339, pp. 103–114, 2013.
- [51] G. Chiodini, L. Marini, and M. Russo, "Geochemical evidence for the existence of high-temperature hydrothermal brines at Vesuvio volcano, Italy," *Geochimica et Cosmochimica Acta*, vol. 65, no. 13, pp. 2129–2147, 2001.
- [52] S. Bellia, F. Italiano, and P. M. Nuccio, *Le strutture sommerse ad Est di Panarea (Isole Eolie): definizione di una loro natura antropica sulla base di studi mineralogici, petrografici e geochimici*, no. 3, 1987Rapp. int. IGF- CNR, 1987.
- [53] M. Anzidei, A. Esposito, and A. Benini, "Using Roman age submerged structures as levelling benchmarks: Interactions between recent sea level variations and crustal deformations," in *Paper presented at EGS Meeting*, European Geophysical Society, 2002.
- [54] M. Anzidei, A. Esposito, and A. Benini, "Evidence of active subsidence at Basiluzzo island (Aeolian islands, southern Italy) inferred from a Roman age wharf," *Quaternary International*, vol. 332, pp. 143–150, 2014.
- [55] A. Tallarico, M. Dragoni, M. Anzidei, and A. Esposito, "Modeling long-term ground deformation due to the cooling of a magma chamber: Case of Basiluzzo island, Aeolian Islands, Italy," *Journal of Geophysical Research*, vol. 108, no. B12, article 2568, 2003.
- [56] F. Lucchi, C. A. Tranne, N. Calanchi, and P. L. Rossi, "Late Quaternary deformation history of the volcanic edifice of Panarea, Aeolian Arc, Italy," *Bulletin of Volcanology*, vol. 69, no. 3, pp. 239–257, 2007.
- [57] S. A. Rice, "Health effects of acute and prolonged CO₂ exposure in normal and sensitive populations," in *Proceedings Second Annual Conference on Carbon Sequestration*, Alexandria, VA, USA, 2003.
- [58] S. A. Rice, "Human health risk assessment of CO₂: survivors of acute high-level exposure and populations sensitive to prolonged low level exposure," in *Paper presented at 3rd Annual conference on carbon sequestration*, Alexandria, VA, USA, 2004.
- [59] M. Durand and J. G. Wilson, "Spatial analysis of respiratory disease on an urbanized geothermal field," *Environmental Research*, vol. 101, no. 2, pp. 238–245, 2006.
- [60] K. Lambeck, F. Antonioli, M. Anzidei et al., "Sea level change along the Italian coast during the Holocene and projections for the future," *Quaternary International*, vol. 232, no. 1–2, pp. 250–257, 2011.
- [61] P. Nomikou, S. Carey, D. Papanikolaou et al., "Submarine volcanoes of the Kolumbo volcanic zone NE of Santorini Caldera, Greece," *Global and Planetary Change*, vol. 90–91, pp. 135–151, 2012.
- [62] P. Nomikou, S. Carey, K. L. C. Bell et al., "Tsunami hazard risk of a future volcanic eruption of Kolumbo submarine volcano, NE of Santorini caldera, Greece," *Natural Hazards*, vol. 72, no. 3, pp. 1375–1390, 2014.
- [63] N. Calanchi, A. Peccerillo, C. A. Tranne et al., "Petrology and geochemistry of volcanic rocks from the island of Panarea: implications for mantle evolution beneath the Aeolian island arc (southern Tyrrhenian sea)," *Journal of Volcanology and Geothermal Research*, vol. 115, no. 3–4, pp. 367–395, 2002.
- [64] R. Cioni, A. Longo, G. Macedonio et al., "Assessing pyroclastic fall hazard through field data and numerical simulations: example from Vesuvius," *Journal of Geophysical Research*, vol. 108, no. B2, article 2063, 2003.
- [65] R. Cioni, A. Bertagnini, R. Santacroce, and D. Andronico, "Explosive activity and eruption scenarios at Somma-Vesuvius (Italy): towards a new classification scheme," *Journal of Volcanology and Geothermal Research*, vol. 178, no. 3, pp. 331–346, 2008.
- [66] G. Macedonio, A. Costa, and A. Folch, "Ash fallout scenarios at Vesuvius: numerical simulations and implications for hazard assessment," *Journal of Volcanology and Geothermal Research*, vol. 178, no. 3, pp. 366–377, 2008.

- [67] A. Costa, F. Dell'Erba, M. A. di Vito et al., "Tephra fallout hazard assessment at the Campi Flegrei caldera (Italy)," *Bulletin of Volcanology*, vol. 71, no. 3, pp. 259–273, 2009.
- [68] J. Selva, A. Costa, W. Marzocchi, and L. Sandri, "BET_VH: exploring the influence of natural uncertainties on long-term hazard from tephra fallout at Campi Flegrei (Italy)," *Bulletin of Volcanology*, vol. 72, no. 6, pp. 717–733, 2010.
- [69] L. Sandri, A. Costa, J. Selva et al., "Beyond eruptive scenarios: assessing tephra fallout hazard from Neapolitan volcanoes," *Scientific reports*, vol. 6, no. 1, article 24271, 2016.
- [70] G. S. Gorshkov, "Gigantic eruption of the volcano Bezymianny," *Bulletin Volcanologique*, vol. 20, no. 1, pp. 77–109, 1959.
- [71] K. Nakamura, "Energy dissipated with volcanic activities. Classification and evolution," *Bulletin of the Volcanological Society of Japan*, vol. 10, pp. 81–90, 1965.
- [72] F. Italiano, C. Caruso, A. Corbo, G. Lazzaro, and P. Favali, "Hydrothermal fluids vented at shallow depths at the Aeolian Islands (Italy): geochemical features and automatic monitoring systems," in *Abstracts of 13th International Conference on Gas Geochemistry*, Chinese Academy of Sciences, Guangzhou Institute of Geochemistry, Chengdu, China, 2015.
- [73] C. Caruso, G. Lazzaro, M. Longo, D. Romano, S. Scirè Scappuzzo, and F. Italiano, "New insights into submarine hydrothermal system phenomena revealed by acoustic monitoring technologies," in *Abstract of 3rd Italian marine geologist Conference, The marine geology in Italy*, Società Geologica Italiana, Rome, Italy, 2019.
- [74] G. Chiodini, S. Caliro, G. Caramanna et al., "Geochemistry of the submarine gaseous emissions of Panarea (Aeolian Islands, Southern Italy): magmatic vs. hydrothermal origin and implications for volcanic surveillance," *Pure and Applied Geophysics*, vol. 163, no. 4, pp. 759–780, 2006.
- [75] F. Tassi, B. Capaccioni, G. Caramanna et al., "Low-pH waters discharging from submarine vents at Panarea Island (Aeolian Islands, southern Italy) after the 2002 gas blast: origin of hydrothermal fluids and implications for volcanic surveillance," *Applied Geochemistry*, vol. 24, no. 2, pp. 246–254, 2009.
- [76] A. Billi, G. Barberi, C. Faccenna, G. Neri, F. Pepe, and A. Sulli, "Tectonics and seismicity of the Tindari Fault System, southern Italy: crustal deformations at the transition between ongoing contractional and extensional domains located above the edge of a subducting slab," *Tectonics*, vol. 25, no. 2, article 2006, 2006.
- [77] C. Monaco and L. Tortorici, "Active faulting in the Calabrian arc and eastern Sicily," *Journal of Geodynamics*, vol. 29, no. 3-5, pp. 407–424, 2000.
- [78] H. P. Eugster and D. R. Wones, "Stability relations of the ferruginous biotite, annite," *Journal of Petrology*, vol. 3, no. 1, pp. 82–125, 1962.